POLITECNICO
MILANO 1863

DIPARTIMENTO DI MECCANICA

mecc

Constitutive description of work hardening and dynamic softening behavior under variable deformation states

Caiyi Liu, Shuo Guo, Shicheng Liang, Ruowei Li, Silvia Barella, Yan Peng, Xiaoming Qian,Andrea Gruttadauria, Marco Belfi, Jianliang Sun, Carlo Mapelli

This is a post-peer-review, pre-copyedit version of an article published in Journal of Materials Processing Technology. The final authenticated version is available online at: http://dx.doi.orgj.jmatprotec.2023.118188

This content is provided under CC BY-NC-ND 4.0 license

Constitutive description of work hardening and dynamic softening behavior under variable deformation states

Caiyi Liu[a,*], Shuo Guo[a], Shicheng Liang[a], Ruowei Li[a], Silvia Barella[b], Yan Peng[a,*], Xiaoming Qian[a], Andrea Gruttadauria[b], Marco Belfi[b], Jianliang Sun[a], Carlo Mapelli[b]

[a] National Engineering Research Center for Equipment and Technology of Cold Strip Rolling, Yanshan University, Qinhuangdao 066004, China

[b] Department of Mechanical Engineering, Politecnico di Milano, Milan, 20156, Italy

[*] Correspondence: pengyan@ysu.edu.cn +86 0335-8387651

Abstract: By carrying out hot compression experiments for 316L austenitic stainless steel under dynamic changes in deformation conditions, the work hardening and softening behaviors are systematically analyzed during the temperature and strain rate changing process. The response pattern of stresses to changes in temperature and strain rate during deformation is related to material properties and deformation conditions. Zener Hollomon parameters can unify the influence. The stress response pattern changes as the value of Z increases or decreases. Further a computational procedure of materials constitutive relationship suitable for the deformation process under dynamic changes in deformation conditions is proposed. The calculation procedure is based on the phenomenal model. Compared with physical-based model, the procedure shows the same accuracy for the prediction of stress and degree of recrystallization and a simple establishment process. The calculation procedure is embedded into DEFORM software. The high-temperature deformation behavior is numerically simulated under dynamic changes in deformation conditions. The dynamic changes in deformation conditions affect the center deformation resistance during the deformation process, affecting the competitive coordination of material deformation resistance and indenter-sample interfacial friction and ultimately affecting the deformation distribution. 4) The microstructure evolution during dynamic variation states is revealed by EBSD characterization. The deformation conditions variation results in the hardening and softening mechanism changing. Especially, at 1000°C the strain rate changing from 0.01s^{-1} to 0.001 s^{-1} results in the recrystallization mechanism changing from CDRX to DDRX to CDRX.

Keywords: Dynamic recrystallization; Constitutive description; Numerical simulation; Variable deformation states.

1.Introduction

High-temperature plastic deformation plays an essential role in the processing of metallic materials. During high-temperature forming processes, materials exhibit complex microstructural evolution under the influence of deformation conditions (temperature, strain rate, deformation degree), determining deformation resistance and influencing macroscopic plastic deformation. Numerical simulations enable the analysis of the microstructure, deformation resistance, and plastic flow of materials at any time and position in a complex thermal processing history. Therefore, accurate numerical simulation is a critical way to obtain products with the desired shape and properties and to guarantee the stability of the process.

The accuracy of the thermal process simulation relies on an accurate description of the constitutive relationships (coupling relationships between flow stresses, microstructure states, and deformation conditions). An accurate constitutive model describing the hot deformation process must consider at least three mechanisms of hardening and softening brought about by work hardening (WH), dynamic recovery (DRV), and dynamic recrystallization (DRX). Depending on whether the physical mechanism is considered or not, the models can be distinguished into the phenomenological and physically based. The phenomenological constitutive model directly describes the macro and microscopic behavior with deformation conditions by fitting mathematical formulas based on the change law of stress or microstructure. Han et al. performed high-temperature compression experiments of earth magnesium alloy (WE43) to obtain the stress-strain curves (Han et al., 2023). A strain-compensated constitutive model of the Arrhenius equation

was developed based on stress-strain data. The model made an accurate prediction of the high-temperature deformation behavior. Gao et al. conducted high-temperature tensile tests on Ti-6Al-4V alloy at different temperatures (650, 700, 750°C) and strain rates ($0.1s^{-1}$, $0.01s^{-1}$, $0.001s^{-1}$) (Gao et al., 2022). Based on the stress-strain data, phenomenological constitutive models such as Johnson Cook (JC) and Henesel Spittel were developed. The accuracy of different models was compared, and the corresponding models were modified to improve the prediction accuracy. Sulzbach et al. performed high-temperature torsional tests on high Nb- and N-containing austenitic stainless-steel biomaterial alloys (De Sousa Sulzbach et al., 2022). A DRV-DRX staged constitutive model was developed to predict the stress changes at 900-1200°C and $0.01\text{-}10s^{-1}$ considering the DRV and DRX softening phenomena. Based on physical-based models, dislocation dynamics, crystal plasticity, and thermodynamics consider the material deformation mechanism to link deformation conditions and macro and micro behaviors with material states at different scales. Lin et al. consider the dislocation proliferation and recombination under WH and DRV. The hardening coefficient and dislocation density were introduced, and a physical-based constitutive model was constructed to predict Al-Zn-Mg-Cu alloy's flow stress and dislocation density (Lin et al., 2018). Su et al. constructed a viscoelastic-plastic model based on the flow stress, grain size, and recrystallization degree of AZ80 magnesium alloy under different deformation conditions (Su et al., 2022). Considering DRV and discontinuous dynamic recrystallization (DDRX) softening mechanisms, a comprehensive prediction of the flow stress, DRX degree, and grain size of AZ80 magnesium alloy was made. In summary, the phenomenal constitutive model is simple, intuitive, easy to construct, and integrated with numerical simulation methods. The physical-based constitutive model can record the changes in material states at different scales in a more detailed and accurate way. However, it requires a large amount of data, and the establishment process is complicated. Embedding in the finite element software for wide application in industrial production is challenging.

Although, after much research, modification, and extension, both phenomenal and physical-based constitutive models can accurately predict the thermal deformation processes of metallic materials under a wide range of deformation conditions. However, the phenomenal constitutive model shows a weak predictive ability for some complex loading histories. The deformation temperature and strain rate are not constant or nearly constant during the deformation process. The predictions of the phenomenal constitutive model show large deviations during deformation conditions variation. With the research and development of forming technology, the not close to a steady state of deformation conditions is gradually recognized. During the hot rolling process, the strip experiences a bite-in and exit process. The strain rate first dramatically increases and then dramatically decreases. Moreover, due to the heat exchange with the rollers, the surface metal will also occur with a significant temperature decrease (Peng et al., 2022a). Alternatively, with dynamic processing techniques such as flexible rolling (Liu et al., n.d.) and variable rate pressure forming (Wang et al., 2022), multi-strand rollers' synergistic input and exit and the variation of die depression rates make temperature and strain rate changes more significantly. Moreover, varying the deformation conditions during the deformation process allows for more flexible regulation of the forming process. Chen et al. performed hot compression and characterization experiments on Ni-30% Fe austenitic steels with strain rate transient increase (Chen et al., 2019). The strain rate transient increase resulted in a shift from a DDRX to a continuous dynamic recrystallization (CDRX) mechanism for dynamic recrystallization. On the one hand, dislocations formed at grain boundaries after a transient strain rate increase inhibit strain-induced grain boundary migration (DDRX process). On the other hand, substructures formed during the low-strain rate deformation stage absorb dislocations formed during the high-strain rate deformation stage, promoting substructure rotation to form high-angle grain boundaries (CDRX process). The synergistic interaction between different dynamic recrystallization mechanisms influences the hardening and softening behavior, controlling the variation of flow stresses. Liu et al. systematically characterized the microstructural evolution of 316L austenitic stainless steel under a dynamic variation state (Liu et al., 2023, 2022). Dynamic variation in deformation conditions altered the internal storage energy, dislocation density, grain boundary distribution, and crystal orientation. The different grain characteristics can be obtained by flexibly changing the deformation conditions. Wang et al. investigated nickel-based alloys' crystal orientation and texture evolution under strain rates transient changing state

(Wang et al., 2020). The corresponding texture required for nickel-based alloys could be obtained by varying the strain rate flexibly. Wang et al. performed high-temperature tensile experiments on Ti2AlNb-alloy in the strain-rate varying state (Wang et al., 2022). A reasonable varying strain rate is beneficial to reduce the damage during the tension of titanium alloys. Therefore, to meet the needs of accurate prediction, planning, and regulation of flexible forming processes, a robust constitutive model needs to adapt to a wide range of deformation conditions, covering different physical mechanisms and the dynamic variations of deformation conditions. All the constitutive models applicable to the dynamic variation of deformation conditions are the physical-based model. He et al. constructed a physical-based constitutive model of Ni-Mo-Cr base alloy by considering the dislocation proliferation under work hardening, dislocation reorganization under DRV, and dislocation absorption under DDRX grain nucleation and growth (He et al., 2022). It accurately predicted the flow stress evolution under abrupt strain rate variation. Wang et al. constructed a physical-based constitutive model for the hot tension process of TA15 titanium alloy considering the α-phase spherization, DRX, and damage (Wang et al., 2022). It accurately predicted the flow stress, recrystallization volume fraction, and damage degree under the transient strain rate change. It significantly improves the prediction accuracy compared with the phenomenal constitutive model. Wang et al. conducted high-temperature compression tests on Inconel 740 superalloy (Wang, 2020). They constructed a viscoelastic-plastic constitutive model considering the DRV and DRX effects to accurately predict the flow stresses and recrystallization fraction under transient changes in strain rate. This is attributed to the ability to record continuous evolutions in the material state at different scales during the deformation process. However, as mentioned earlier, the physical-based constitutive model requires many different data scales for correction and exhibits a complex form and establishing process. As a result, its usefulness in finite element simulation and industrial production is constrained.

Compared with the physical-based constitutive model, the phenomenon constitutive model is less investigated for the prediction of flow stresses under dynamically changing deformation conditions. Puchi-Cabrera et al. attributed the lack of predictive ability of the phenomenal constitutive model under changing deformation conditions to the fact that the model uses strain as a variable for calculation (Puchi-Cabrera et al., 2018, 2014). They extended the Sellars-Tegart-Garofalo (STG) phenomenal and DRV-DRX two-stage models in differential form. Different C-Mn steels' stress and recrystallization fraction was predicted for successive changes in strain rate and temperature. However, the accuracy of the prediction results was not fully validated by experiments. Zeng et al. constructed a phenomenal constitutive model in differential form for 300M high-strength steel to predict the change in stress and degree of recrystallization at constant strain rate and temperature (Zeng et al., 2019). However, the applicability of the dynamic variation deformation conditions state has not been verified.

Therefore, this paper aims to develop a computational procedure based on the conventional phenomenal constitutive model for prediction under dynamically changing deformation conditions. First, the stress-strain relationship is obtained by conducting high-temperature deformation experiments with deformation conditions' dynamic variation. The experimental procedures and conditions are described in detail in Section 2.1. Section 2.2 presents the conventional and extended differential form of a typical phenomenal constitutive model (DRV-DRX staged model) and a typical physical-based constitutive model (viscoelastic-plastic model). The models are constructed based on the flow stresses under steady-state deformation conditions. The hardening and softening behavior under different dynamic variation deformation conditions states are analyzed in Section 3.1. The Zener-Hollomon (Z) parameters are used to consider the effects of deformation conditions and material properties on stress changes and to reveal the stress evolution rules under a dynamic variation state. The accuracy of the three forms of models described in Section 2.2 is compared. The characteristics and reasons of suitable models for dynamic variation state are analyzed by combining the stress and microstructure evolution behavior in Section 3.2. Further, a computational procedure for flow stress prediction under dynamically changing deformation conditions is proposed based on the phenomenal constitutive model. The accuracy of the computational procedure is verified. Finally, Section 3.3 embeds the suitable constitutive model in the finite element software. The characteristics of metal plastic flow under a dynamic variation

state are investigated by numerical simulation. The coupling relationship between microstructure evolution, deformation resistance, and metal plastic flow is revealed.

2.Experiment and Materials

2.1 Experiment procedure and conditions

Gleeble 3800-GTC thermo–mechanical simulator is used to study the stress-strain relationship under the dynamic variation state. 316L stainless steel is investigated, and the chemical composition and manufacturing process can be found in the literature (Liu, 2023). Cylindrical specimens($\varphi 8 \times 12mm$) are wire cut on hot rolled steel plates. The cylindrical height direction is parallel to the normal direction of the plate. The specimens experience high-temperature uniaxial compression in argon. The specimen is polished and fastened, with a thermocouple at the center of the side surface, as shown in Fig. 1. (a) . The temperature, during the experiment, is maintained constant through and automatic control. Molybdenum disulfide lubricant is uniformly applied to cylindrical specimens' upper and lower surfaces, reducing friction, avoiding adhesion, and improving deformation stability and uniformity. Tantalum foil, 0.1 mm in thickness, and round graphite sheet, 12mm in diameter, is placed between the specimen and the indenter to prevent diffusion bonding or interfacial melting. Fig. 1. (b) shows the hot compression experimental procedure. The specimen is first heated to 1150°C at 10°C/s and held for 5 min to achieve uniform austenitization. Subsequently, the specimen temperature is lowered to the deformation temperature at 5°C/s and held for the 60s. After the temperature homogenization, the specimens are first deformed to 0.4 true strain at a constant strain rate and deformation temperature. Subsequently, the strain rate or deformation temperature changes, and the specimens keep continuous deformation to 0.9 true strain. After deformation, the specimens are water-cooled.

The experimental conditions are divided into two categories. The first is a single-pass hot compression experiment with constant temperature and strain rate transient change. As shown in Fig. 1. (c), the experiments include transient increase and decrease of strain rate and are conducted at a constant temperature of 1000°C and 1100°C, respectively. The indenter controls the transient change of strain rate during the experiment.

The second condition is a single-pass hot compression experiment with constant strain rate and deformation temperature variation. As shown in Fig. 1. (d), (e), the experimental conditions include deformation temperature increase and decrease cases performed at constant strain rates of 0.01 s^{-1} and 0.001 s^{-1}, respectively. The temperature variation during the experiment is measured by the thermocouple, compared with the preset value, and automatically controlled by the equipment. The heating and cooling rate is 10°C/s. To ensure the same variation rate, the temperature variation occurs in the 0.4-0.5 strain at 0.01 s^{-1} and in the 0.4-0.41 strain at 0.001 s^{-1}.

DEFORM software is used to simulate the high-temperature deformation behavior under dynamic variations state. The Fortran language embeds the constitutive model in the software. The accuracy of the material model and the finite element model was verified comparing the simulation and experimental results under a dynamic variation state. The deformation distribution under the dynamic variation of deformation conditions is analyzed. The influence and mechanism of the dynamic variation of the deformation conditions on the macroscopic metal flow are investigated.

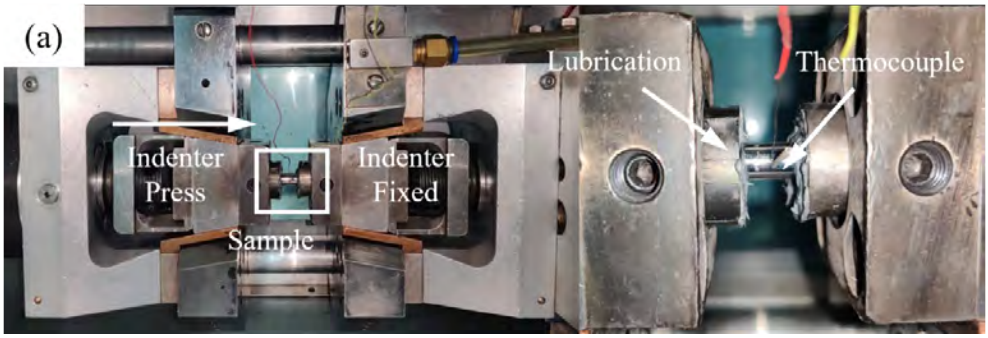

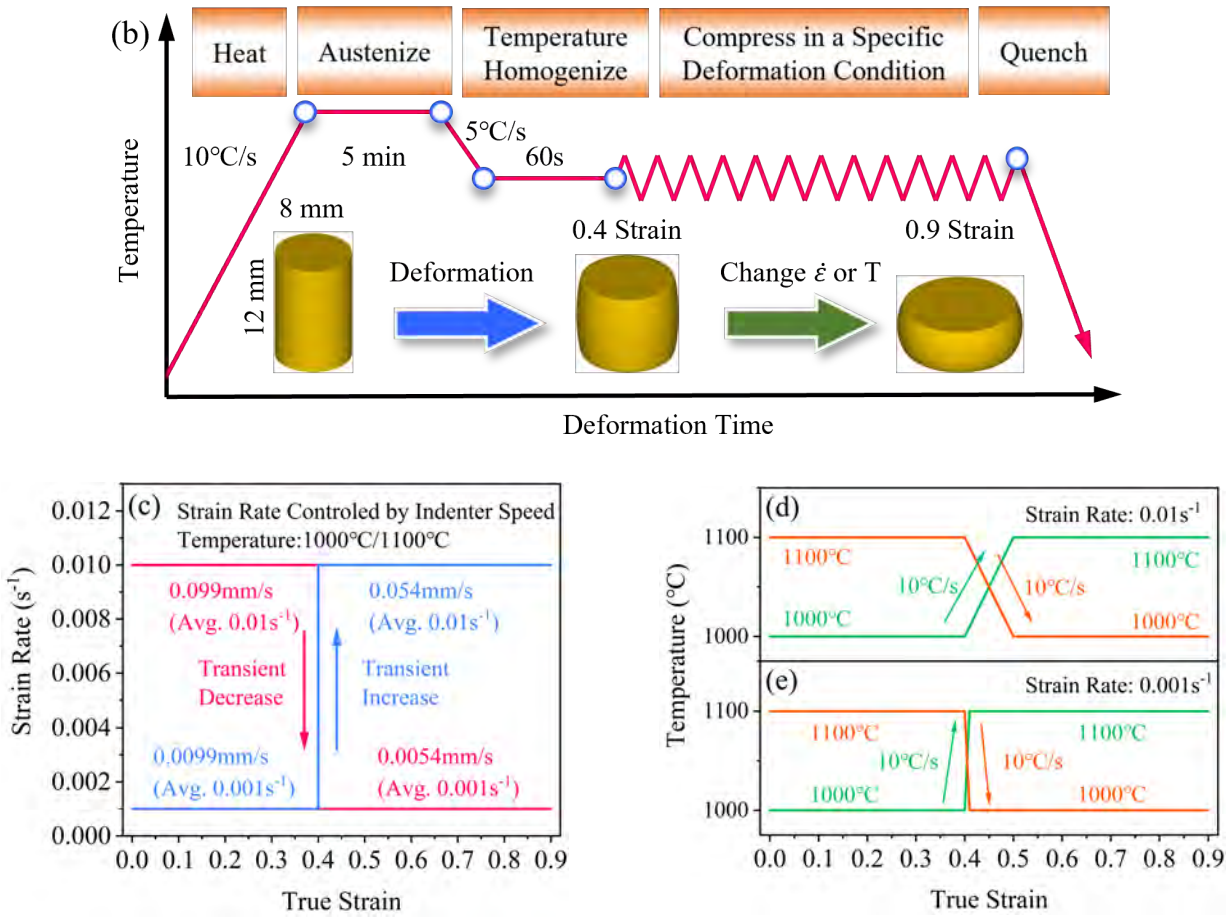

Fig. 1. Experiment procedure and conditions. (a) Experimental equipment; (b) Experimental procedure; (c) Experiment conditions for strain rate dynamic variation; (d) Experiment conditions for deformation temperature dynamic variation at 0.01 s^{-1}; (e) Experiment conditions for deformation temperature dynamic variation at 0.001 s^{-1}.

2.2 Constitutive models using in the paper

This section will construct a typical phenomenal constitutive model, including its conventional and differential form, and a physical-based model based on the steady-state deformation condition.

The phenomenal constitutive model considers that the materials' state is directly related to the deformation conditions. These models include the JC model (Gao et al., 2022), the Arrhenius model considering strain compensation (Han et al., 2023), and the model considering dynamic recovery and dynamic recrystallization (Peng et al., 2022a). Although these models have different expressions and physical meanings, their essence is considering the materials' state as a function of strain rate, deformation temperature, and deformation degree. The model, considering dynamic recovery and dynamic recrystallization, can predict microstructural evolution (recrystallization behavior) and stress-strain relationships. Therefore, this model is chosen to represent the first type of model. Eq. (1)-(3) show the conventional form of expressions:

$$\sigma = \sqrt{\sigma_{SAT}^2 + (\sigma_0^2 - \sigma_{SAT}^2)\exp(-\varepsilon r)}\left(\varepsilon_C > \varepsilon\right) \tag{1}$$

$$\sigma = \sqrt{\sigma_{SAT}^2 + (\sigma_0^2 - \sigma_{SAT}^2)\exp(-\varepsilon r)} - (\sigma_{SAT} - \sigma_{SS})X_{DRX}(\varepsilon_C \le \varepsilon) \tag{2}$$

$$X_{DRX} = 1 - \exp\left(-k\left(\frac{\varepsilon - \varepsilon_c}{\varepsilon_p}\right)^t\right)(\varepsilon_C \le \varepsilon) \tag{3}$$

Where ε is the plastic strain, r is the softening factor, σ_0 is the yield stress, σ_{SAT} is the saturation stress, ε_c

is the critical strain, ε_P is the peak strain, k and t are the DRX kinetic model coefficients, and σ_{SS} is the steady-state stress.

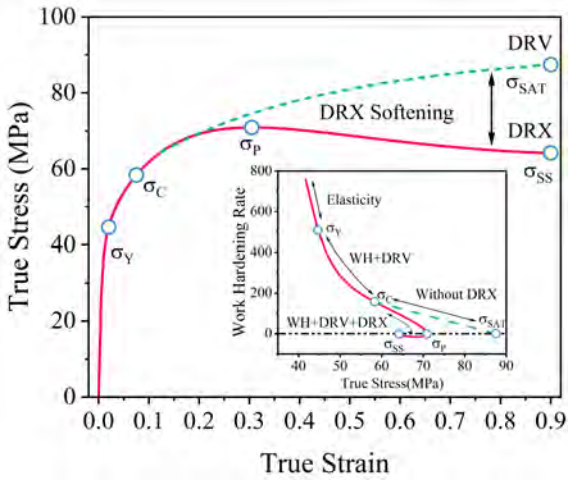

Fig. 2. Schematic diagram of stress evolution during high-temperature deformation.

As shown in Fig. 2., the model considers the hardening and softening behavior during high-temperature deformation to include the WH+DRV stage, dominated by work hardening, and the WH+DRV+DRX stage, dominated by dynamic softening. The model reflects that during the steady deformation state, the stress evolution reaches saturation under the coordination of WH+DRV. With the accumulation of internal energy, the critical condition of DRX behavior is reached and the stress decreases significantly through the rapid reduction of substructure and dislocation density by DRX grain formation. The steady-state stress, saturation stress, yield stress, critical stress, and peak stress are established by hyperbolic sine functions to the deformation conditions (Eq. (4)) (Puchi-Cabrera et al., 2018). The relationships between critical strain, peak strain, softening coefficient, and deformation conditions are established in the form of a power function through the Z-value (Eq. (5)) (Li et al., 2023):

$$p = \frac{1}{\alpha} sinh^{-1}\left[\left(\frac{\dot{\varepsilon} exp(Q/RT)}{A}\right)^{\frac{1}{n}}\right] \tag{4}$$

$$p = aZ^{b} \tag{5}$$

where p is the material characteristic parameters, and a, b, α, n, and A is the model coefficients. The relationships between critical strain, peak strain, softening coefficient, and Z value can be found in the previous literature (Liu et al., 2023, 2022). Table 1 shows the hyperbolic sine function model coefficients.

Table. 1. Model coefficients for different material characteristic parameters.

Parameter	α	$Q(KJ/mol)$	n	A
σ_{SAT}	0.00682	399233	4.82618	4.59×10^{14}
σ_Y	0.01405	572966	9.40084	4.87×10^{16}
σ_{SS}	0.00767	438742	4.56776	2×10^{16}
σ_C	0.00861	458740	4.56317	9.85×10^{16}
σ_P	0.00762	436250	4.75056	1.26×10^{16}

The differential form of the model is first proposed by Puchi-Cabrera et al (Puchi-Cabrera et al., 2018, 2014). This model assumes that the materials' state is unrelated to the strain. The essence of the model is the incremental calculation of the materials' state to eliminate the strain term from the conventional model in differential form. Eq. (6)-(10) shows the general forms:

$$dX_{DRX} = \begin{cases} 0(\sigma < \sigma_c) \\ \left(1 - X_{DRX}^i\right)\frac{kt}{\varepsilon_p}\left[-\frac{1}{k}ln\left(1 - X_{DRX}^i\right)\right]^{\frac{t-1}{t}} d\varepsilon(\sigma_c \le \sigma_i) \end{cases} \tag{6}$$

$$d\sigma_{DRV} = \frac{r}{2\sigma_{DRV}}\left({\sigma_{SAT}}^2 - \left(\sigma_{DRX} + \Delta\sigma X_{DRX}^i\right)^2\right) d\varepsilon\left(\sigma_0 \le \sigma^i < \sigma_c\right) \tag{7}$$

$$d\sigma_{DRX} = \left(\frac{r}{2\sigma_{DRV}}\left({\sigma_{SAT}}^2 - \left(\sigma_{DRX} + \Delta\sigma X_{DRX}^i\right)^2\right) - \Delta\sigma dX_{DRX}\right) d\varepsilon\left(\sigma_c \le \sigma^i\right) \tag{8}$$

$$X_{DRX}^{i+1} = X_{DRX}^i + dX_{DRX} \tag{9}$$

$$\sigma^{i+1} = \begin{cases} \sigma^i + d\sigma_{DRV}\left(\sigma_0 \le \sigma^i < \sigma_c\right) \\ \sigma^i + d\sigma_{DRX}\left(\sigma_c \le \sigma^i\right) \end{cases} \tag{10}$$

Two components bear the change in stress during plastic deformation. As deformation proceeds, the changes in dislocation density and degree of recrystallization under the combined effect of WH, DRV, and DRX affect the deformation resistance. This part of the stress composition is directly related to the state of the material. Successive changes in the state of the material during deformation lead to successive changes in the deformation resistance. However, another part of the deformation resistance represents the resistance to initial slip of dislocations and is directly related to temperature and strain rate. When the deformation conditions change, the material deformation resistance, on the one hand, is influenced by the material state (dislocation density, degree of recrystallization), showing continuous changes. This part can be captured through Eq. (7)-(10). On the other hand, the deformation resistance exhibits transient changes due to the influence of changing deformation conditions. The model cannot capture the direct effect of deformation conditions. Therefore, the following correction is made in this paper to reflect the direct effect of deformation conditions on the deformation resistance by the yield stress. When the deformation conditions change, the direct effect of the deformation conditions is reflected by directly increasing or decreasing the yield stress. Eq. (7) and Eq. (8) are modified as follows:

$$d\sigma_{DRV} = \frac{r}{2\sigma_{DRV}}\left({\sigma_{SAT}}^2 - \left(\sigma_{DRX} + \Delta\sigma X_{DRX}^i\right)^2\right) d\varepsilon + \Delta\sigma_Y\left(\sigma_0 \le \sigma^i < \sigma_c\right) \tag{11}$$

$$d\sigma_{DRX} = \left(\frac{r}{2\sigma_{DRV}}\left({\sigma_{SAT}}^2 - \left(\sigma_{DRX} + \Delta\sigma X_{DRX}^i\right)^2\right) - \Delta\sigma dX_{DRX}\right) d\varepsilon + \Delta\sigma_Y\left(\sigma_c \le \sigma^i\right) \tag{12}$$

The stress values (which reflect the dislocation density) and DRX fraction are the state variables for the differential model. The differential model considers the materials' state for calculating the hardening and softening behavior. The differential model differs from the conventional ones in predicting the transient change with deformation variation. Based on the current stress value and DRX volume fraction, the model calculates the stress and DRX fraction increment with deformation conditions variation and updates the stress value and DRX volume fraction.

The physical-based model uses microstructure features, such as dislocation density, directly as a state variable to calculate the constitutive relationships. Different materials, with different elemental compositions, exhibit different forms of microstructural evolution, leading to different expression forms. The classical visco-elastic-plastic constitutive model applicable to 316L austenitic stainless steel is chosen (Su et al., 2022). Eq. (11)-(17) shows the general forms:

$$\sigma_E = E\varepsilon_E \tag{12}$$

$$\sigma = \sigma_a + \sigma_{th} \tag{13}$$

$$\sigma_{th} = \frac{1}{A_2} arcsinh\left(\frac{\dot{\varepsilon}}{A_1}\right) + \sigma_0 \tag{14}$$

$$\dot{\sigma_a} = 0.5B\bar{\rho}^{-0.5}\dot{\bar{\rho}} \tag{15}$$

$$\dot{\bar{\rho}} = A_3(1 - \bar{\rho})\dot{\varepsilon}^{\delta_1} - C\bar{\rho}^{\delta_2} - \frac{A_4\bar{\rho}}{(1 - S)^{\delta_3}}\dot{S}\dot{\varepsilon}^{b_1} \tag{16}$$

$$\dot{S} = \bar{\rho}[\chi\varepsilon - \varepsilon_c(1-S)](1-S)^{\lambda}N \quad (17)$$

$$\dot{\chi} = A_5(1-\chi)\bar{\rho} \quad (18)$$

where σ_E is the stress in the elastic stage, and E is the elastic modulus. Assuming that the material is in the elastic stage before the 0.02 strain, the stress is equal to the product of the elastic modulus and the elastic strain. The stress at the 0.02 strain is taken as the yield stress. Considering that elastic stress has a linear relationship with the strain, the elasticity modulus equals the yield stress divided by 0.02 strain. After the material enters the plastic stage, the stress contains two parts: thermally activated stress σ_{th} and athermal stress σ_a. The thermally activated stress is the initial slip resistance, which is related to the temperature, strain rate, and alloying elements. It denotes the effect of short-range obstacles on dislocation motion. The athermal stress σ_a characterizes the effect of the long-range obstacles on dislocation motion, which is related to the normalized dislocation density $\bar{\rho}$. $\dot{\bar{\rho}}$ is the normalized dislocation density change rate, where the dislocation density change considers the effects of work hardening ($A_3(1-\bar{\rho})\dot{\varepsilon}^{\delta_1}$), dynamic recovery ($-C\bar{\rho}^{\delta_2}$), and dynamic recrystallization ($-\frac{A_4\bar{\rho}}{(1-S)^{\delta_3}}\dot{S}\dot{\varepsilon}^{b}$). $\dot{S}$ is the dynamic recrystallization rate, which considers the nucleation and growth process of dynamic recrystallization. χ is the dynamic recrystallization incubation fraction, which indicates the incubation period required for dynamic recrystallization behavior, in a process influenced by the dislocation density. A_3, C, and A_5 values are temperature dependent, as shown in Eq. (18). They consider the temperature effects on work hardening, dynamic recovery, and dynamic recrystallization (Xiao et al., 2020).

$$\begin{cases} A_3 = A_{30}exp\left(\dfrac{Q_{A_3}}{RT}\right) \\ C = C_0exp\left(-\dfrac{Q_C}{RT}\right) \\ A_5 = A_{50}exp\left(-\dfrac{Q_{A_5}}{RT}\right) \end{cases} \quad (19)$$

N represents the dynamic recrystallization nucleation rate (Buzolin et al., 2021). It is influenced by temperature and strain rate:

$$N = N_0\dot{\varepsilon}^{b_2}exp\left(-\frac{Q_N}{RT}\right) \quad (20)$$

The other coefficients in the model represent the material constants, fixed values not dependent on the change in deformation conditions.

The genetic optimization algorithm in MATLAB software solved the model coefficients. The minimal residuals between the calculated and experimental data are the objective function (Xu et al., 2020). The details of the solution process can be found in other literature. Table 2 shows the model coefficients.

Table. 2. Coefficients of model 3.

Coefficient	Value	Coefficient	Value
$\boldsymbol{A_1}$	3.447	A_4	1.199
$\boldsymbol{A_2}$	0.266	δ_3	0.943
$\boldsymbol{B}$	86.554	b_1	0.0012
$\boldsymbol{A_{30}}$	-9.704	λ	1.078
$\boldsymbol{Q_{A_3}}$**(KJ/Mol)**	15414.312	N_0	30.271
$\boldsymbol{\delta_1}$	1.477	b_2	0.0015
$\boldsymbol{C_0}$	46.234	Q_N(KJ/Mol)	39518.796
$\boldsymbol{Q_C}$**(KJ/Mol)**	53231.816	A_{50}	35.8998
$\boldsymbol{\delta_2}$	17.663	Q_{A_5}(KJ/Mol)	39468.251

3.Result and Discussion

3.1 Analysis of stress-strain relationships under dynamic variation states

This section will summarize the relationship between material properties, deformation conditions, and the constitutive relationships under a dynamic variation state by studying the stress-strain relationship and analyzing the hardening and softening behavior.

Fig. 3. (a) and (c) show the stress-strain relationship and the strain rate variation under the strain rate transient increase state. The deformation temperatures are 1000°C and 1100°C, respectively, and the strain rate transient increases from 0.001 s^{-1} to 0.01 s^{-1} at strain 0.4. The solid red and dashed black lines are the stress-strain curves under dynamic variation and stable states, respectively. The solid orange line and the green dots are the experimentally set and equipment-recorded strain rate variations, respectively. Although there are small fluctuations in the strain rate, the recorded values generally agree with the preset values. Experiments can be used to study the flow behavior under strain rate transient variations. The stress-strain relationship is almost the same as at a steady state before the transient variation in strain rate. If the deformation conditions remain steady, the stress will gradually reach the steady state stress condition. However, the strain rate increases transiently from 0.001 s^{-1} to 0.01 s^{-1} at strain 0.4 (point A). The stress increases dramatically to point B, where the stress value is less than that under a steady state in the same deformation condition. As deformation continues, the stress increases to point C and gradually becomes steady. Notably, when the deformation temperature is 1100°C, during the change process from point B to C, the stress shows a trend of reaching the peak, decreasing again, and finally entering the steady state. As the deformation temperature increases, the softening effect after the strain rate transient increase becomes more significant.

Fig. 3. (b) and (d) show the stress-strain relationship and the strain rate variation under the strain rate transient decrease state. The deformation temperatures are 1000°C and 1100°C, respectively, and the strain rate transient decreases from 0.01 s^{-1} to 0.001 s^{-1} at strain 0.4. The experiment starts with steady deformation conditions. In contrast to the strain rate transient increase state, the strain rate transient decrease (which occurs at 0.4 strain) leads to a rapid stress decrease from point A to point B. The stress nearly drops to the steady-state stress after the deformation conditions variation. As deformation continues, the deformation enters the steady state, and the stress fluctuates around the steady-state stress. Notably, as in the case of a transient increase in strain rate, different deformation temperatures lead to different trends in stress variation. When the deformation temperature is 1100°C, the strain rate transient decrease leads to a rapid decrease in stress to below the steady-state stress. As deformation continues, the stress slowly increases and eventually becomes steady.

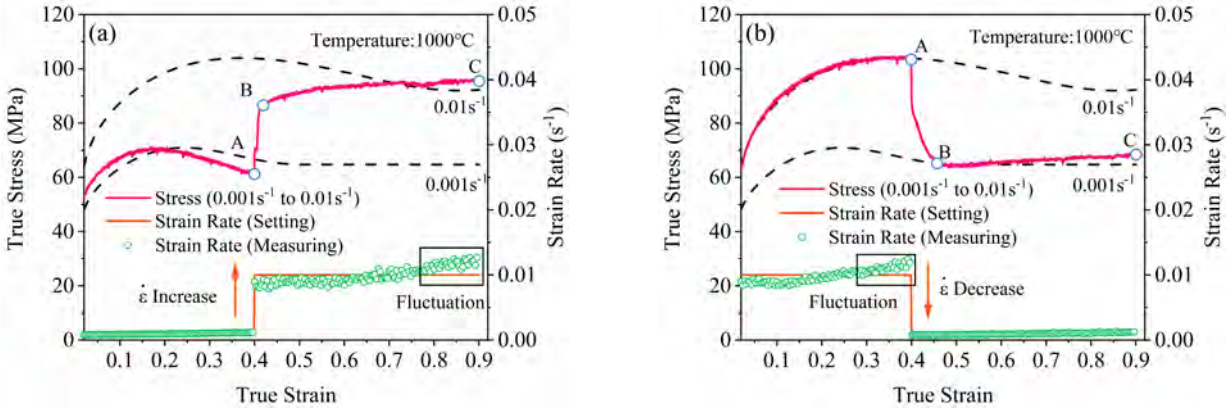

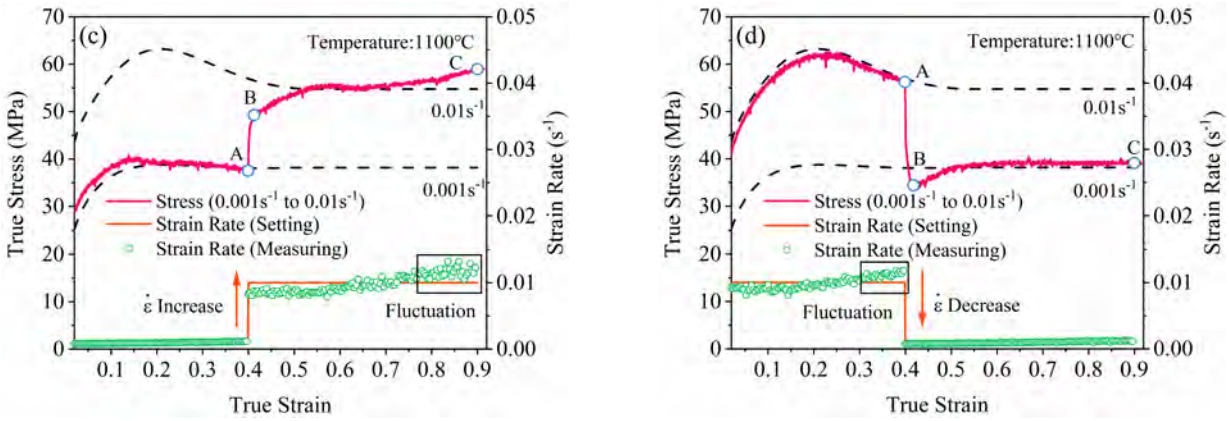

Fig. 3. Stress-strain curves under strain rate transient variation state. (a) 1000°C, and the strain rate transient increases from 0.001 s^{-1} to 0.01 s^{-1} at strain 0.4; (b) 1000°C, and the strain rate transient decreases from 0.01 s^{-1} to 0.001 s^{-1} at strain 0.4; (c) 1100°C, and the strain rate transient increases from 0.001 s^{-1} to 0.01 s^{-1} at strain 0.4; (d) 1100°C, and the strain rate transient decreases from 0.01 s^{-1} to 0.001 s^{-1} at strain 0.4.

Fig. 4. (a) and (c) show the stress-strain relationship and the deformation temperature variation under the deformation temperature decrease state. The constant strain rates are 0.01 s^{-1} and 0.001 s^{-1}, respectively, and the deformation temperature decreases from 1100℃ to 1000℃ at strain 0.4. To ensure the same temperature variation rate (10°C/s), the variation interval is 0.4-0.5 for 0.01 s^{-1} and 0.4-0.41 for 0.001 s^{-1}. The recorded temperature variations are in agreement with the experimental preset. Even though the specimen temperature distribution is inhomogeneous due to the temperature variation, the flow behavior under the temperature variation state can be studied approximately. When the deformation temperature starts to decrease, it is similar to the case of strain rate transient increase: the stress increases dramatically to point B (less than the stress value under a steady state in the same deformation condition). As the deformation continues, the stress slowly increases from point B to point C, reaching a steady state. At 0.001 s^{-1}, the stress slightly decreases after reaching the peak (from point B to point C) after the deformation temperature decreases. The low strain rate makes the softening phenomenon more obvious.

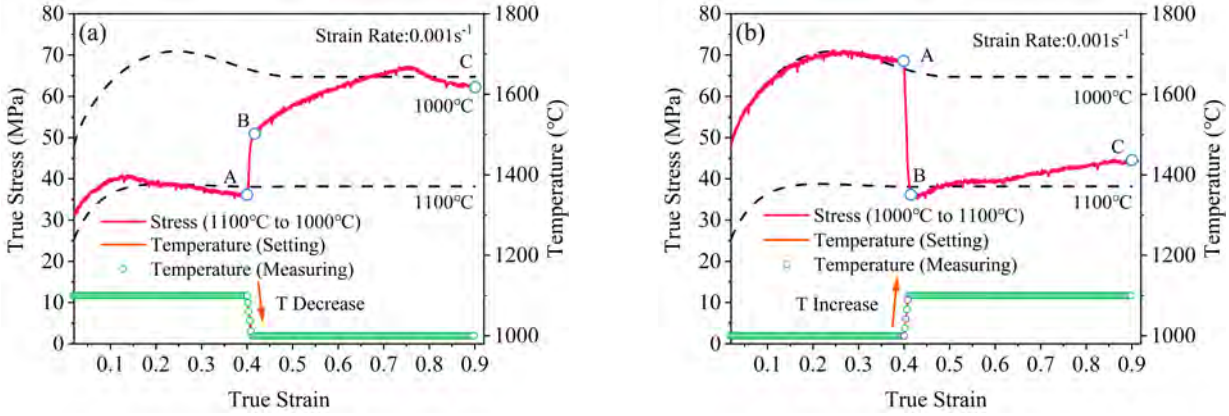

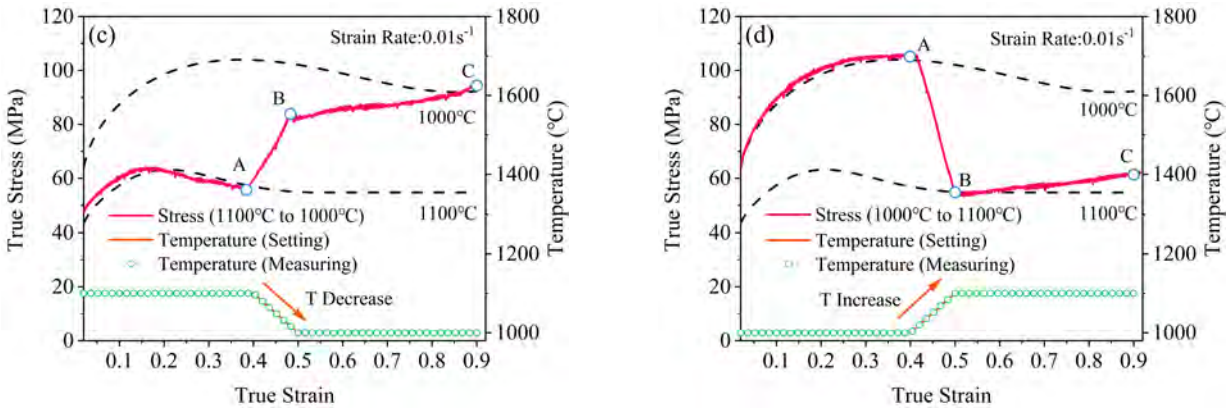

Fig. 4. Stress-strain curves under deformation temperature variation state. (a) $0.001s^{-1}$, and the deformation temperature decreases from 1100℃ to 1000℃ from strain 0.4 to 0.41; (b) $0.001s^{-1}$, and the deformation temperature increases from 1000℃ to 1100℃ from strain 0.4 to 0.41; (c) $0.01s^{-1}$, and the deformation temperature decreases from 1100℃ to 1000℃ from strain 0.4 to 0.5; (d) $0.01s^{-1}$, and the deformation temperature increases from 1000℃ to 1100℃ from strain 0.4 to 0.5.

Fig. 4. (b) and (d) show the stress-strain relationship and the deformation temperature variation under the deformation temperature increase state. The strain rates are 0.01 s^{-1} and 0.001 s^{-1}, respectively, and the deformation temperature increases from 1000℃ to 1100℃ at strain 0.4. The deformation temperature increase has the same effect as the decrease in strain rate. When the deformation temperature increases (point A), the stress rapidly decreases to point B (near the steady-state stress after the deformation conditions variation). Subsequently, the stress is nearly stable from point B to point C. Different strain rates cause different stress evolution under temperature variation states. When the strain rate is 0.01 s^{-1}, the stress decreases to near the steady-state stress after the deformation conditions variations. The stress is basically stable as the deformation proceeds (from point B to point C). When the strain rate is 0.001 s^{-1}, the stress drops below the steady-state stress after the deformation conditions variations. As deformation proceeds (from point B to point C), the stress increases and gradually becomes steady.

During high-temperature deformation, the hardening and softening behavior under the coordination of work hardening (WH), dynamic recovery (DRV), and dynamic recrystallization (DRX) directly determine the constitutive relationships (Ouyang et al., 2020). Deformation condition variations affect the WH, DRV, and DRX behavior, leading to complex stress changes. Fig. 5. and Fig. 6. show the work-hardening rate curves under the strain rate and deformation temperature variation state, respectively. In the steady-state deformation stage, the work-hardening rate shows a typical change pattern. At the beginning of deformation, the work hardening rate is at a high state and decreases rapidly. The rapid dislocation accumulation weakens the WH effect and intensifies the DRV effect. The stress increases rapidly during this stage, but the growth rate gradually decreases. When the dislocation density accumulates to a critical value, the DRX behavior activates and accelerates the decrease of the work-hardening rate.

The solid green lines in Fig. 5 (a), (c), and Fig. 6 (a), (c) show the work-hardening rate after the strain rate increase and deformation temperature decrease during the deformation process. After the deformation condition variations (point A), the work-hardening rate changes rapidly to a higher value and decreases rapidly to point B. The stress increases dramatically at this stage. The strain rate increase and deformation temperature decrease promote the dislocation proliferation and the interaction between dislocations and grain boundaries, enhancing the WH behavior (Chen et al., 2021). On the other hand, it hinders the cross-slip and climbing of the dislocation system and the grain boundary migration ability, inhibiting the softening of DRV and DRX (Yang et al., 2021). The work-hardening rate decreases, and the stress enters a slow growth stage. Moreover, after the deformation condition variations, the work hardening rate drops below zero in the high deformation temperature and low strain rate. The stress reaches a peak and decreases. The atomic thermal activation is promoted at high deformation temperatures, and the deformation time is prolonged at low strain rates. Therefore, the softening effect during deformation is more significant (Mishra et al.,

2022).

The solid green lines in Fig. 5. (b), (d) and Fig. 6. (b), (d) show the work-hardening rate during the deformation process under strain rate decrease and deformation temperature increase state. After the deformation condition variations (point A), the work-hardening rate changes to a negative value and rises rapidly to point B. The stress decreases dramatically at this stage. The lower strain rate and higher deformation temperature give sufficient time and more robust thermal activation for dislocation cross-slip, climbing, and grain boundary migration, which promotes DRV and DRX softening effect (Mishra et al., 2022). The work-hardening rate then increases, and the stress enters the steady-state stage. The stress drops below the steady state at high deformation temperatures and low strain rates and rises slowly into the steady state. The DRV and DRX behavior provides a more dramatic softening of stress reduction.

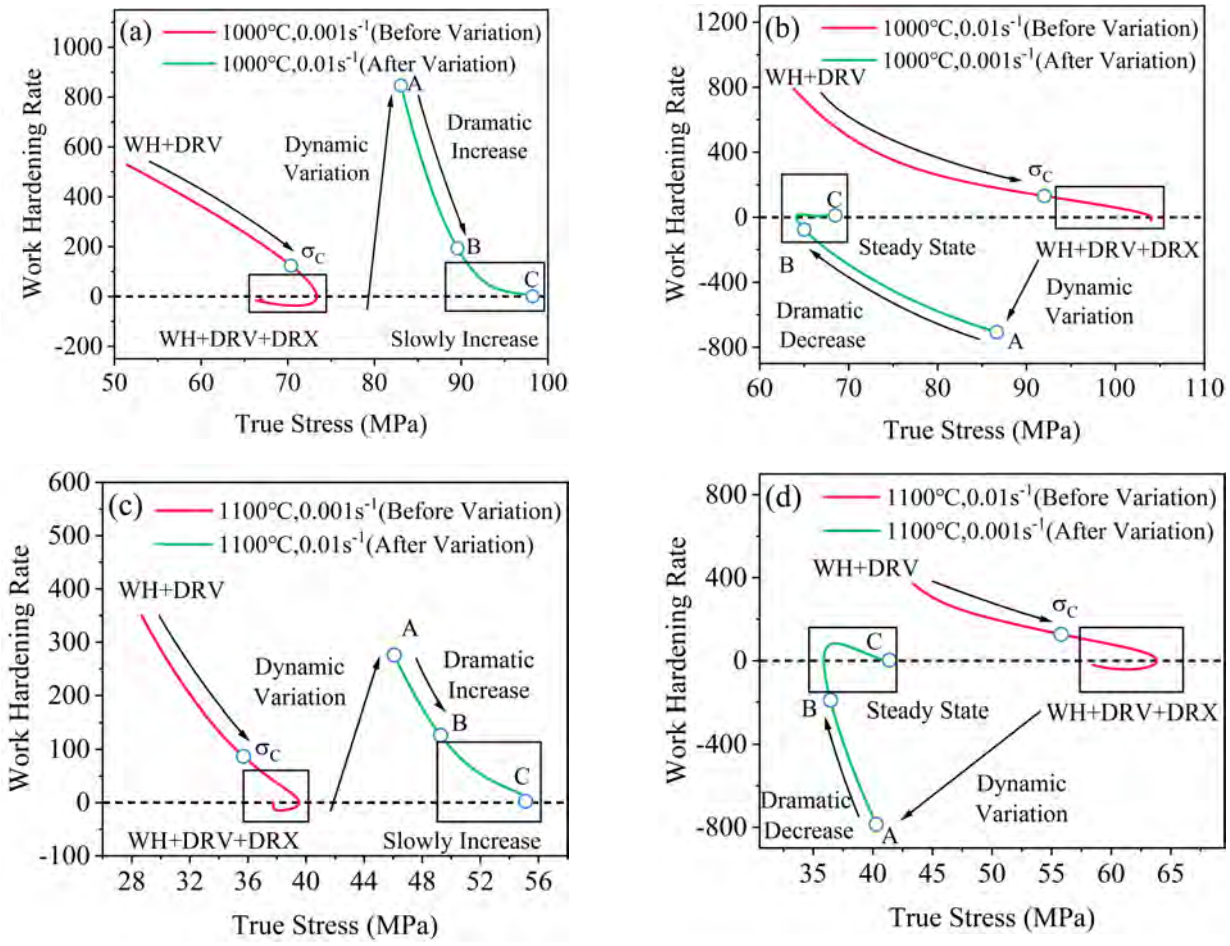

Fig. 5. Work-hardening curves under strain rate transient variation state. (a) 1000°C, and the strain rate transient increases from 0.001 s^{-1} to 0.01 s^{-1} at strain 0.4; (b) 1000°C, and the strain rate transient decreases from 0.01 s^{-1} to 0.001 s^{-1} at strain 0.4; (c) 1100°C, and the strain rate transient increases from 0.001 s^{-1} to 0.01 s^{-1} at strain 0.4; (d) 1100°C, and the strain rate transient decreases from 0.01 s^{-1} to 0.001 s^{-1} at strain 0.4.

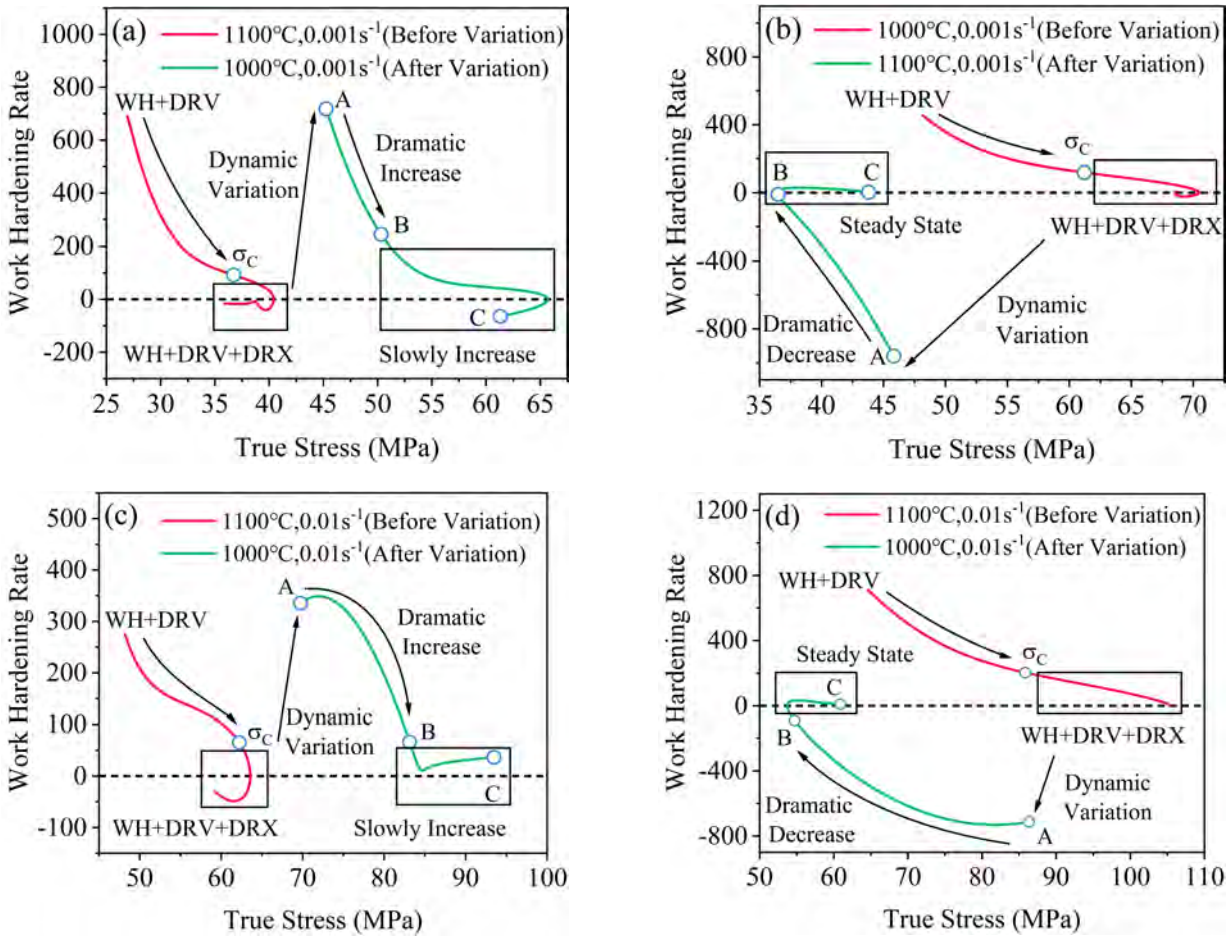

Fig. 6. Work-hardening curves under deformation temperature variation state. (a) $0.001s^{-1}$, and the deformation temperature decreases from 1100℃ to 1000℃ from strain 0.4 to 0.41; (b) $0.001s^{-1}$, and the deformation temperature increases from 1000℃ to 1100℃ from strain 0.4 to 0.41; (c) $0.01s^{-1}$, and the deformation temperature decreases from 1100℃ to 1000℃ from strain 0.4 to 0.5; (d) $0.01s^{-1}$, and the deformation temperature increases from 1000℃ to 1100℃ from strain 0.4 to 0.5.

The Zener-Hollomon parameter is often used to unify the effect of deformation conditions on the high-temperature deformation behavior (Gui et al., 2021). If the deformation conditions change after entering the steady-state stage, the stress evolution will contain two periods. The first is the severe hardening/softening stage, in which a rapid increase or decrease in stress occurs. The second is the stable variation stage, where different material compositions and deformation conditions lead to different behaviors. Fig. 7. (a) shows the stress curve for the transient increase in Z value due to deformation conditions' variations (transient increase in strain rate or rapid decrease in deformation temperature). The stress evolution shows two trends after a rapid increase. Firstly, the stress rises slowly and gradually enters a steady state (Fig. 3. (a) and Fig. 4. (c)). Secondly, the stress rises slowly, reaches the peak, and then decreases slightly, entering a steady state (Fig. 3. (c) and Fig. 4. (a)). Fig. 7. (b) shows the stress curve for the transient decrease in Z value due to deformation conditions' variations (transient decrease in strain rate or rapid increase in deformation temperature). The stress evolution also shows two trends after a rapid decrease. Firstly, the stress slowly decreases and gradually enters a steady state (Fig. 3. (b) and Fig. 4. (d)). Secondly, the stress decreases to below the steady state and increases again, entering the steady state (Fig. 3. (d) and Fig. 4. (b)).

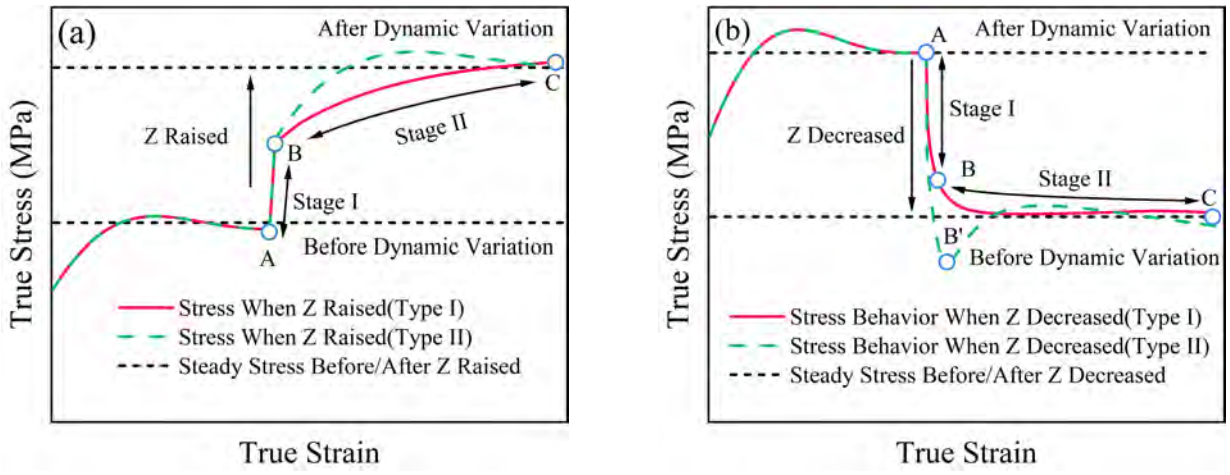

Fig. 7. The stress evolution after deformation conditions variation when entering the steady-state stage. (a) Z value transient increase; (b) Z value transient decrease.

To further illustrate the effect of material properties and deformation conditions on stress evolution after deformation conditions dynamic variation, Fig. 8 shows the variation of the Z value under different deformation conditions. The stress evolution is related to the Z-value: when the overall Z value is small, the Z value transiently increases, and the stress, after a dramatic increase, shows a trend of slowly increasing to the peak and slightly decreasing into the steady state (Fig. 3. (a) and Fig. 4. (c)). The DRX and DRV exhibited a more significant softening effect at high deformation temperatures and low strain rates. After the deformation conditions variation, the accumulated dislocations decreased rapidly under the more substantial softening effect and showed a significant softening phenomenon. When the overall Z value is considerable, the Z value transiently increases, and the stress, after a dramatic increase, shows a trend of slowly increasing to the peak and gradually reaching the steady state (Fig. 3. (c) and Fig. 4. (a)). At low deformation temperatures and high strain rates, the softening ability of DRX and DRV is insufficient. DRV and DRX at high Z are insufficient for the significant softening behavior. Table 3 shows the stress evolution type when deformation conditions variation occurs in the steady state for different materials and deformation conditions. The stress evolution type is illustrated in Fig. 7. Table 3 includes stainless steel, nickel-based alloys, high-entropy alloys, and carbon steel (Abbod et al., 2008; Chen et al., 2019; Graetz et al., 2014; He et al., 2018; Lin et al., 2018; Liu et al., 2017; Svyetlichnyy et al., 2013; Wang et al., 2020). The stress evolution type is related to material properties and deformation conditions. Fig. 9. shows the range of Z value variation for some materials in Table 3. The Z value can unify the influence of material properties and deformation conditions on the stress evolution type. The softening ability is relatively weak in the high Z value case (high thermal activation energy, high strain rate, low deformation temperature), and the stress evolution shows the type I. In the low Z value case (low thermal activation energy, low strain rate, high deformation temperature), the softening behavior is relatively sustainable, and the stress evolution exhibits the type II.

Table. 3. The stress evolution type when deformation conditions variation occurs in the steady state for different materials and deformation conditions.

Materials	Changing of The Deformation Conditions	Type
316L Stainless Steel (Abbod et al., 2008)	1025℃, $5s^{-1}$-$50\ s^{-1}$, $5s^{-1}$-$0.05s^{-1}$	Type I
Austenitic Steel 800H (Frommert and Gottstein, 2009; Graetz et al., 2014)	1100℃,$0.01s^{-1}$-$0.001s^{-1}$, $0.001s^{-1}$-$0.01s^{-1}$	Type II
Ni-based Superalloy (He et al., 2018)	980℃,$1s^{-1}$,$0.1s^{-1}$,$0.01s^{-1}$-$0.001s^{-1}$ 980℃, $0.001s^{-1}$-$1s^{-1}$,$0.1s^{-1}$,$0.01s^{-1}$	Type I
Al-Zn-Mg-Cu Alloy (Lin et al., 2018)	380℃,$0.01s^{-1}$-$0.001s^{-1}$, $0.001s^{-1}$-$0.01s^{-1}$	Type I
Ni-30%Fe austenitic alloy (Chen et al.,	900℃, $0.001s^{-1}$-$0.1s^{-1}$	Type I

2019)		
Ni-based Superalloy (Liu et al., 2017)	1100℃, $0.1s^{-1}$-$0.01s^{-1}$, $0.01s^{-1}$-$0.1s^{-1}$	Type I
45 Steel (Svyetlichnyy et al., 2013)	800℃,$1s^{-1}$-$0.1s^{-1}$,$10s^{-1}$-$1s^{-1}$,$0.1s^{-1}$-$10s^{-1}$	Type I
740 Superalloy (Wang, 2020)	1100℃, $0.1s^{-1}$-$0.01s^{-1}$, $0.01s^{-1}$-$0.1s^{-1}$	Type I

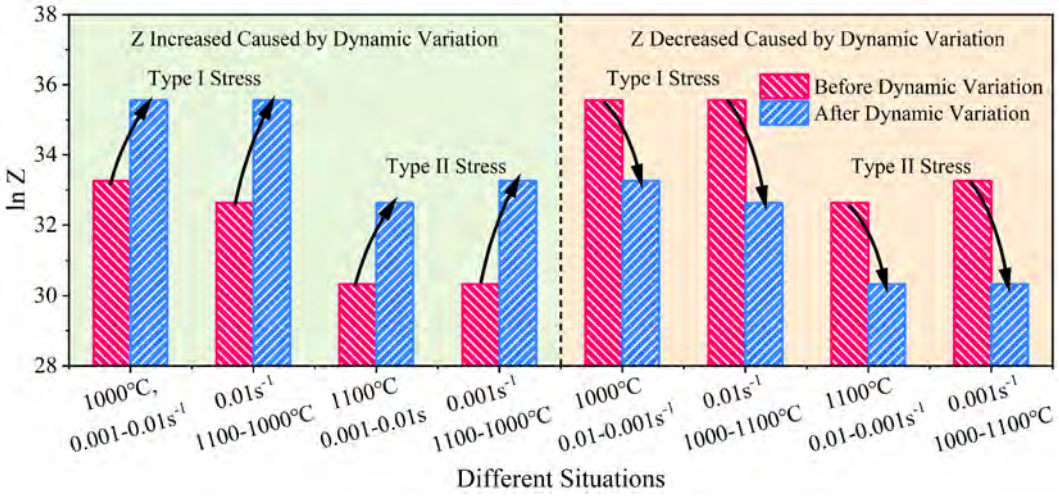

Fig. 8. The variation of the Z value under different deformation conditions in this paper.

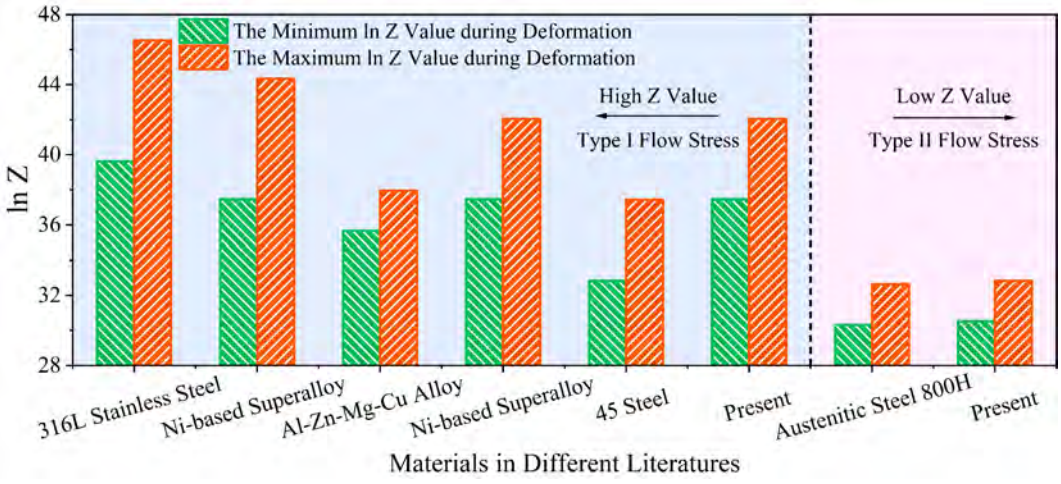

Fig. 9. The range of Z value variation for some materials in Table 3.

3.2 Analysis of the accuracy of different constitutive models under the variation of deformation conditions

This section compares the accuracy of the three forms of models described in Section 2.2. The characteristics and reasons of suitable models for dynamic variation state are analyzed by combining the stress and microstructure evolution behavior. Finally, a computational procedure for flow stress prediction under dynamically changing deformation conditions is proposed based on the phenomenal constitutive model, which achieves the same accuracy as the physical-based model.

For illustration, the conventional form of the DRV-DRX staged constitutive model is named model 1. The differential form is named model 2. The physical-based constitutive model is named model 3. Fig. 10 compares the accuracy of models 1, 2 and 3 for different deformation temperatures (1000℃,1050℃, and 1100℃) and strain rates ($0.001s^{-1}$,$0.01s^{-1}$, and $0.1s^{-1}$). The model 1 has the same prediction results as model 2 for the steady deformation state. As shown in table 4, the model 1 and 2's root mean square error (RMSE), correlation coefficient (R), and average absolute relative error (AARE) are 3.428MPa, 0.9901, and 0.03487, respectively. The model 3's root mean square error (RMSE), correlation coefficient (R), and average absolute relative error (AARE) are 2.201MP, 0.9951, and 0.02102, respectively. All models make reasonable predictions for the steady deformation state.

Table. 4. The accuracy of the three models for the steady deformation state.

	Model 1	Model 2	Model 3
RMSE (MPa)	3.428	3.428	2.201
R	0.9901	0.9901	0.9951
AARE	0.03487	0.03487	0.02102

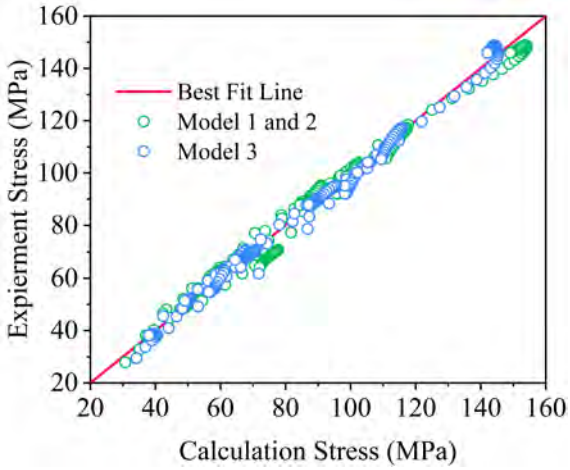

Fig. 10. The comparison between the accuracy of models 1 and 3 for steady deformation conditions.

Fig. 11. compare the prediction of the three models for the dynamic variation states. Fig. 11. (a), (c), (e), and (g) show the case of increasing Z value (increasing strain rate or decreasing deformation temperature). As shown in table 5, the model 1's RMSE, R, and AARE are 8.198MPa, 0.88919, and 0.08181, respectively. The model 2's RMSE, R, and AARE are 4.017MPa, 0.96129, and 0.03934, respectively. The model 3's RMSE, R, and AARE are 3.725MPa, 0.94864, and 0.03887, respectively. Model 2 and 3 shows high accuracy. Both models successfully reflect the trend of a transient flow stress increase and gradually increasing into a steady state. Model 1 considers that the materials' state is directly controlled by strain, strain rate, and deformation temperature, ignoring the continuous change process of the materials' state and leading to extensive prediction results. Model 2 takes the stress value and the recrystallization degree as state variables and considers the continuous evolution process of the materials' state. The direct effect of strain rate and deformation temperature on the materials' state is reflected by the yield stress. Model 3 successfully considers the transient and continuous change in the materials' state under a dynamic variation state by introducing thermally activated and athermal stress.

Table. 5. The accuracy of the three models for the dynamic variation state (the case of increasing Z value).

	Model 1	Model 2	Model 3
RMSE (MPa)	8.198	4.017	3.725
R	0.88919	0.96129	0.94864
AARE	0.08181	0.03934	0.03887

Fig. 11. (b), (d), (f), and (h) show the case of decreasing Z value (decreasing strain rate or increasing deformation temperature). As shown in table 6, the model 1's RMSE, R, and AARE are 3.743MPa, 0.96283, and 0.05723, respectively. The model 2's RMSE, R, and AARE are 6.994MPa, 0.83195, and 0.11066, respectively. The model 3's RMSE, R, and AARE are 3.676MPa, 0.94273, and 0.05709, respectively. In the Z value decreases cases, model 1 and 3 shows high accuracy. The dynamic variation of deformation conditions first causes a transient decrease of the flow stress, reflected by the thermally activated stress in model 3 and yield stress in model 2. Subsequently, under the coordination of WH+DRV+DRX, the flow stress gradually enters the equilibrium state. It is noteworthy that Model 1 exhibits better prediction accuracy for both cases of Fig. 11. (d), (h) (when the deformation temperature is 1100°C and the strain rate is changed from 0.01 to 0.001, and when the strain rate is 0.001 and the deformation temperature is changed from 1000°C to 1100°C). This is because both cases have higher temperatures and lower strain rates. The DRV and DRX exhibit a robust softening effect. Moreover, the proliferation and interaction of dislocations under the

action of WH are weaker. The material state is more likely to reach equilibrium under WH, DRV, and DRX joint action. Therefore, when the change of deformation conditions leads to a decrease in the Z value, it can be approximated that the stress quickly enters the corresponding equilibrium state after the change of deformation conditions. Therefore, both Model 1 and Model 3 show high prediction accuracy for decreasing Z-value.

Table. 6. The accuracy of the three models for the dynamic variation state (the case of decreasing Z value).

	Model 1	**Model 2**	**Model 3**
RMSE (MPa)	3.743	6.994	3.676
R	0.96283	0.83195	0.94273
AARE	0.05723	0.11066	0.05709

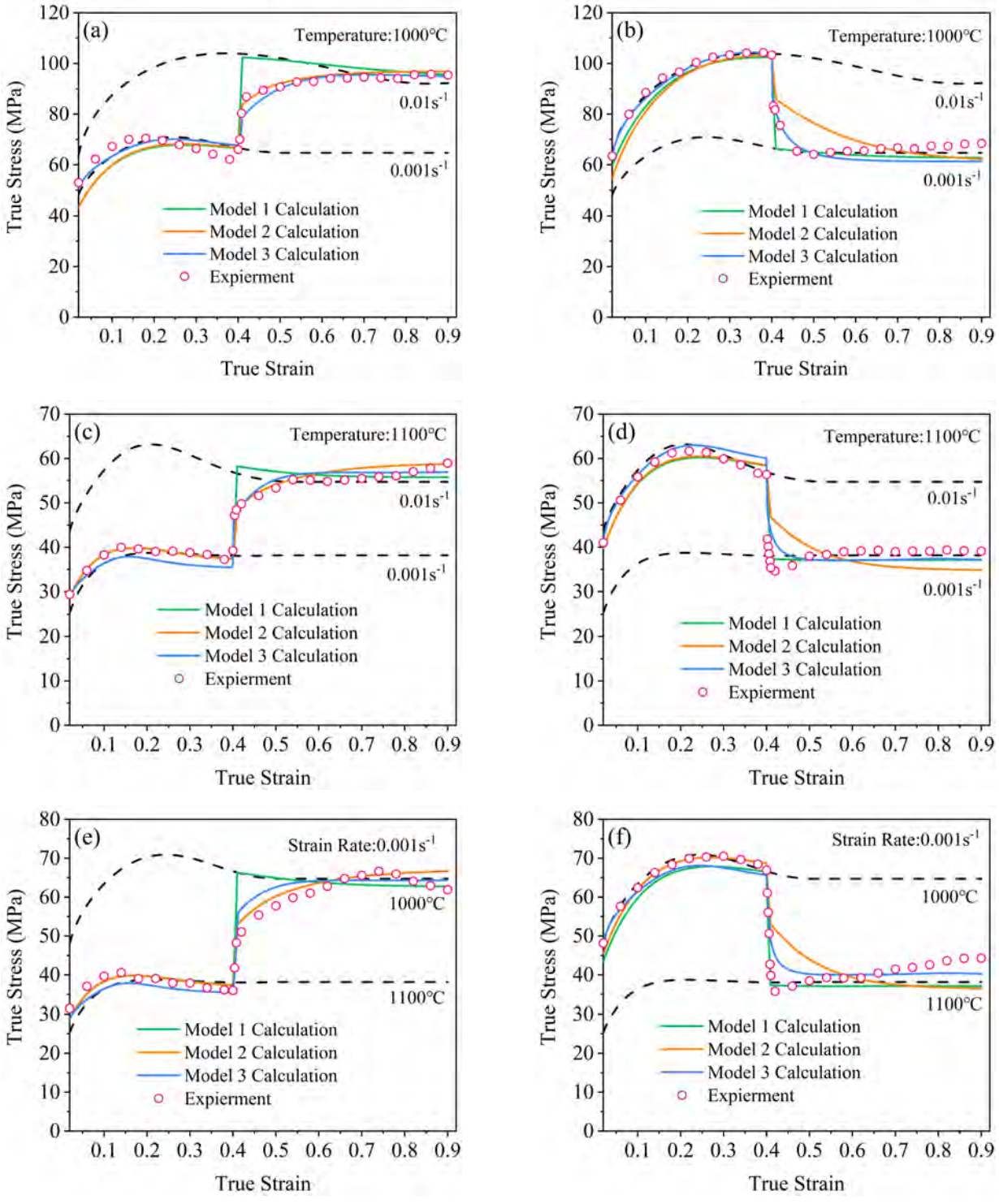

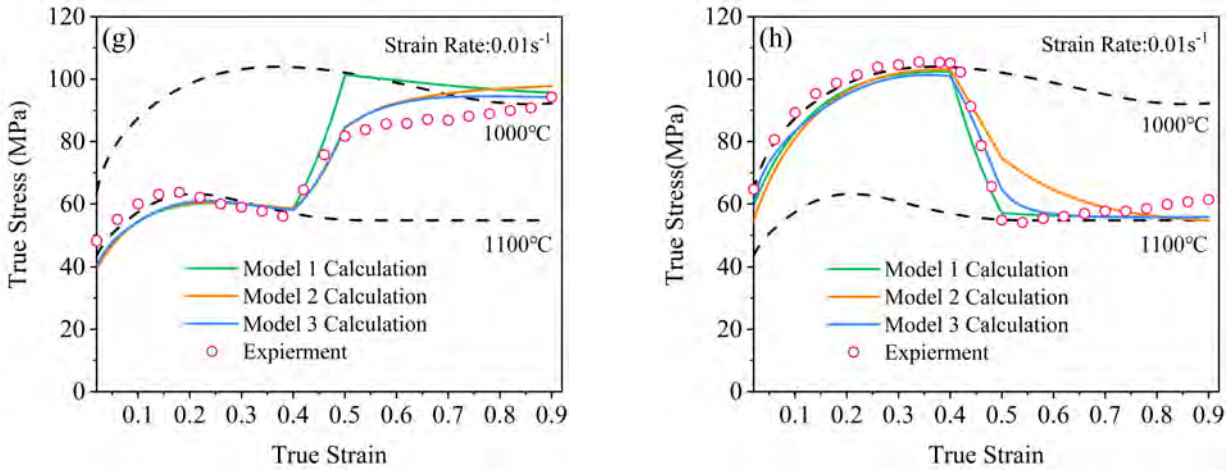

Fig. 11. The comparison between the accuracy of the three models for the dynamic variation states. (a) 1000°C, and the strain rate transient increases from 0.001 s^{-1} to 0.01 s^{-1} at strain 0.4; (b) 1000°C, and the strain rate transient decreases from 0.01 s^{-1} to 0.001 s^{-1} at strain 0.4; (c) 1100°C, and the strain rate transient increases from 0.001 s^{-1} to 0.01 s^{-1} at strain 0.4; (d) 1100°C, and the strain rate transient decreases from 0.01 s^{-1} to 0.001 s^{-1} at strain 0.4; (e) 0.001s^{-1}, and the deformation temperature decreases from 1100℃ to 1000℃ from strain 0.4 to 0.41; (f) 0.001s^{-1}, and the deformation temperature increases from 1000℃ to 1100℃ from strain 0.4 to 0.41; (g) 0.01s^{-1}, and the deformation temperature decreases from 1100℃ to 1000℃ from strain 0.4 to 0.5; (h) 0.01s^{-1}, and the deformation temperature increases from 1000℃ to 1100℃ from strain 0.4 to 0.5.

Based on the above analysis, this paper proposes a computational procedure that combines the conventional and differential forms of the DRV-DRX staged model. The procedure calculates the stress and recrystallization fraction in differential form when the deformation conditions change, causing an increase in Z-value. When the deformation conditions change, causing a decrease in Z-value, the procedure calculates the stress and recrystallization fraction changes in conventional form. Fig. 12. compares the accuracy between the proposed procedure and the physical-based model. Both have similar accuracy for predicting flow stress under dynamically changing deformation conditions.

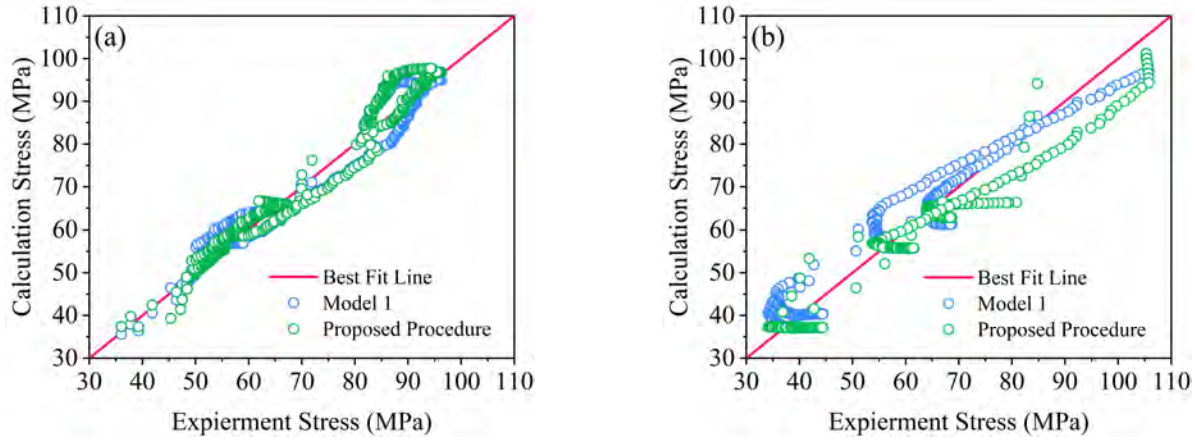

Fig. 12. The comparison between the accuracy of the three models for the dynamic variation states. (a) Z value increases cases; (b) Z value decreases cases.

Fig. 13. compares the recrystallization fraction calculated by the process proposed in this paper with the stress softening degree. Fig. 13. compares the predicted DRX fraction with the stress softening degree. The stress softening degree is calculated as Eq. (19).

$$X_{DRX} = \frac{\sigma_{DRV} - \sigma}{\sigma_{SAT} - \sigma_{SS}} \tag{21}$$

Fig. 13. (a), (c), (e), (g) show the case of increasing Z value (increasing strain rate or decreasing deformation

temperature). Z value increases during deformation lead to significant suppression of the DRX behavior. The DRX and stress softening degree curves plateau under dynamic variation states. The strain rate increases or deformation temperature decrease during steady-state deformation, leading to dislocations and substructures forming between grain boundaries (Chen et al., 2019; Liu, 2023). These dislocations or substructures can hinder the boundary motion, obstructing the nucleation and growth of recrystallized grains through strain-induced boundary migration. As the deformation proceeds, dislocations or substructures reach critical conditions. Under the strain-induced, grain boundaries will gradually bow out to be serrated. A new round of the DRX grain nucleation and growth process occurs. The model can describe the DRX behavior inhibition and the following activation process. Fig. 13. (b), (d), (f), (h) show the case of decreasing Z value (increasing strain rate or decreasing deformation temperature). Z value decreases during deformation lead to significant promotion of the DRX behavior. The DRX and stress softening degree curves dramatic increase under dynamic variation states. Dislocations accumulate in grains and at grain boundaries at high strain rates and low deformation temperatures. The strain rate decrease or deformation temperature increase can improve grain boundary migration ability. The previously accumulated dislocation, especially at grain boundaries, will provide a greater driving force for grain boundary migration and promote grain nucleation and growth under strain-induced grain boundary migration. As the deformation proceeds, dislocations annihilate during the formation and growth of DRX grains, engulfing the deformed grains until the DRX grain boundary migration and dislocation formation reach a new dynamic equilibrium. The model can describe the promotion DRX behavior process.

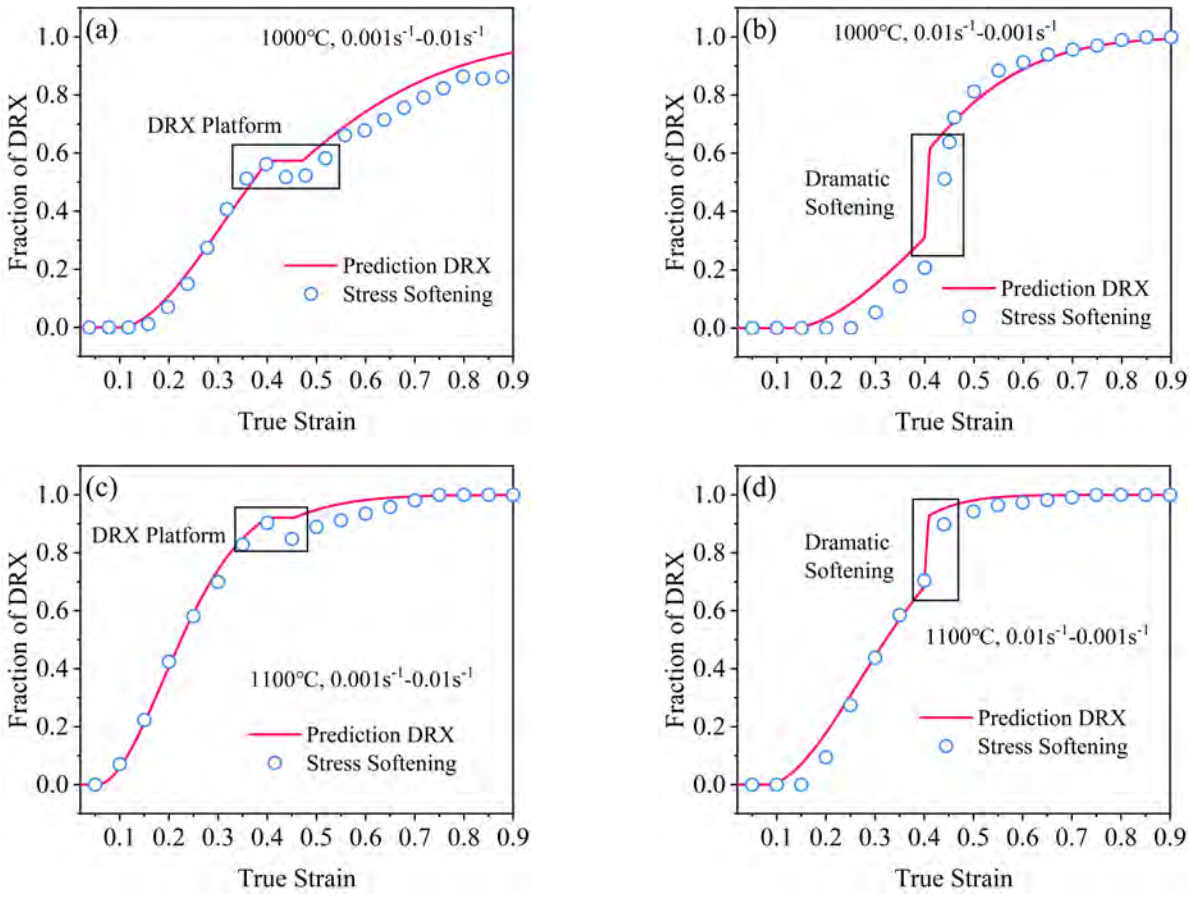

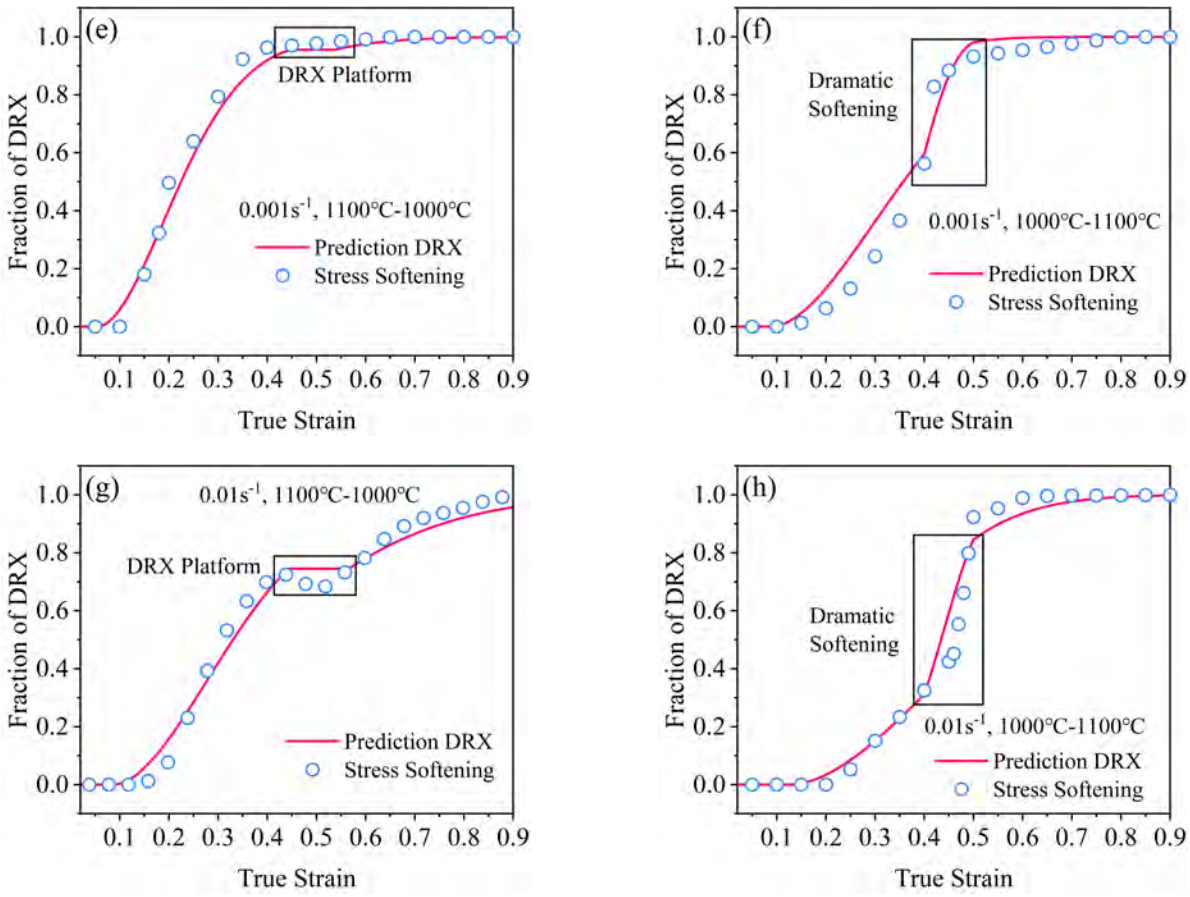

Fig. 13. The comparison between the predicted DRX fraction with the stress softening degree for the dynamic variation states. (a) 1000°C, and the strain rate transient increases from 0.001 s^{-1} to 0.01 s^{-1} at strain 0.4; (b) 1000°C, and the strain rate transient decreases from 0.01 s^{-1} to 0.001 s^{-1} at strain 0.4; (c) 1100°C, and the strain rate transient increases from 0.001 s^{-1} to 0.01 s^{-1} at strain 0.4; (d) 1100°C, and the strain rate transient decreases from 0.01 s^{-1} to 0.001 s^{-1} at strain 0.4; (e) 0.001s^{-1}, and the deformation temperature decreases from 1100℃ to 1000℃ from strain 0.4 to 0.41; (f) 0.001s^{-1}, and the deformation temperature increases from 1000℃ to 1100℃ from strain 0.4 to 0.41; (g) 0.01s^{-1}, and the deformation temperature decreases from 1100℃ to 1000℃ from strain 0.4 to 0.5; (h) 0.01s^{-1}, and the deformation temperature increases from 1000℃ to 1100℃ from strain 0.4 to 0.5.

3.3 Analysis of flow behavior under dynamic variation states

This section embeds the model 3 in a commercial finite element software to investigate the characteristics of metal plastic flow under a dynamic variation state. The coupling relationship between microstructure evolution, deformation resistance, and metal plastic flow is revealed.

This paper uses Deform-3D software to simulate the high-temperature deformation under the dynamic variation states. Fig. 14. shows the finite element model and boundary conditions. The finite element model is a 1/4 model, and the size of the indenter and specimen is consistent with the experiments. The indenter is set as a rigid object. The cylindrical specimen is set as a rigid-plastic object, and a hexahedral meshing with a mesh number of 10000 is performed. Considering the lubrication treatment, the friction between the indenter and the specimen is set to 0.3 shear friction (Peng et al., 2022b). Since the Gleeble experimental machine has an accurate and sensitive temperature control system, it can carry out automatic heating and cooling according to the temperature measured on the surface of the specimen so that the specimen has a stable temperature state during the test. The heat exchange between the specimen and the environment is considered negligible. Only the internal heat generation during the deformation process was considered. The constitutive relationship is embedded using the model 3 and is implemented through a secondary development technique. The deformation conditions are the same as the experiments. The indenter speed controls the

strain rate variation. On the other hand, the simulation ignores the inhomogeneity temperature distribution under temperature variation states and approximates that the temperature is uniform. This assumption is feasible through the introduction of the equipment temperature control capability and the comparison between the experimental and the simulation results.

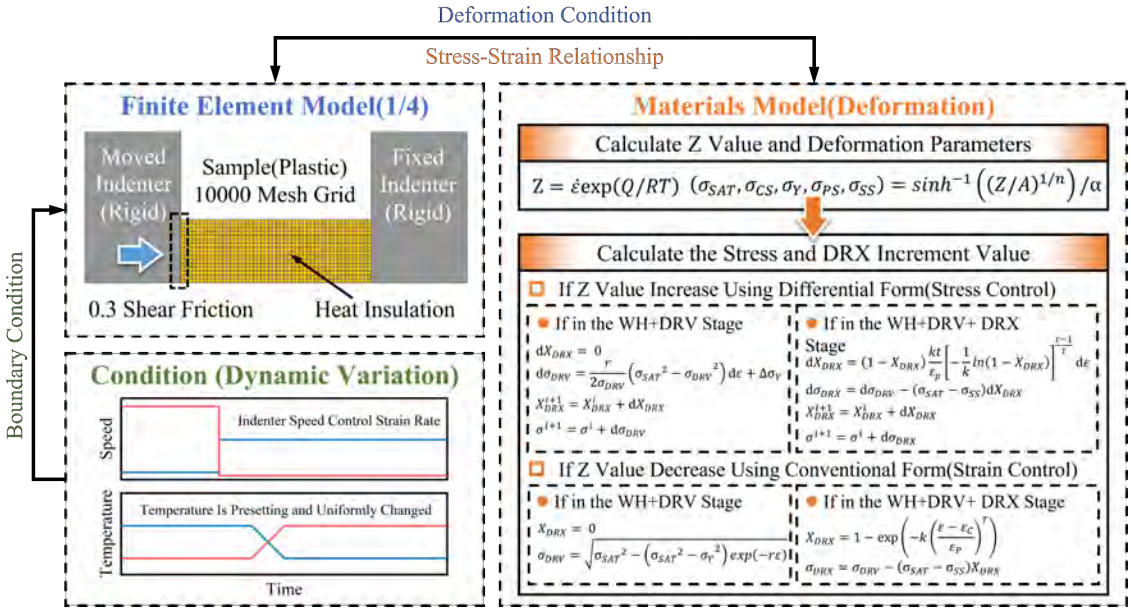

Fig. 14. The finite element model and boundary conditions.

Fig. 15. shows the load-time comparison between the experiment and simulation under different dynamic variation states. The simulated results agree well with the experimental results, indicating that the model can study the high-temperature deformation behavior under deformation conditions variation states.

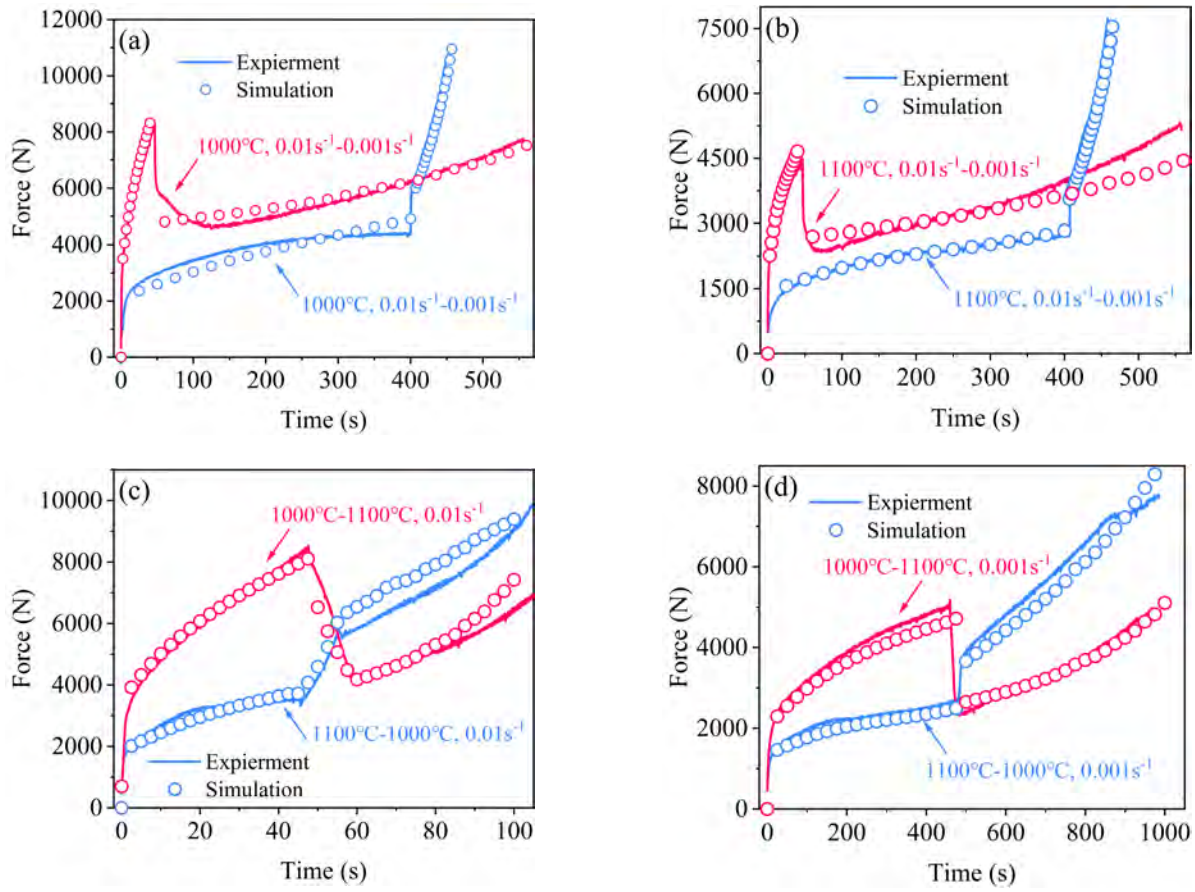

Fig. 15. The load-time comparison between the experiment and simulation under different dynamic variation states. a) strain rate dynamic increases or decreases at 1000°C; b) strain rate dynamic increases or decreases at 1100°C; c) temperature dynamic increase or decrease at $0.01s^{-1}$; d) temperature dynamic increase or decrease at $0.001s^{-1}$.

Fig. 16 (a), (b) shows the effective strain distribution at the beginning of the deformation conditions variation (true strain 0.4) and the end of the deformation (true strain 0.9) under dynamic variation states. The two cases are 1000°C, with transient changes of $0.001s^{-1}$-$0.01s^{-1}$ and $0.01s^{-1}$-$0.001s^{-1}$ at 0.4 true strain. Under strain rate increases case, the specimen is first deformed at 0.001 s^{-1} to 0.4 true strain. The center effective strain is 0.587, and the surface is 0.093. The strain rate then undergoes a transient increase from 0.001 s^{-1} to 0.01 s^{-1}. The specimen continues to deform to 0.9 true strain at 0.01 s^{-1}. After deformation, the center effective strain becomes 1.29, and the surface becomes 0.25. Under strain rate decreases case, the specimen is first deformed at 0.01 s^{-1} to 0.4 true strain. The center effective strain is 0.575, and the surface is 0.104. The strain rate then undergoes a transient decrease from 0.01 s^{-1} to 0.001 s^{-1}. The specimen continues to deform to 0.9 true strain at 0.001 s^{-1}. After deformation, the center effective strain becomes 1.32, and the surface becomes 0.233. Comparing the deformation distribution process, the transient decrease of strain rate promotes the deformation in the center. Fig.16. (c) shows the effective strain evolutions of the center and surface position in the above two cases. The pink solid/dashed lines are the center/surface effective strain evolutions for strain rate increases. The blue solid/dashed lines are the center/surface effective strain evolutions for strain rate decreases. Before the strain rate variation, the strain rate transient increase case has a lower initial strain rate. More deformation occurs in the center. When the strain rate variation occurs, the deformation in the center of the strain rate decrease case gradually exceeds that of the strain rate increase case.

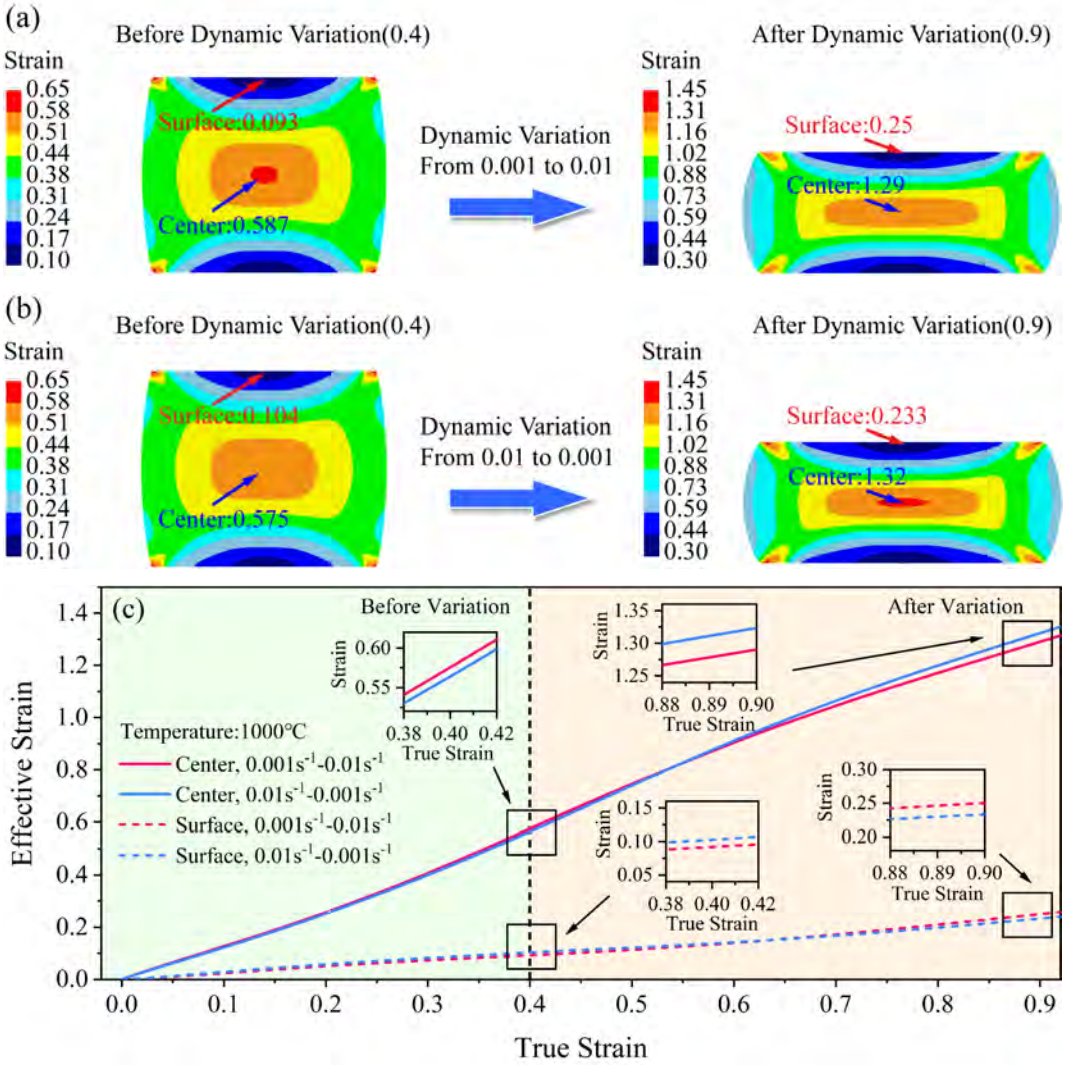

Fig. 16. The effective strain distribution at the beginning of the deformation conditions variation (true strain 0.4) and the end of the deformation (true strain 0.9) under dynamic variation states (a) 1000°C, with transient changes of $0.001s^{-1}$-$0.01s^{-1}$ at 0.4 true strain; (b) 1000°C, with transient changes of $0.01s^{-1}$-$0.001s^{-1}$ at 0.4 true strain.; (c) the effective strain evolutions of the center and surface position in the above two cases.

Fig. 17. (a), (b) compare the center and surface effective strain of strain rate increases and decreases cases at the beginning of the deformation conditions variation (true strain 0.4) and the end of the deformation (true strain 0.9) under different deformation temperatures (1000℃ and 1100℃). Fig. 17. (c), (d) compare the center and surface effective strain of deformation temperature increases and decreases cases at the beginning of the deformation conditions variation (true strain 0.4) and the end of the deformation (true strain 0.9) under different strain rates ($0.01s^{-1}$ and $0.001s^{-1}$). The decrease in strain rate and the increase in deformation temperature during deformation promote the deformation in the center.

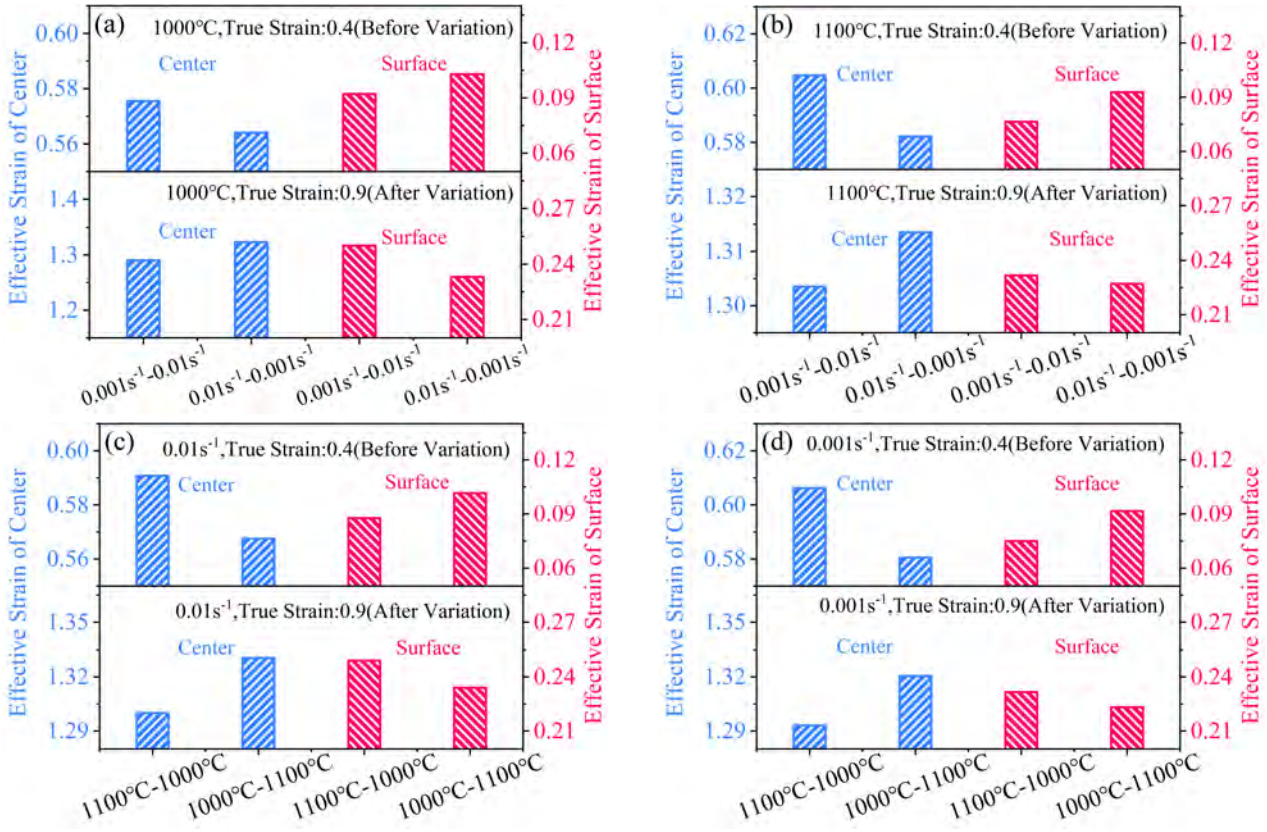

Fig. 17. The center and surface effective strain at the beginning of the deformation conditions variation (true strain 0.4) and the end of the deformation (true strain 0.9). (a)1000℃, $0.001s^{-1}$-$0.01s^{-1}$ and $0.01s^{-1}$-$0.001s^{-1}$; (b) 1100°C, $0.001s^{-1}$-$0.01s^{-1}$ and $0.01s^{-1}$-$0.001s^{-1}$; (c) $0.01s^{-1}$,1000℃-1100℃ and 1100℃-1000℃; (d) $0.001s^{-1}$,1000℃-1100℃ and 1100℃-1000℃.

The essence of the deformation distribution is the competitive coordination of deformation resistance and indenter-sample interfacial friction. Fig. 18. (a) shows the effective strain distribution from surface to center under the deformation condition in Fig. 16. (a). The specimen exhibited a significant deformation gradient from the surface to the center. The deformation is more concentrated in the center. Many studies have demonstrated the reasons: interfacial friction between the surface and the indenter hinders the lateral flow of the metal (Jia et al., 2019; Shi and Chen, 2016). A Under the volume invariance principle, the surface compression deformation is also restrained. As the distance from the surface increases, the constraining effect of interfacial friction decreases and the metal near the center is in a free-deformation state. The obstructed plastic deformation of the surface will be transferred to the center than the specimen shows the macroscopic shape of a bulging belly. Fig. 18. (a) shows the shape of the surface and center elements after deformation. The center element is flatter and undertakes more deformation. When the center exhibits more significant

deformation resistance under deformation conditions, the obstruction of interfacial friction on the surface metal flow is relatively weakened. The deformation distribution relationship between the center and the surface changes and part of the center deformation is transferred to the surface metal, hindering the deformation in the center. When the center deformation resistance is small, the obstruction of interfacial friction on the surface metal flow dominates and deformation is easily in the center. Fig. 18. (b) shows the surface and center effective strain versus Z value for deformation to a true strain of 0.9 at different constant deformation temperatures (1000°C, 1050°C, 1100°C) and strain rates ($0.1s^{-1}$, $0.01s^{-1}$, $0.001s^{-1}$). As the Z value increases, the deformation temperature decreases, and the strain rate increases. The center deformation resistance quickly reaches a higher state, weakening the deformation penetration ability under interface friction. The center deformation is reduced.

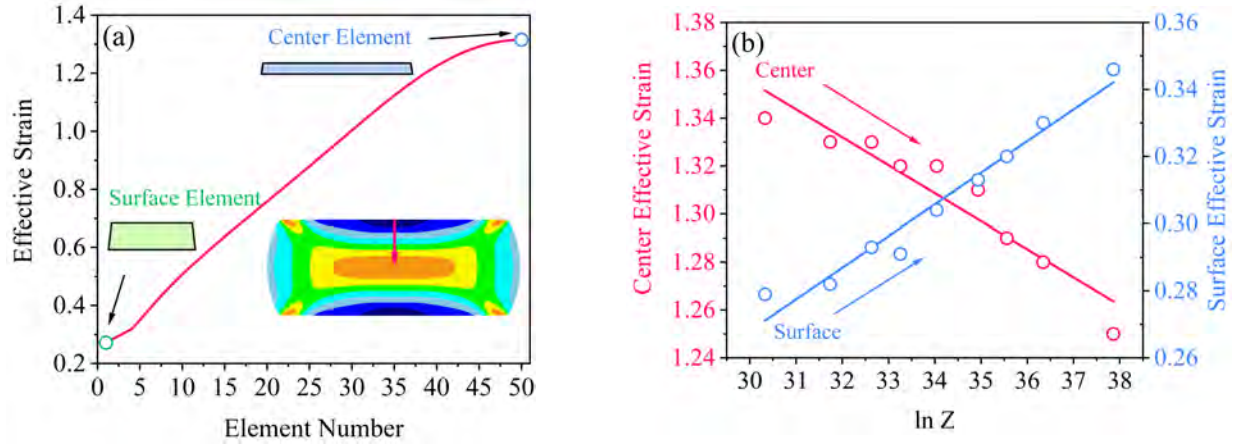

Fig. 18. Non-uniform strain distribution during deformation. (a) the effective strain distribution from surface to center under the deformation condition in Fig. 17. (a); (b) the surface and center effective strain versus Z value for deformation to a true strain of 0.9 at different constant deformation temperatures (1000°C, 1050°C, 1100°C) and strain rates ($0.1s^{-1}$, $0.01s^{-1}$, $0.001s^{-1}$).

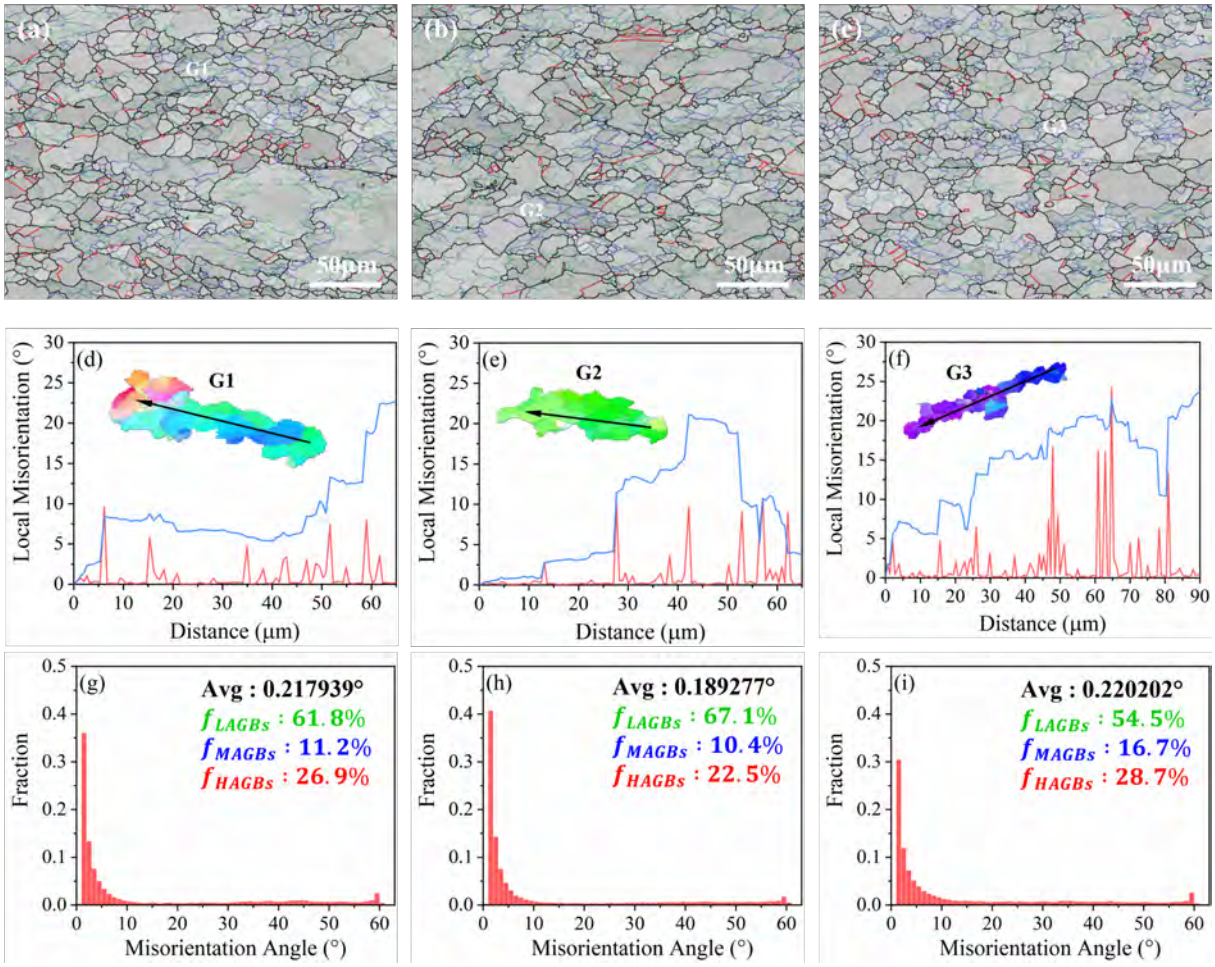

Fig. 19. Microstructure evolution under a deformation condition that strain rate transient increases from 0.001s^{-1} to 0.01s^{-1} with 1000℃ at different true strain (0.4, 0.6, 0.9). (a)-(c) Grain boundary map; (d)-(f) The local and cumulative misorientation statistics; (g)-(i) Grain boundary statistics.

EBSD characterization is used to further reveal the relationship between microstructure evolution, hardening and softening behavior, and plastic flow of metals under dynamic changes in deformation conditions. The procedure of the EBSD experiment can be found in the previous study (Liu, 2023). Fig. 19. (a)-(c) shows the GB distribution at 1000°C for three strains at 0.4, 0.6, and 0.9 during the transient change of strain rate from 0.001 s^{-1} to 0.01 s^{-1}, which occurs at 0.4 strain. The low-angle(2°-5°), medium-angle(5°-15°), high-angle grain(> 15°) boundaries and $\sum 3$ twins are shown by green, blue, black, and red lines, respectively. When deformed at 0.001s^{-1} to 0.4 strain, a considerable amount of substructure is attached at most deformed grains' grain boundaries. Some of the original grain boundaries bulge toward the adjacent grains. Sub-boundary networks mixed with low-angle grain boundaries and medium-angle grain boundaries inside a few deformed grains. The current state exhibits a softening mechanism dominated by DDRX. When the strain rate is transiently changed from 0.001s^{-1} to 0.01s^{-1} and further deformed to 0.6 strain, more sub-grains are formed inside the deformed grains. When the deformation continues at 0.01s^{-1} to 0.9 strain, discontinuous high-angle grain boundaries mixed with medium-angle grain boundaries are formed inside some deformed grains. Almost no $\sum 3$ twin structures are formed inside the DRX grains, which implies that the current state softening mechanism undergoes a transition from DDRX to CDRX. Fig. 19. (d)-(f) shows the local and cumulative misorientation statistics along arrows in different grains for the corresponding conditions (a)-(c). with the deformation proceeding after the transient increase in strain rate, the local misorientation angle exceeding 10-15° occurs more frequently, indicating the formation of denser high-angle and medium-angle grain boundaries. Fig. 19. (g)-(i) shows the statistics of the grain boundary ratio for the corresponding conditions of (a)-(c). When deforming at 0.001s-1 to 0.4 strain, the average grain

boundary angle is 0.217939°, and the percentage of low-angle, medium-angle, and high-angle grain boundaries is 61.8%, 11.2%, and 26.9%. When the strain rate transiently increases to 0.01s-1 and continues to deform to 0.6, the average grain boundary angle is 0.189277°, and the percentage of low-angle, medium-angle, and high-angle grain boundaries is 67.1%, 10.4%, and 22.5%. The transient increase in strain rate leads to an increase in the percentage of low-angle grain boundaries and a decrease in the percentage of high-angle grain boundaries. When continuing the deformation to 0.9 at 0.01s-1, the average grain boundary angle is 0.220202°, and the percentage of low-angle, medium-angle, and high-angle grain boundaries is 54.5%, 16.7%, and 28.7%. The decrease in low-angle grain boundaries and the increase in medium-angle and high-angle grain boundaries also reflect a softening mechanism dominated by CDRX.

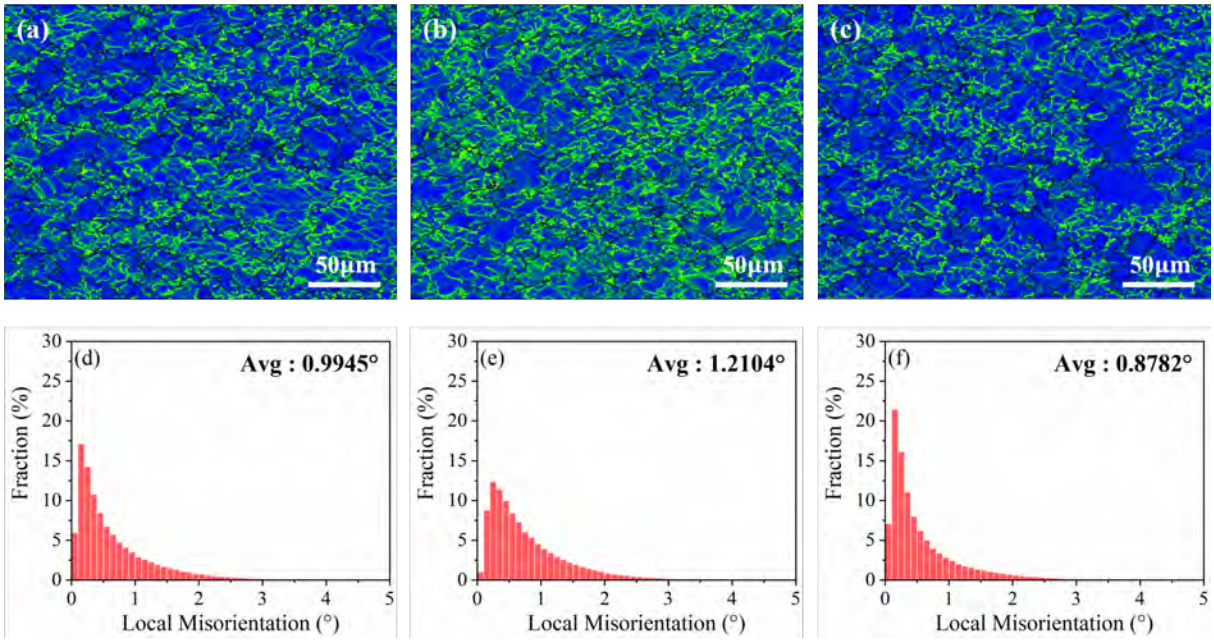

Fig. 20. Deformation energy statistics under a deformation condition that strain rate transient increases from $0.001s^{-1}$ to $0.01s^{-1}$ with 1000℃ at different true strain (0.4, 0.6, 0.9). (a)-(c) Local misorientation angle map; (d)-(f) The local misorientation statistics.

Fig. 20. (a)-(c) shows the LAM at 1000°C for three strains at 0.4, 0.6, and 0.9 during the transient change of strain rate from $0.001s^{-1}$ to $0.01s^{-1}$, which occurs at 0.4 strain, and the statistical values are given by (d)-(f). When deforming at $0.001s^{-1}$ to 0.4 strain, the average LAM is 0.9945°. As the strain rate transiently increases to $0.01s^{-1}$ and deforms to 0.6, the average LAM value increases to 1.2104°. The transient increase in strain rate suppresses the softening effect, and the rapid accumulation of dislocations within the grain increases LAM. The average LAM value decreases to 0.8782° when the deformation continues at $0.01s^{-1}$ for 0.9. The rapid accumulation of dislocation density and the substructure inside the grain gradually shifts toward high-angle grain boundaries. The LAM within the grain decreases under the CDRX-dominated softening mechanism.

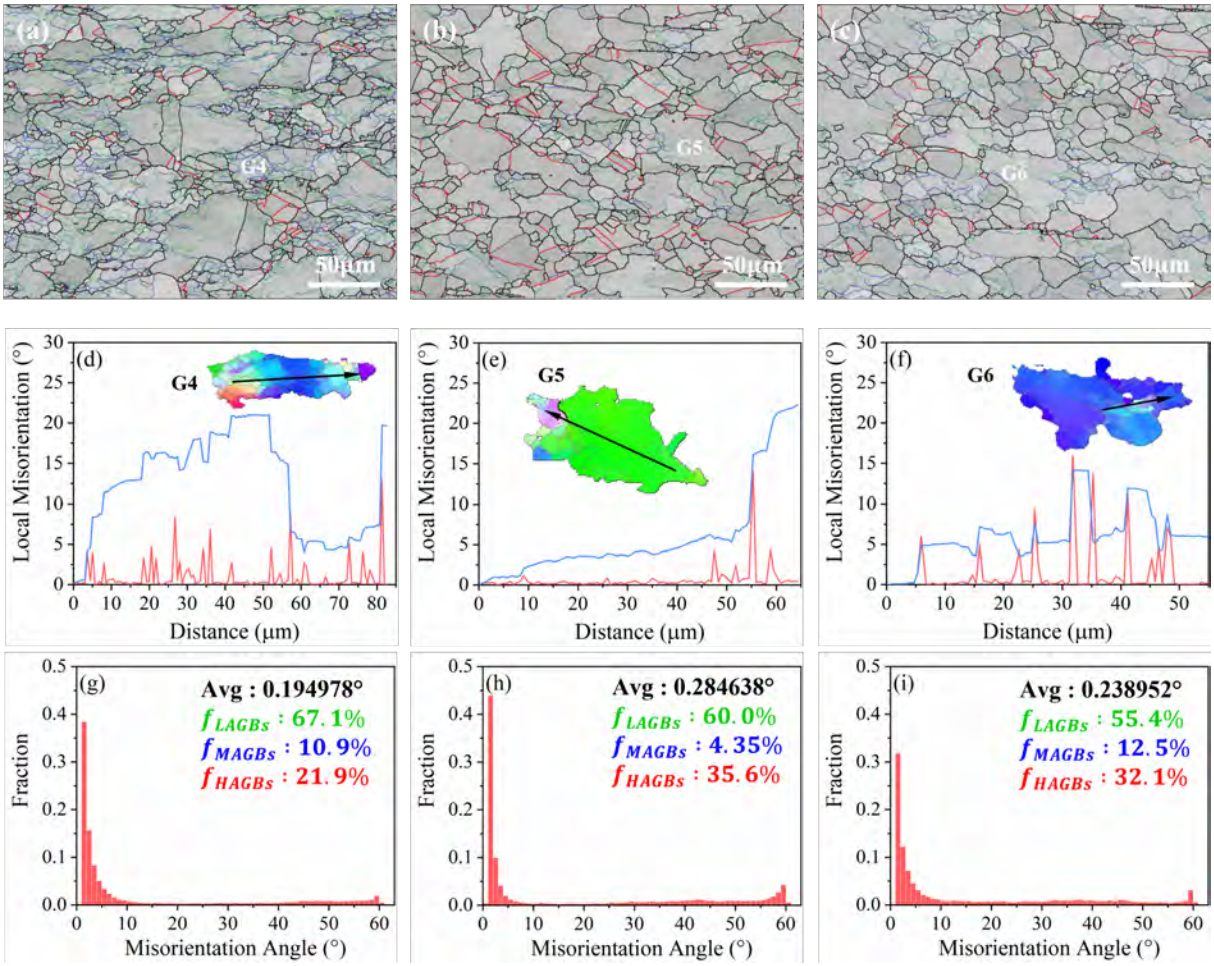

Fig. 21. Microstructure evolution under a deformation condition that strain rate transient decreases from $0.01s^{-1}$ to $0.001s^{-1}$ with 1000℃ at different true strain (0.4, 0.6, 0.9). (a)-(c) Grain boundary map; (d)-(f) The local and cumulative misorientation statistics; (g)-(i) Grain boundary statistics.

Fig. 21. (a)-(c) shows the GB distribution at 1000°C for three strains at 0.4, 0.6, and 0.9 during the transient change of strain rate from 0.01 s^{-1} to 0.001 s^{-1}, which occurs at 0.4 strain. When deformed at $0.01s^{-1}$ to 0.4 strain, a considerable amount of substructure is attached at most deformed grains' grain boundaries. Sub-boundary networks mixed with low-angle grain boundaries and medium-angle grain boundaries inside a few deformed grains. The current state exhibits a softening mechanism dominated by CDRX. When the strain rate is transiently changed from $0.01s^{-1}$ to $0.001s^{-1}$ and further deformed to 0.6 strain, sub-grains formed before disappeared rapidly. A large number of $\sum 3$ twins were formed inside the grains. When the deformation continues at $0.001s^{-1}$ to 0.9 strain, the number of $\sum 3$ twin decreases and substructures reformed inside grains. These phenomena imply that the dislocation structure accumulated at high strain rates provides energy for strain-induced grain boundary migration. After the strain rate transiently decreases, the grain boundaries have enough time to swallow neighboring grains driven by substructures and dislocations. However, as deformation continues at low strain rates, the energy accumulated at high strain rates rapidly decreases. It cannot support strain-induced grain boundary migration behavior. Substructures within the grains re-form to balance the dislocation proliferation. The recrystallization mechanism undergoes a shift from CDRX to DDRX to CDRX. Fig. 21. (d)-(f) shows the local and cumulative misorientation statistics along arrows in different grains for the corresponding conditions (a)-(c). Local orientation differences within the deformed grains exceed 10-15° frequently when deforming at $0.01s^{-1}$ to 0.4 strain. When the strain rate decreases to $0.001s^{-1}$, and deformation continues to 0.6, there are almost no mid-angle and high-angle grain boundaries inside the grains. After continuing deformation to 0.9, the stepped cumulative misorientation and the recurring local misorientation exceeding 5-15° indicate the formation

of well-developed sub-grains again. Fig. 21. (g)-(i) shows the statistics of the grain boundary ratio for the corresponding conditions of (a)-(c). When deforming at $0.01s^{-1}$ to 0.4 strain, the average grain boundary angle is 0.194978°, and the percentage of low-angle, medium-angle, and high-angle grain boundaries is 67.1%, 10.9%, and 21.9%. When the strain rate transiently decreases to $0.001s^{-1}$ and continues to deform to 0.6, the average grain boundary angle is 0.284638°, and the percentage of low-angle, medium-angle, and high-angle grain boundaries is 60.0%, 4.35%, and 35.6%. The transient decrease in strain rate significantly reduces the proportion of low-angle and medium-angle grain boundaries and increases the proportion of high-angle grain boundaries. When continuing the deformation to 0.9 at $0.001s^{-1}$, the average grain boundary angle is 0.238952°, and the percentage of low-angle, medium-angle, and high-angle grain boundaries is 55.4%, 12.5%, and 23.7%. The further decrease in the low-angle grain boundaries and the increase in the proportion of medium-angle grain boundaries indicate an increase in the misorientation angle due to the continued absorption of dislocations by the low-angle grain boundaries as the deformation proceeds.

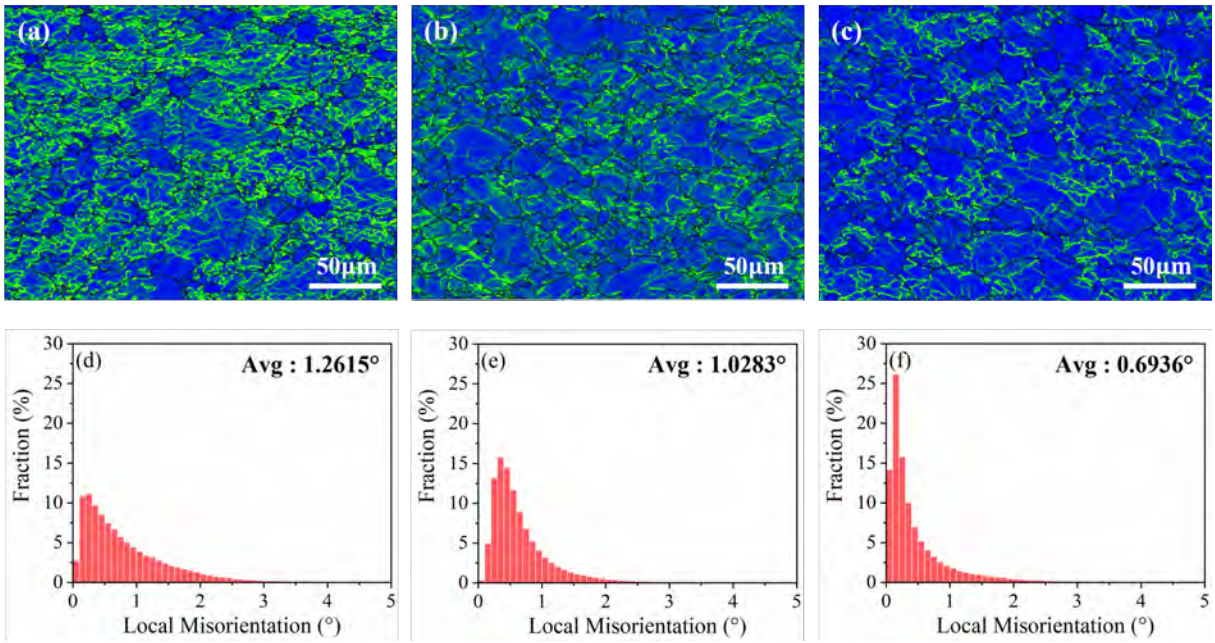

Fig. 22. Deformation energy statistics under a deformation condition that strain rate transient decreases from $0.01s^{-1}$ to $0.001s^{-1}$ with 1000℃ at different true strain (0.4, 0.6, 0.9). (a)-(c) Local misorientation angle map; (d)-(f) The local misorientation statistics.

Fig. 22. (a)-(c) shows the LAM at 1000°C for three strains at 0.4, 0.6, and 0.9 during the transient change of strain rate from $0.01s^{-1}$ to $0.001s^{-1}$, which occurs at 0.4 strain, and the statistical values are given by (d)-(f). When deforming at $0.01s^{-1}$ to 0.4 strain, the average LAM is 1.2615°. As the strain rate transiently decreases to $0.001s^{-1}$ and deforms to 0.6, the average LAM value decreases to 1.0283°. The average LAM value decreases to 0.6936° when the deformation continues at $0.001s^{-1}$ for 0.9.

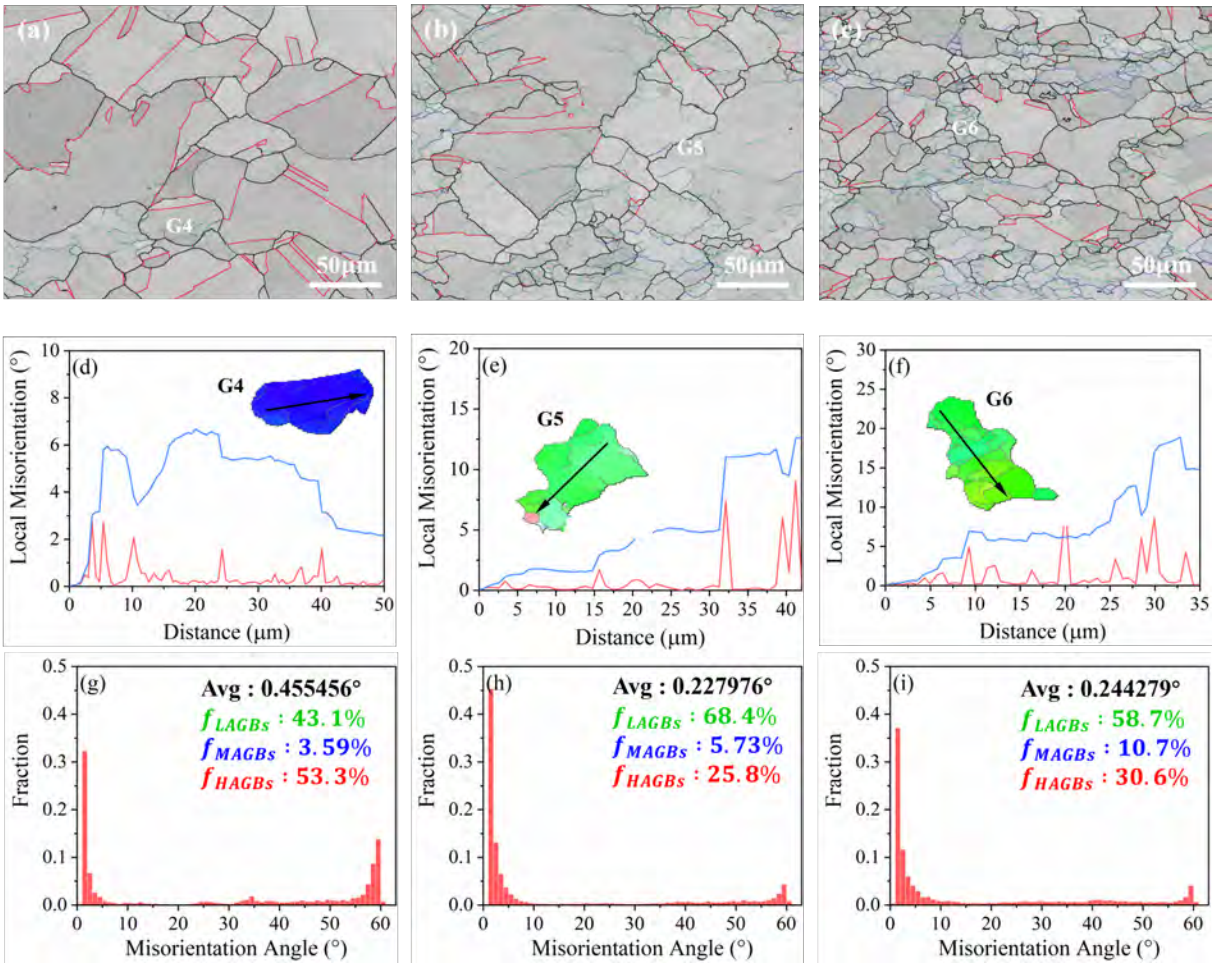

Fig. 23. Microstructure evolution under a deformation condition that temperature decreases from 1100℃ to 1000℃ with 0.001s^{-1} at different true strain (0.4, 0.6, 0.9). (a)-(c) Grain boundary map; (d)-(f) The local and cumulative misorientation statistics; (g)-(i) Grain boundary statistics.

Fig. 23. (a)-(c) shows the GB distribution at 0.001s^{-1} for three strains at 0.4, 0.6, and 0.9 during the change of temperature from 1100℃ to 1100℃. When deformed to 0.4 strain at 1100℃, the current state exhibits a softening mechanism dominated by DDRX. Both the huge amount of $\sum 3$ twin and some original grain boundaries bulge out under strain induced demonstrate it. When the Temperature is changed from 1100℃ to 1000℃ and further deformed to 0.6 strain, more sub-grains are formed inside the deformed grains. And the number of $\sum 3$ twin decreases. When the deformation continues at 1000℃ to 0.9 strain, discontinuous high-angle grain boundaries mixed with medium-angle grain boundaries are formed inside some deformed grains. The current state softening mechanism undergoes a transition from DDRX to CDRX. Fig. 23. (d)-(f) shows the local and cumulative misorientation statistics along arrows in different grains for the corresponding conditions (a)-(c). with the deformation proceeding after the decrease in temperature, the local misorientation angle exceeding 10-15° occurs more frequently, indicating the formation of denser high-angle and medium-angle grain boundaries. Fig. 23. (g)-(i) shows the statistics of the grain boundary ratio for the corresponding conditions of (a)-(c). When deforming at 1100℃ to 0.4 strain, the average grain boundary angle is 0.455456°, and the percentage of low-angle, medium-angle, and high-angle grain boundaries is 43.1%, 3.59%, and 53.3%. When the temperature decreases to 1000℃ and continues to deform to 0.6, the average grain boundary angle is 0.227969°, and the percentage of low-angle, medium-angle, and high-angle grain boundaries is 68.4%, 5.73%, and 25.8%. The decrease in temperature leads to an increase in the percentage of low-angle grain boundaries and a decrease in the percentage of high-angle grain boundaries. When continuing the deformation to 0.9, the average grain boundary angle is 0.244279°, and the percentage of low-angle, medium-angle, and high-angle grain boundaries is 58.7%, 10.7%,

and 30.6%. The decrease in low-angle grain boundaries and the increase in medium-angle and high-angle grain boundaries also reflect a softening mechanism dominated by CDRX. After the temperature is reduced, the deformation proceeds, with a significant increase in small-angle grain boundaries and a significant decrease in large-angle grain boundaries. As the deformation continues, small-angle grain boundaries decrease, and large-angle and medium-angle grain boundaries increase. This is attributed to the larger grain size and lower internal dislocation density during high-temperature deformation. At the initial deformation stage after temperature reduction, many dislocations accumulate inside the grains due to the weakened atomic activation. The larger grain size provides space for the dislocation proliferation process and limits the formation of substructures. As the deformation continues, the large-sized grains formed at high temperatures continue to be compressed, the internal dislocation interactions are enhanced, and the medium- and large-angle grain boundaries increase.

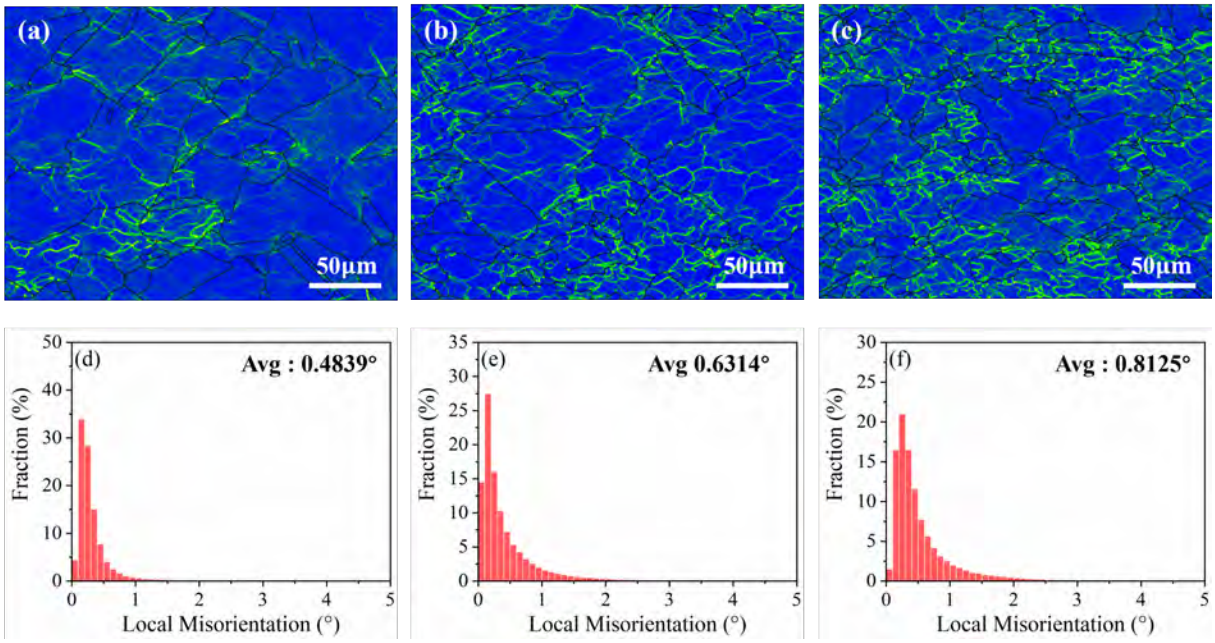

Fig. 24. Deformation energy statistics under a deformation condition that temperature decreases from 1100℃ to 1000℃ with $0.001s^{-1}$ at different true strain (0.4, 0.6, 0.9). (a)-(c) Local misorientation angle map; (d)-(f) The local misorientation statistics.

Fig. 24. (a)-(c) shows the LAM at $0.001s^{-1}$ for three strains at 0.4, 0.6, and 0.9 during the change of temperature from 1100℃ to 1000℃, and the statistical values are given by (d)-(f). When deforming at 1100℃ to 0.4 strain, the average LAM is 0.4839°. As the temperature decreases to 1000℃ and deforms to 0.6, the average LAM value increases to 0.6314°. The decrease in temperature suppresses the softening effect, and the rapid accumulation of dislocations within the grain increases LAM. And the average LAM value increases to 0.8125° when the deformation continues to 0.9.

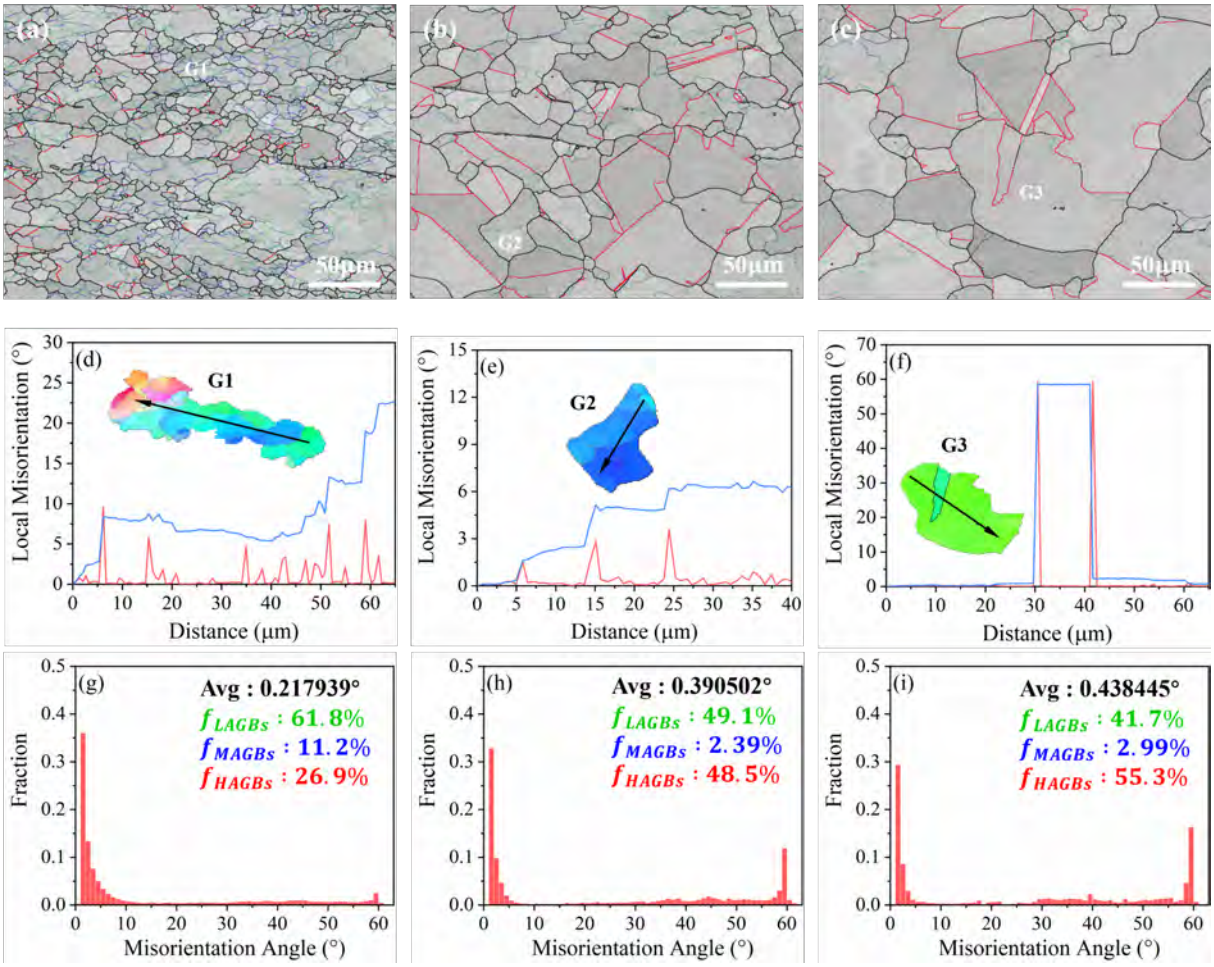

Fig. 25. Microstructure evolution under a deformation condition that temperature increases from 1000℃ to 1100℃ with 0.001s^{-1} at different true strain (0.4, 0.6, 0.9). (a)-(c) Grain boundary map; (d)-(f) The local and cumulative misorientation statistics; (g)-(i) Grain boundary statistics.

Fig. 25. (a)-(c) shows the GB distribution at 0.001s^{-1} for three strains at 0.4, 0.6, and 0.9 during the change of temperature from 1000℃ to 1100℃. When deformed at 1000℃ to 0.4 strain, a considerable amount of substructure is attached at most deformed grains' grain boundaries. Sub-boundary networks mixed with low-angle grain boundaries and medium-angle grain boundaries inside a few deformed grains. Many refined recrystallized grains are formed inside the grains and at the grain boundaries. The current state exhibits a softening mechanism dominated by CDRX. When the temperature changes from 1000℃ to 1100℃ and further deformed to 0.6 strain, sub-grains formed before disappeared rapidly. The grain size increases significantly, and many ∑3 twins form internally. When the deformation continues to 0.9 strain, the grain size increases further。 The temperature increase during deformation leads to the rapid growth of refined recrystallized grains formed at grain boundaries driven by the adjacent strain gradient and the temperature, which annexes the adjacent grains. The recrystallization mechanism undergoes a transition from CDRX to DDRX. Fig. 25. (d)-(f) shows the local and cumulative misorientation statistics along arrows in different grains for the corresponding conditions (a)-(c). Local orientation differences within the deformed grains exceed 10-15° frequently when deforming at 1000℃ to 0.4 strain. When the temperature increases to 1100℃, and deformation continues to 0.6 and 0.9, there are almost no mid-angle and high-angle grain boundaries inside the grains. Many substructures formed within the grains during the low-temperature deformation process recombine and decompose as the temperature rises, becoming the energy that drives the migration of the grain boundaries. Fig. 25. (g)-(i) shows the statistics of the grain boundary ratio for the corresponding conditions of (a)-(c). When deforming at 1000℃ to 0.4 strain, the average grain boundary angle is 0.217939°, and the percentage of low-angle, medium-angle, and high-angle

grain boundaries is 61.8%, 11.2%, and 26.9%. When the temperature increases to 1100 ℃ and continues to deform to 0.6, the average grain boundary angle is 0.390502°, and the percentage of low-angle, medium-angle, and high-angle grain boundaries is 49.1%, 2.39%, and 48.5%. The increase in temperature significantly reduces the proportion of low-angle and medium-angle grain boundaries and increases the proportion of high-angle grain boundaries. When continuing the deformation to 0.9 , the average grain boundary angle is 0.438445°, and the percentage of low-angle, medium-angle, and high-angle grain boundaries is 41.7%, 2.99%, and 55.3%. The further decrease in the low-angle grain boundaries and the increase in the proportion of high-angle grain boundaries indicate the grain growth as the grain boundary migration.

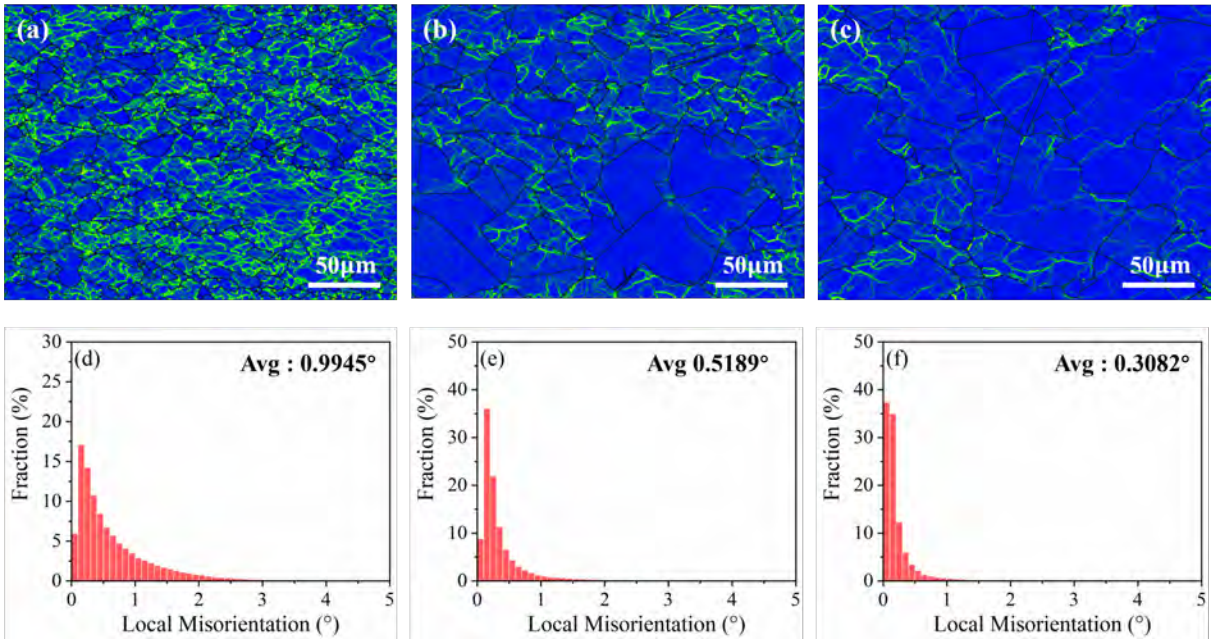

Fig. 26. Deformation energy statistics under a deformation condition that temperature increases from 1000℃ to 1100℃ with 0.001s^{-1} at different true strain (0.4, 0.6, 0.9). (a)-(c) Local misorientation angle map; (d)-(f) The local misorientation statistics.

Fig. 26. (a)-(c) shows the LAM at 0.001s^{-1} for three strains at 0.4, 0.6, and 0.9 during the change of temperature from 1000℃ to 1100℃, and the statistical values are given by (d)-(f). When deforming at 1000℃ to 0.4 strain, the average LAM is 0.9945°. As the strain rate transiently decreases to 1100℃ and deforms to 0.6, the average LAM value decreases to 0.5189°. The average LAM value decreases to 0.3082° when the deformation continues at 1100℃ for 0.9. Accompanied by grain growth under grain boundary migration, the deformation energy stored inside the grains is continuously consumed.

Based on the above analysis, the role of deformation conditions variation on strain distribution can be explained as follows. When deforming steadily at a high strain rate and low deformation temperature up to 0.4 true strain, the high dislocation proliferation rate leads to the accumulation of dislocations within the grains and between grain boundaries (especially at grain boundaries) (Chen et al., 2019). The high strain rate reduces the time for the original large-angle grain boundaries to bow out of the nucleation through strain-induced migration. In addition, the low deformation temperature weakens the ability of grain boundary migration under thermal activation and the DDRX behavior characterized by nucleation and growth is hindered. Moreover, it weakens the ability to form substructures by dislocations climbing, and cross-slip under DRV. The CDRX behavior characterized by substructure formation, rotation between substructures, forming large-angle grain boundaries, and migration processes is also hindered. WH dominates dislocation entanglement and interaction. The dislocation-dislocation and dislocation-boundary show strong interactions. The deformation resistance is at a high state, which inhibits the center deformation penetration under the interfacial friction. In this case, the strain rate decreases, or the deformation temperature increases during deformation.

Firstly, grain boundary migration gets more action time or vital driving ability. The DDRX nucleation and growth process is promoted. Secondly, dislocations are more likely to form substructures by climbing and cross-slip. The misorientation between adjacent substructures increases by continuously absorbing dislocations, forming large-angle grain boundaries, and migrating outward. Initial dislocations accumulated within and between grain boundaries provide more nucleation sites and substantial driving power for DDRX/CDRX. The deformed grains are replaced by recrystallized grains. The center deformation resistance is significantly reduced, the obstruction of interfacial friction dominates, and the deformation is more favorable to penetrate the center.

The DRV and DRX dynamic softening is significant when deformed steadily at a low strain rate and high deformation temperature up to 0.4 true strain. Accumulated dislocations within the deformed grains are reduced through DRX grain formation and growth. Under dynamic hardening and softening coordination, the deformation resistance is at a lower state. Interfacial friction obstruction dominates, and the deformation is more concentrated in the center. The strain rate increases or the deformation temperature decreases, promoting the partial slip system opening. WH dominates the dislocation proliferation within the grains and between grain boundaries. Dislocations accumulated at the original DRX grain boundaries weakened the deformation-induced grain boundary migration ability. The dynamic hardening and softening coordination are out of balance, and the dislocation density increases significantly. Until the formation of dislocations and substructures again reaches critical conditions. DDRX and CDRX behaviors occur again. The deformation resistance reaches equilibrium at a higher state, and the center deformation penetration is hindered. The obstruction of interfacial friction weakens, and the surface metal gradually assumes a certain degree of deformation.

4.Conclusion

This paper combines high-temperature deformation experiments, flow stress analysis, and numerical simulation to study the high-temperature deformation behavior of 316L austenitic stainless steel under a dynamic variation state. The critical conclusions are as follows:

1) During the deformation process, dynamic changes in deformation conditions can cause a transient increase or decrease in stress. Moreover, stress gradually enters a steady state in the subsequent deformation process. Different material properties and deformation conditions will lead to different evolutionary patterns of stress under a dynamic variation state. The Z value can unify the effects of material properties and deformation conditions.

2) Combined with the DRV-DRX staged phenomenal model, a flow stress calculation procedure is proposed and applicable for dynamic changes in deformation conditions. The calculation procedure exhibits similar accuracy to the complex physical-based constitutive model.

3) Dynamic changes in deformation conditions affect the heart deformation resistance during the deformation process, affecting the competitive coordination of material deformation resistance and indenter-sample interfacial friction and ultimately affecting the deformation distribution. When the Z value decreases during the dynamic variation state, the heart's intense softening action promotes the deformation penetration into the heart. When the Z value increases during the dynamic variation state, the intense hardening effect hinders the progression of deformation toward the center.

4) The microstructure evolution during dynamic variation states is revealed by EBSD characterization. The deformation conditions variation results in the hardening and softening mechanism changing. Especially, at 1000℃ the strain rate changing from $0.01s^{-1}$ to $0.001\ s^{-1}$ results in the recrystallization mechanism changing from CDRX to DDRX to CDRX.

Acknowledgments

This work was supported by Regional Joint Funds of the National Natural Science Foundation of China (Grant No. U20A20289); The General Program of National Natural Science Foundation of China (Grant No. 52075471、52075473); Innovative Research Groups Project of the Natural Science Foundation of Hebei Province (Grant No. E2021203011); Excellent Youth Science Foundation of Hebei Province (Grant No. E2021203190); Innovative

Capacity Cultivation Funding Project for Postgraduates of Hebei Province (Grant No. CXZZSS2023040).

Reference

Abbod, M.F., Sellars, C.M., Tanaka, A., Linkens, D.A., Mahfouf, M., 2008. Effect of changing strain rate on flow stress during hot deformation of Type 316L stainless steel. Materials Science and Engineering: A 491, 290–296. https://doi.org/10.1016/j.msea.2008.02.005

Buzolin, R.H., Lasnik, M., Krumphals, A., Poletti, M.C., 2021. 65.A dislocation-based model for the microstructure evolution and the flow stress of a Ti5553 alloy. International Journal of Plasticity 136, 102862. https://doi.org/10.1016/j.ijplas.2020.102862

Chen, W., Hu, B., Jia, C., Zheng, C., Li, D., 2019. Continuous dynamic recrystallization during the transient deformation in a Ni-30%Fe austenitic model alloy. Materials Science and Engineering: A 751, 10–14. https://doi.org/10.1016/j.msea.2019.02.048

Chen, Z.-J., Lin, Y.C., He, D.-G., Lou, Y.-M., Chen, M.-S., 2021. 21.A unified dislocation density-based model for an aged polycrystalline Ni-based superalloy considering the coupled effects of complicate deformation mechanisms and initial δ phase. Materials Science and Engineering: A 827, 142062. https://doi.org/10.1016/j.msea.2021.142062

De Sousa Sulzbach, G.A., Goncalves Rodrigues, M.V., Rodrigues, S.F., Macedo, G.M.E., Gomes De Abreu, H.F., Aranas, C., Reis, G.S., Silva, E.S., 2022. Constitutive analysis of stress–strain curves in dynamic softening of high Nb- and N-containing austenitic stainless-steel biomaterial. Journal of Materials Research and Technology 19, 4939–4956. https://doi.org/10.1016/j.jmrt.2022.07.036

Gao, S., Sang, Y., Li, Q., Sun, Y., Wu, Y., Wang, H., 2022. Constitutive modeling and microstructure research on the deformation mechanism of Ti-6Al-4V alloy under hot forming condition. Journal of Alloys and Compounds 892, 162128. https://doi.org/10.1016/j.jallcom.2021.162128

Graetz, K., Miessen, C., Gottstein, G., 2014. Analysis of steady-state dynamic recrystallization. Acta Materialia 67, 58–66. https://doi.org/10.1016/j.actamat.2013.12.005

Gui, Y., Ouyang, L., Xue, Y., Li, Q., 2021. 57.Effect of thermo-mechanical processing parameters on the dynamic restoration mechanism in an Mg-4Y-2Nd-1Sm-0.5Zr alloy during hot compression. Journal of Materials Science & Technology 90, 205–224. https://doi.org/10.1016/j.jmst.2021.02.036

Han, L., Zhu, X., Wei, D., Yu, Y., Wang, G., 2023. Construction of an Arrhenius constitutive model for Mg-Y-Nd-Zr-Gd rare earth magnesium alloy based on the Zener-Hollomon parameter and objective evaluation of its accuracy in the twinning-rich intervals. Journal of Magnesium and Alloys S221395672300021X. https://doi.org/10.1016/j.jma.2023.01.008

He, D., Yan, X.-T., Lin, Y.C., Zhang, S., Chen, Z.-J., 2022. 50.Microstructure evolution and constitutive model for a Ni-Mo-Cr base alloy in double-stages hot compression with step-strain rates. Materials Characterization 194, 112385. https://doi.org/10.1016/j.matchar.2022.112385

He, D.-G., Lin, Y.C., Chen, J., Chen, D.-D., Huang, J., Tang, Y., Chen, M.-S., 2018. Microstructural evolution and support vector regression model for an aged Ni-based superalloy during two-stage hot forming with stepped strain rates. Materials & Design 154, 51–62. https://doi.org/10/ghtbs4

Jia, W., Ma, L., Le, Q., Zhi, C., Liu, P., 2019. 71.Deformation and fracture behaviors of AZ31B Mg alloy at elevated temperature under uniaxial compression. Journal of Alloys and Compounds 783, 863–876. https://doi.org/10/gqmp9w

Li, M., Shi, Z.-Z., Wang, Q., Cheng, Y., Wang, L.-N., 2023. Zn–0.8Mn alloy for degradable structural applications: Hot compression behaviors, four dynamic recrystallization mechanisms, and better elevated-temperature strength. Journal of Materials Science & Technology 137, 159–175. https://doi.org/10.1016/j.jmst.2022.08.002

Lin, Y.C., Chen, X.-M., 2011. 13.A critical review of experimental results and constitutive descriptions for metals and alloys in hot working. Materials & Design 32, 1733–1759. https://doi.org/10/cbmbjp

Lin, Y.C., Dong, W.-Y., Zhou, M., Wen, D.-X., Chen, D.-D., 2018. A unified constitutive model based on dislocation density for an Al-Zn-Mg-Cu alloy at time-variant hot deformation conditions. Materials Science and Engineering: A 718, 165–172. https://doi.org/10.1016/j.msea.2018.01.109

Liu, C., 2023. 41.Modeling and characterization of dynamic recrystallization under variable deformation states. International Journal of Mechanical Sciences 22.

Liu, C., Barella, S., Peng, Y., Sun, J., Guo, S., Liang, S., Gruttadauria, A., Mapelli, C., 2022. Dynamic recrystallization behavior under steady and transient mutation deformation state. Materials Science and Engineering: A 143138. https://doi.org/10/gp24xn

Liu, C., Mapelli, C., Peng, Y., Barella, S., Liang, S., Gruttadauria, A., Belfi, M., n.d. 34.Dynamic Recrystallization Behavior of Low-Carbon Steel during the Flexible Rolling Process: Modeling and Characterization. steel research international 2100490.

Liu, Y.-X., Lin, Y.C., Zhou, Y., 2017. 2D cellular automaton simulation of hot deformation behavior in a Ni-based superalloy under varying thermal-mechanical conditions. Materials Science and Engineering: A 691, 88–99. https://doi.org/10.1016/j.msea.2017.03.039

Mishra, B., Singh, V., Sarkar, R., Mukhopadhyay, A., Gopinath, K., Madhu, V., Prasad, M.J.N.V., 2022. 56.Dynamic recovery and recrystallization mechanisms in secondary B2 phase and austenite matrix during hot deformation of Fe–Mn–Al–C-(Ni) based austenitic low-density steels. Materials Science and Engineering: A 842, 143095. https://doi.org/10.1016/j.msea.2022.143095

Ouyang, L., Luo, R., Gui, Y., Cao, Y., Chen, L., Cui, Y., Bian, H., Aoyagi, K., Yamanaka, K., Chiba, A., 2020. 53.Hot deformation characteristics and dynamic recrystallization mechanisms of a Co–Ni-based superalloy. Materials Science and Engineering: A 788, 139638. https://doi.org/10.1016/j.msea.2020.139638

Peng, Y., Guo, S., Liu, C., Barella, S., Liang, S., Gruttadauria, A., Mapelli, C., 2022a. 12.Dynamic recrystallization behavior of low-carbon steel during hot rolling process: modeling and simulation. Journal of Materials Research and Technology 20, 1266–1290. https://doi.org/10.1016/j.jmrt.2022.07.039

Peng, Y., Liang, S., Liu, C., Barella, S., Guo, S., Gruttadauria, A., Belfi, M., Liu, Y., Qu, X., Mapelli, C., 2022b. 70.Dynamic Recrystallization Behavior Under Inhomogeneous Thermomechanical Deformation State. steel research int. 2200574. https://doi.org/10.1002/srin.202200574

Puchi-Cabrera, E.S., Guérin, J.D., La Barbera-Sosa, J.G., Dubar, M., Dubar, L., 2018. Plausible extension of Anand's model to metals exhibiting dynamic recrystallization and its experimental validation. International Journal of Plasticity 108, 70–87. https://doi.org/10.1016/j.ijplas.2018.04.013

Puchi-Cabrera, E.S., Staia, M.H., Guérin, J.D., Lesage, J., Dubar, M., Chicot, D., 2014. An experimental analysis and modeling of the work-softening transient due to dynamic recrystallization. International Journal of Plasticity 54, 113–131. https://doi.org/10/f5sr8t

Savaedi, Z., Motallebi, R., Mirzadeh, H., 2022. 14.A review of hot deformation behavior and constitutive models to predict flow stress of high-entropy alloys. Journal of Alloys and Compounds 903, 163964. https://doi.org/10.1016/j.jallcom.2022.163964

Shi, C., Chen, X.-G., 2016. 72.Evolution of activation energies for hot deformation of 7150 aluminum alloys with various Zr and V additions. Materials Science and Engineering: A 650, 197–209. https://doi.org/10/gp5r2r

Su, Z., Sun, C., Wang, M., Qian, L., Li, X., 2022. 20.Modeling of microstructure evolution of AZ80 magnesium alloy during hot working process using a unified internal state variable method. Journal of Magnesium and Alloys 10, 281–294. https://doi.org/10/gqp72x

Svyetlichnyy, D.S., Majta, J., Nowak, J., 2013. A flow stress for the deformation under varying condition—internal and state variable models. Materials Science and Engineering: A 576, 140–148.

https://doi.org/10.1016/j.msea.2013.04.007

Wang, K., Song, K., Zhao, J., Cui, S., Peng, C., Wang, X., Wang, L., Liu, G., 2022. 35.Physically-based constitutive models for hot gas pressure forming of laser-welded titanium alloy blank. Journal of Manufacturing Processes 82, 501–515. https://doi.org/10.1016/j.jmapro.2022.08.021

Wang, M., 2020. 48.Experimental investigations and constitutive modeling of the dynamic recrystallization behavior of Inconel 740 superalloy. Materials Science 13.

Wang, M., Sun, C., Fu, M.W., Liu, Z., Wang, C., 2020. Microstructure and microtexture evolution of dynamic recrystallization during hot deformation of a nickel-based superalloy. Materials & Design 188, 108429. https://doi.org/10.1016/j.matdes.2019.108429

Wu, H., Xu, W., Shan, D., Jin, B.C., 2019. An extended GTN model for low stress triaxiality and application in spinning forming. Journal of Materials Processing Technology 263, 112–128. https://doi.org/10/gqpvwb

Xiao, Y.-W., Lin, Y.C., Jiang, Y.-Q., Zhang, X.-Y., Pang, G.-D., Wang, D., Zhou, K.-C., 2020. 64.A dislocation density-based model and processing maps of Ti-55511 alloy with bimodal microstructures during hot compression in α+β region. Materials Science and Engineering: A 790, 139692. https://doi.org/10.1016/j.msea.2020.139692

Xu, W., Yuan, C., Wu, H., Yang, Z., Yang, G., Shan, D., Guo, B., Jin, B.C., 2020. 67.Modeling of flow behavior and microstructure evolution for Mg-6Gd-5Y-0.3Zr alloy during hot deformation using a unified internal state variable method. Journal of Materials Research and Technology 9, 7669–7685. https://doi.org/10/gqp72z

Yang, P., Liu, C., Guo, Q., Liu, Y., 2021. 61.Variation of activation energy determined by a modified Arrhenius approach: Roles of dynamic recrystallization on the hot deformation of Ni-based superalloy. Journal of Materials Science & Technology 72, 162–171. https://doi.org/10.1016/j.jmst.2020.09.024

Zeng, R., Huang, L., Li, J., Li, H., Zhu, H., Zhang, X., 2019. 65.Quantification of multiple softening processes occurring during multi-stage thermoforming of high-strength steel. International Journal of Plasticity 120, 64–87. https://doi.org/10.1016/j.ijplas.2019.04.010

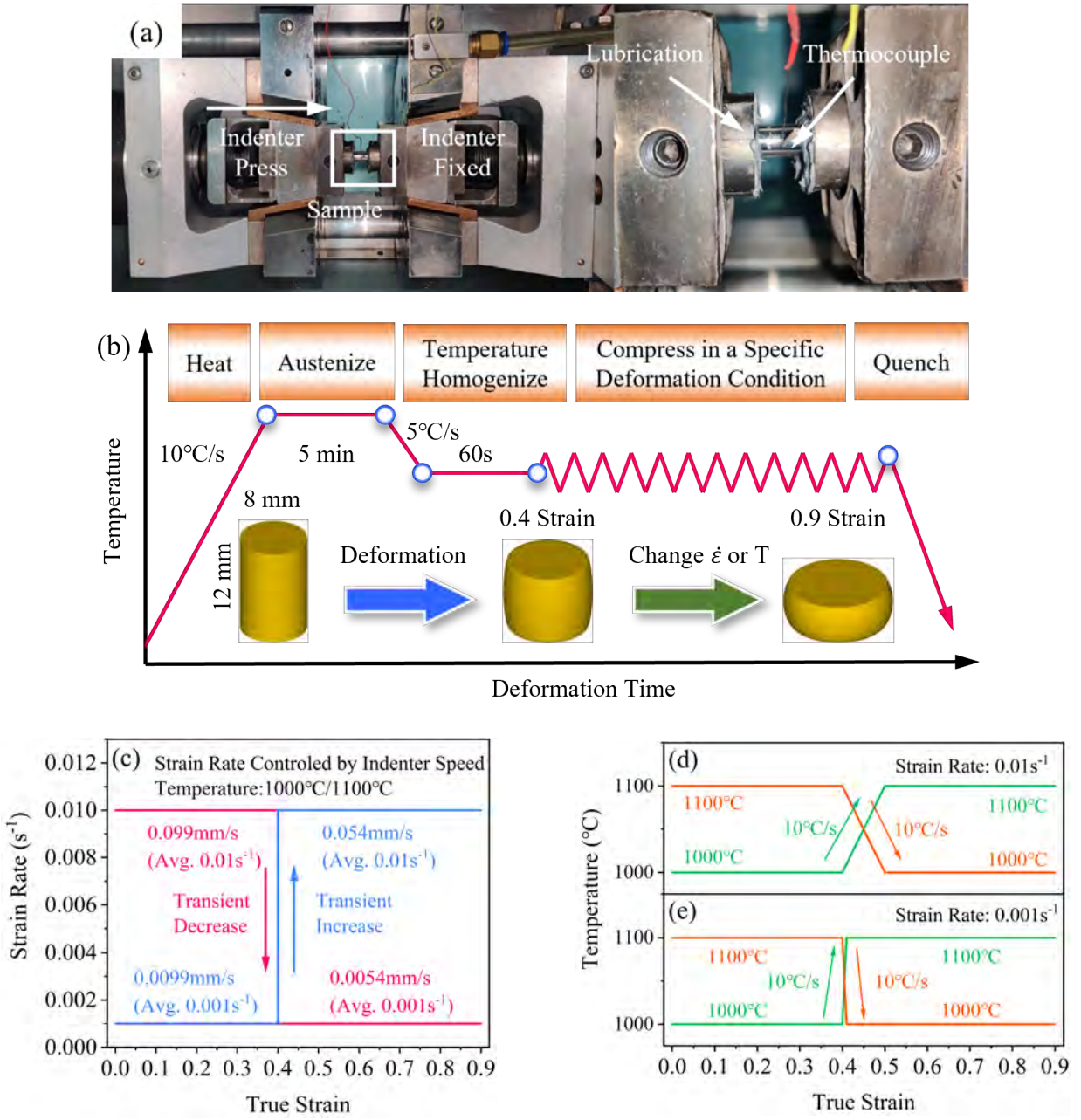

Fig. 1. (a) Experimental equipment; (b) Experimental procedure; (c) Experiment conditions for strain rate dynamic variation; (d) Experiment conditions for deformation temperature dynamic variation at 0.01 s^{-1}; (e) Experiment conditions for deformation temperature dynamic variation at 0.001 s^{-1}.

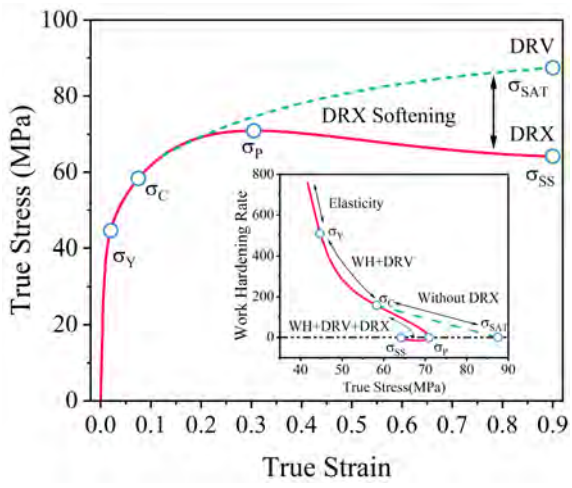

Fig. 2. Schematic diagram of stress evolution during high-temperature deformation.

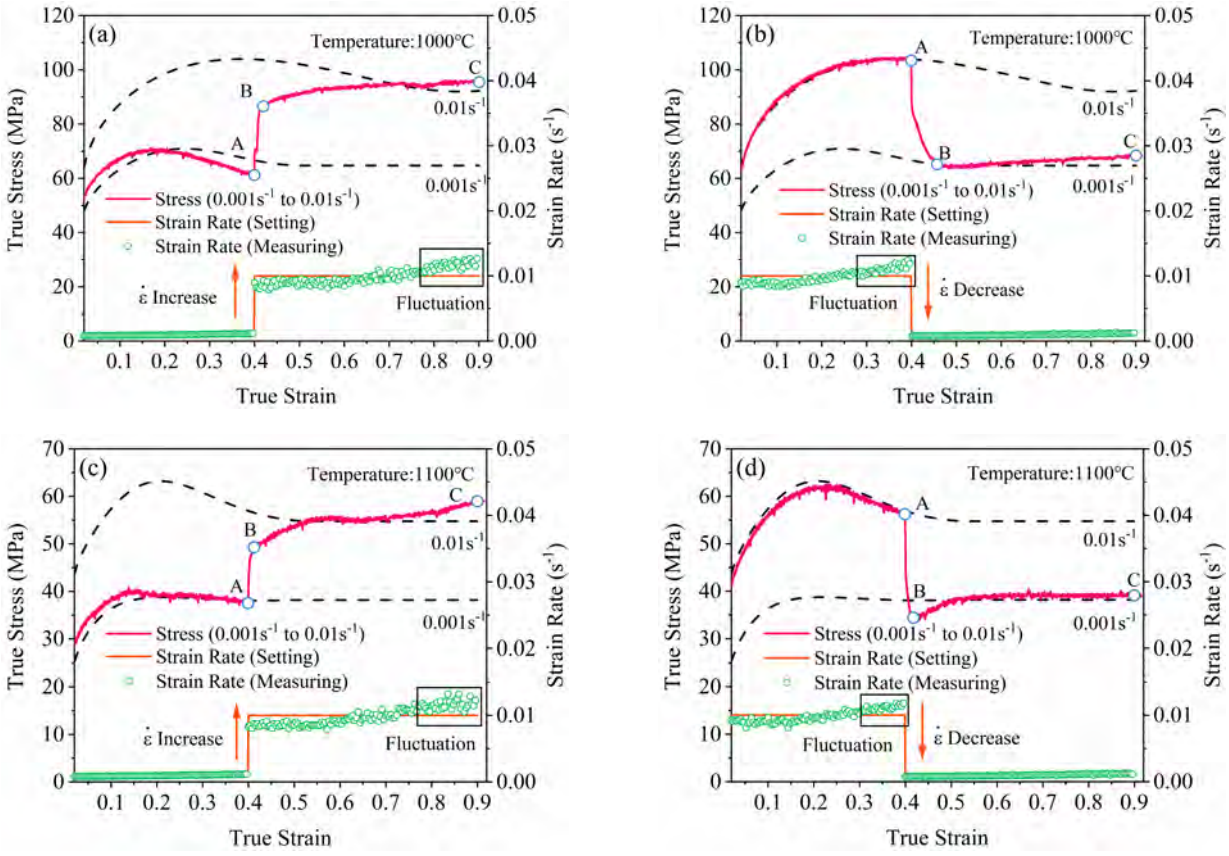

Fig. 3. Stress-strain curves under strain rate transient variation state. (a) 1000°C, and the strain rate transient increases from 0.001 s^{-1} to 0.01 s^{-1} at strain 0.4; (b) 1000°C, and the strain rate transient decreases from 0.01 s^{-1} to 0.001 s^{-1} at strain 0.4; (c) 1100°C, and the strain rate transient increases from 0.001 s^{-1} to 0.01 s^{-1} at strain 0.4; (d) 1100°C, and the strain rate transient decreases from 0.01 s^{-1} to 0.001 s^{-1} at strain 0.4.

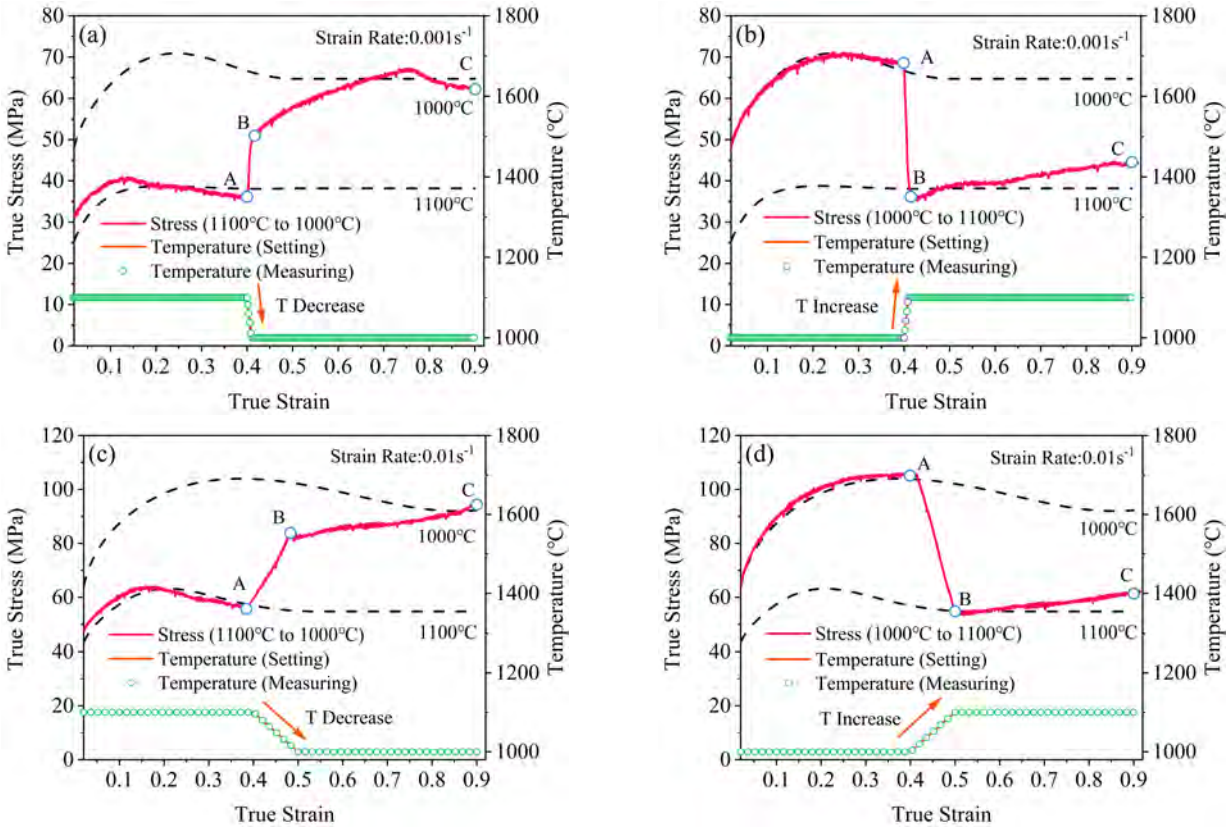

Fig. 4. Stress-strain curves under deformation temperature variation state. (a) $0.001s^{-1}$, and the deformation temperature decreases from 1100℃ to 1000℃ from strain 0.4 to 0.41; (b) $0.001s^{-1}$, and the deformation temperature increases from 1000℃ to 1100℃ from strain 0.4 to 0.41; (c) $0.01s^{-1}$, and the deformation temperature decreases from 1100℃ to 1000℃ from strain 0.4 to 0.5; (d) $0.01s^{-1}$, and the deformation temperature increases from 1000℃ to 1100℃ from strain 0.4 to 0.5.

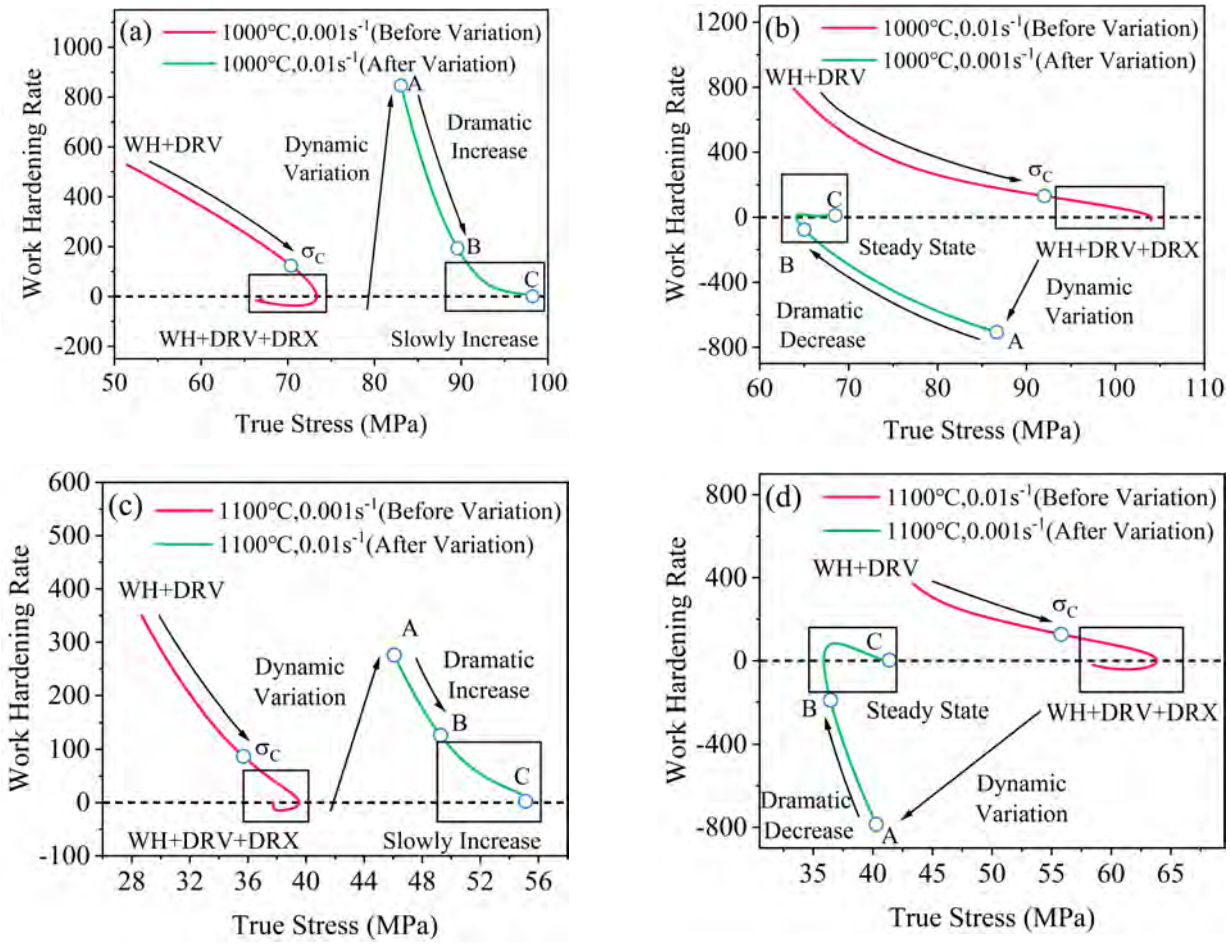

Fig. 5. Work-hardening curves under strain rate transient variation state. (a) 1000°C, and the strain rate transient increases from 0.001 s^{-1} to 0.01 s^{-1} at strain 0.4; (b) 1000°C, and the strain rate transient decreases from 0.01 s^{-1} to 0.001 s^{-1} at strain 0.4; (c) 1100°C, and the strain rate transient increases from 0.001 s^{-1} to 0.01 s^{-1} at strain 0.4; (d) 1100°C, and the strain rate transient decreases from 0.01 s^{-1} to 0.001 s^{-1} at strain 0.4.

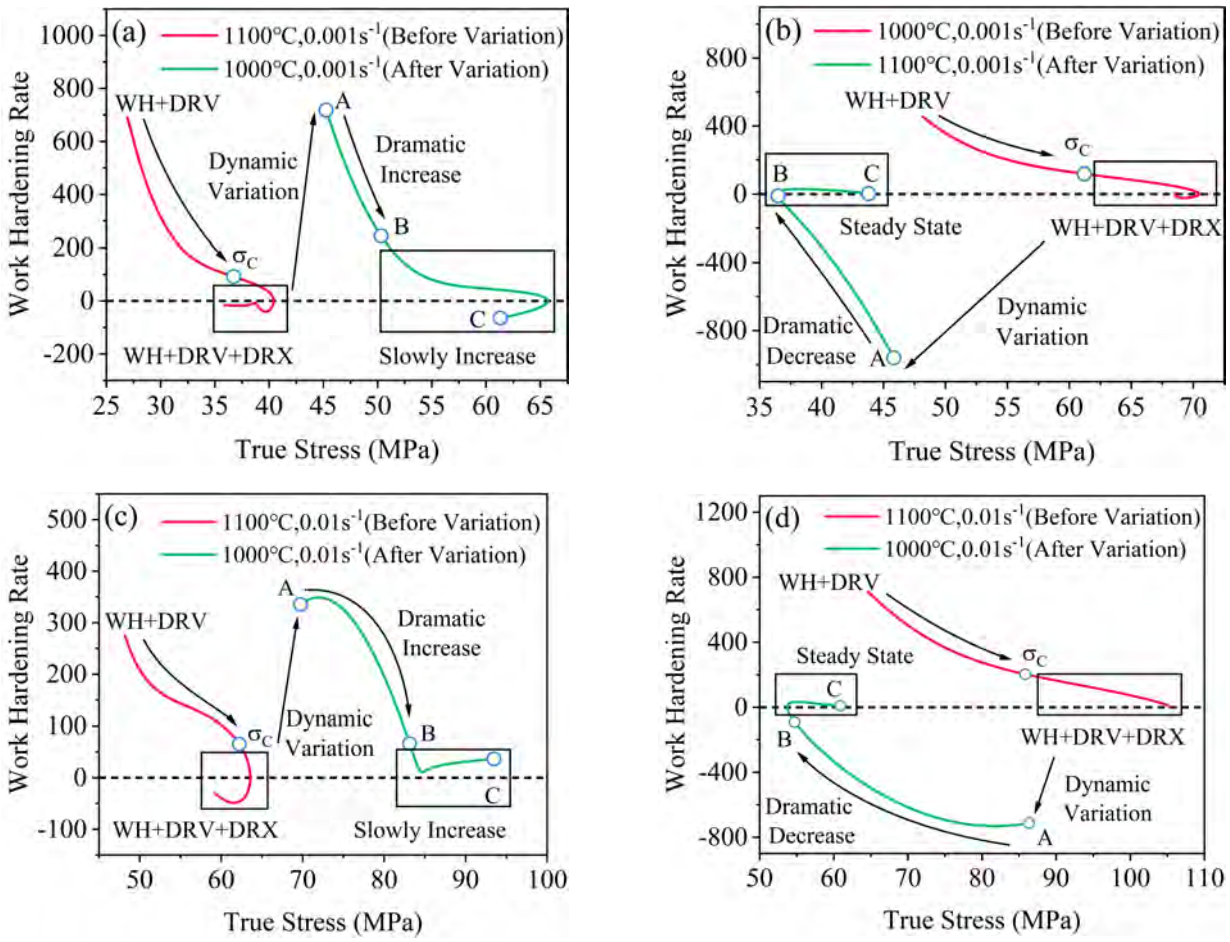

Fig. 6. Work-hardening curves under deformation temperature variation state. (a) $0.001s^{-1}$, and the deformation temperature decreases from 1100℃ to 1000℃ from strain 0.4 to 0.41; (b) $0.001s^{-1}$, and the deformation temperature increases from 1000℃ to 1100℃ from strain 0.4 to 0.41; (c) $0.01s^{-1}$, and the deformation temperature decreases from 1100℃ to 1000℃ from strain 0.4 to 0.5; (d) $0.01s^{-1}$, and the deformation temperature increases from 1000℃ to 1100℃ from strain 0.4 to 0.5.

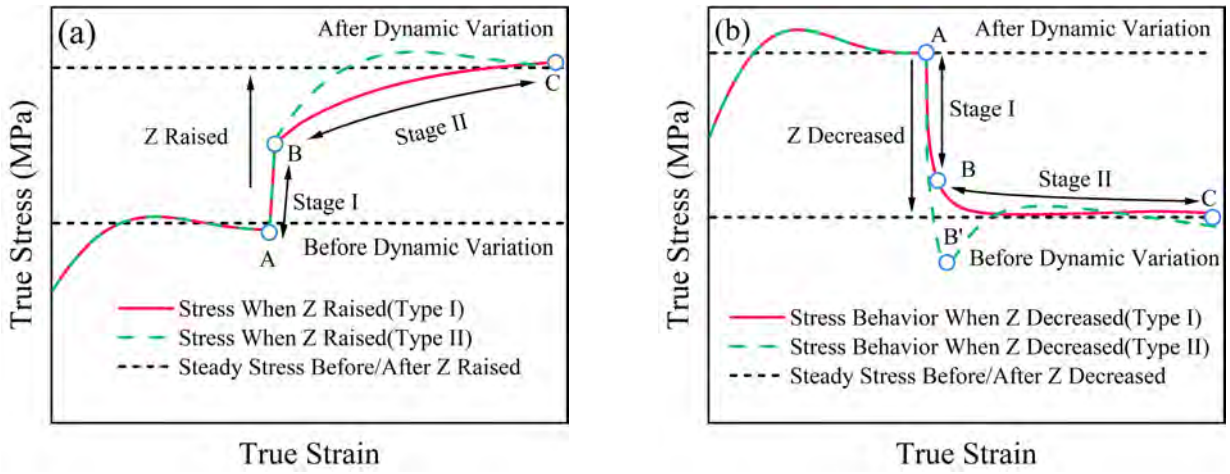

Fig. 7. The stress evolution after deformation conditions variation when entering the steady-state stage. (a) Z value transient increase; (b) Z value transient decrease.

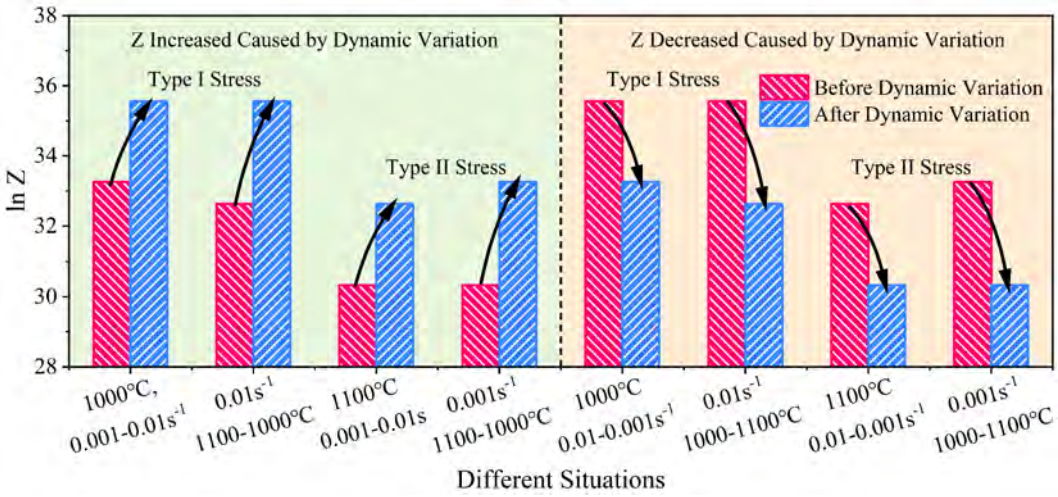

Fig. 8. The variation of the Z value under different deformation conditions in this paper.

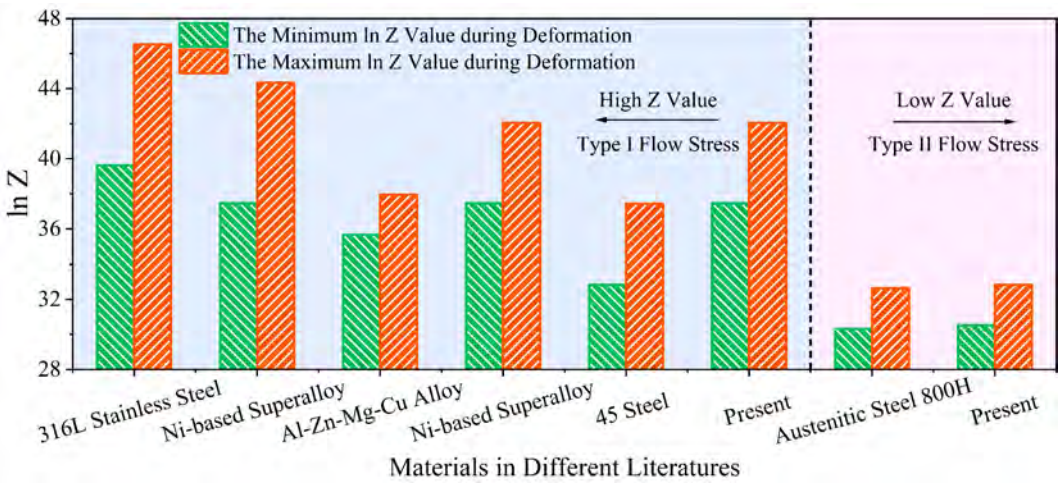

Fig. 9. The range of Z value variation for some materials in Table 3.

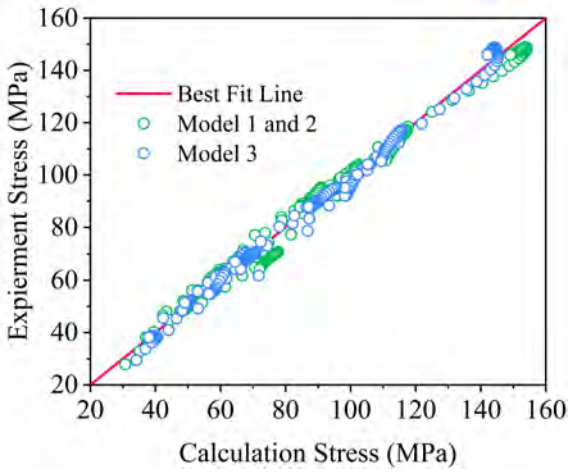

Fig. 10. The comparison between the accuracy of models 1 and 3 for steady deformation conditions.

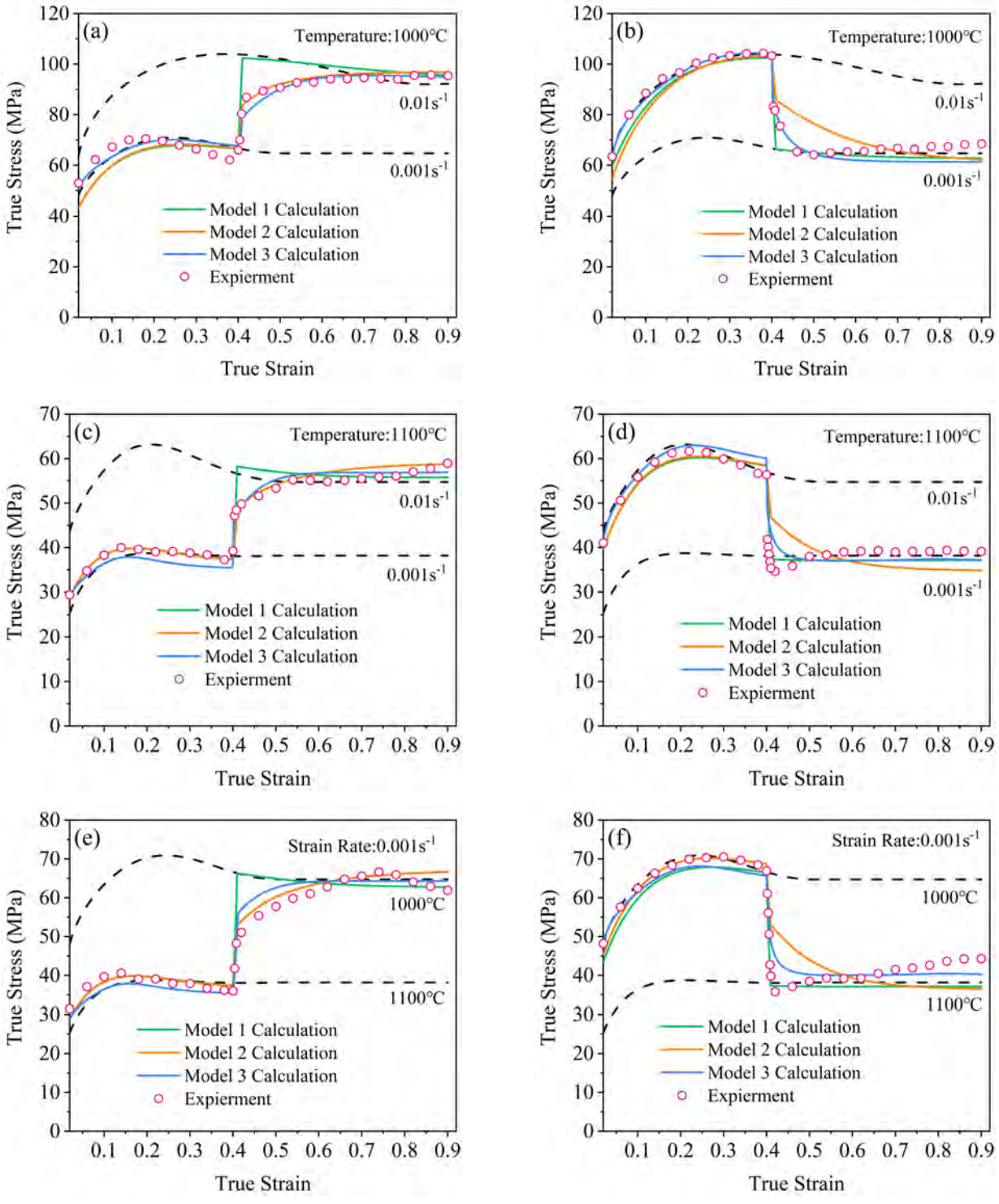
(a)
Temperature:1000°C
0.01s-1
0.001s-1
Model 1 Calculation
Model 2 Calculation
Model 3 Calculation
Expierment
True Stress (MPa)
True Strain
(b)
Temperature:1000°C
0.01s-1
0.001s-1
Model 1 Calculation
Model 2 Calculation
Model 3 Calculation
Expierment
True Stress (MPa)
True Strain
(c)
Temperature:1100°C
0.01s-1
0.001s-1
Model 1 Calculation
Model 2 Calculation
Model 3 Calculation
Expierment
True Stress (MPa)
True Strain
(d)
Temperature:1100°C
0.01s-1
0.001s-1
Model 1 Calculation
Model 2 Calculation
Model 3 Calculation
Expierment
True Stress (MPa)
True Strain
(e)
Strain Rate:0.001s-1
1000°C
1100°C
Model 1 Calculation
Model 2 Calculation
Model 3 Calculation
Expierment
True Stress (MPa)
True Strain
(f)
Strain Rate:0.001s-1
1000°C
1100°C
Model 1 Calculation
Model 2 Calculation
Model 3 Calculation
Expierment
True Stress (MPa)
True Strain

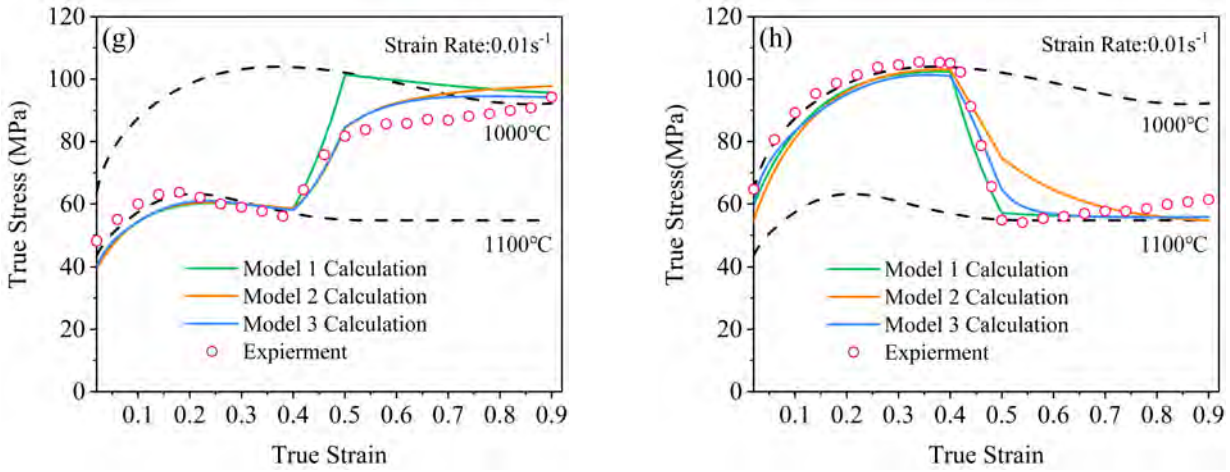

Fig. 11. The comparison between the accuracy of the three models for the dynamic variation states. (a) 1000°C, and the strain rate transient increases from 0.001 s^{-1} to 0.01 s^{-1} at strain 0.4; (b) 1000°C, and the strain rate transient decreases from 0.01 s^{-1} to 0.001 s^{-1} at strain 0.4; (c) 1100°C, and the strain rate transient increases from 0.001 s^{-1} to 0.01 s^{-1} at strain 0.4; (d) 1100°C, and the strain rate transient decreases from 0.01 s^{-1} to 0.001 s^{-1} at strain 0.4; (e) 0.001s^{-1}, and the deformation temperature decreases from 1100℃ to 1000℃ from strain 0.4 to 0.41; (f) 0.001s^{-1}, and the deformation temperature increases from 1000℃ to 1100℃ from strain 0.4 to 0.41; (g) 0.01s^{-1}, and the deformation temperature decreases from 1100℃ to 1000℃ from strain 0.4 to 0.5; (h) 0.01s^{-1}, and the deformation temperature increases from 1000℃ to 1100℃ from strain 0.4 to 0.5.

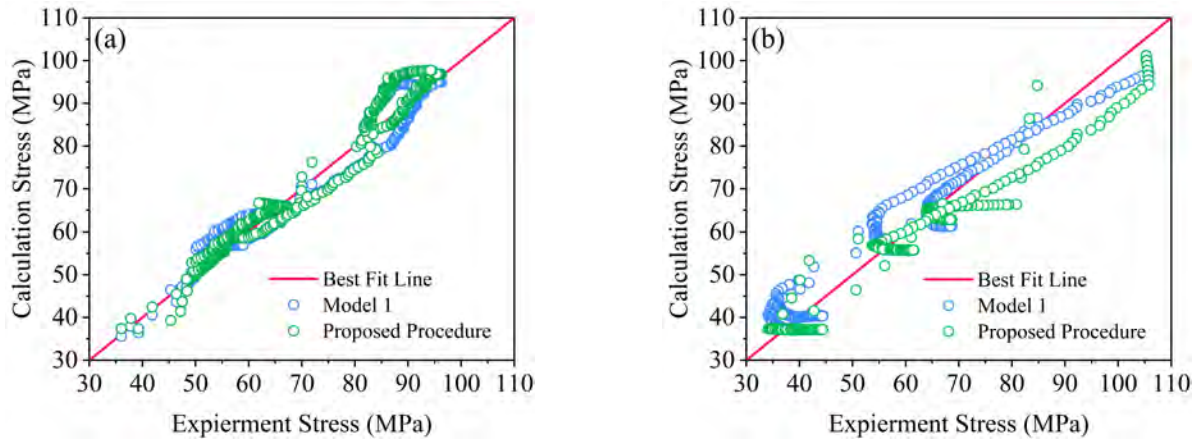

Fig. 12. The comparison between the accuracy of the three models for the dynamic variation states. (a) Z value increases cases; (b) Z value decreases cases.

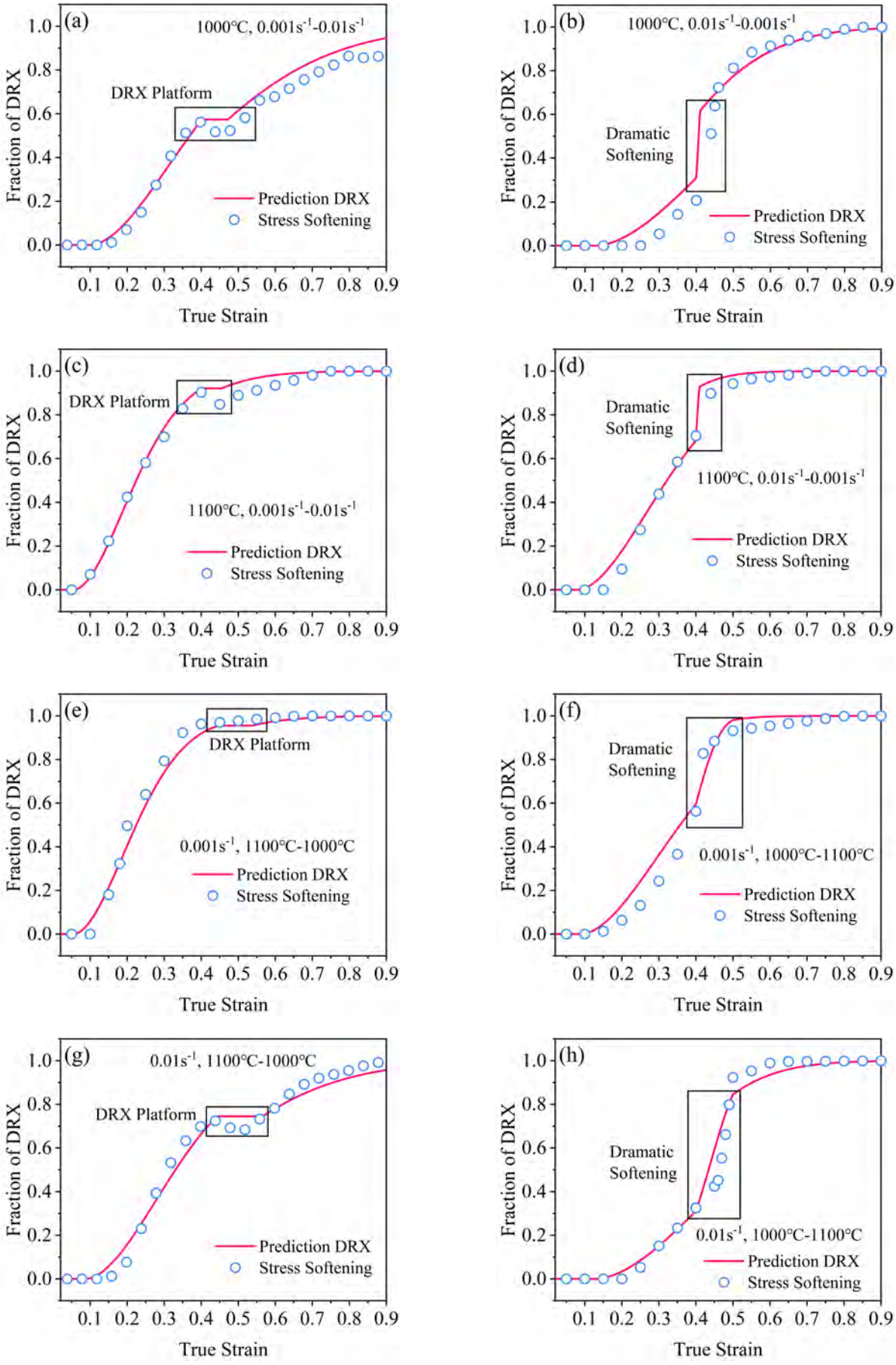
(a)
1000°C, 0.001s-1-0.01s-1
DRX Platform
Prediction DRX
Stress Softening
(b)
1000°C, 0.01s-1-0.001s-1
Dramatic Softening
(c)
1100°C, 0.001s-1-0.01s-1
(d)
1100°C, 0.01s-1-0.001s-1
(e)
0.001s-1, 1100°C-1000°C
(f)
0.001s-1, 1000°C-1100°C
(g)
0.01s-1, 1100°C-1000°C
(h)
0.01s-1, 1000°C-1100°C
Fraction of DRX
True Strain

Fig. 13. The comparison between the predicted DRX fraction with the stress softening degree for the dynamic variation states. (a) 1000°C, and the strain rate transient increases from 0.001 s^{-1} to 0.01 s^{-1} at strain 0.4; (b) 1000°C, and the strain rate transient decreases from 0.01 s^{-1} to 0.001 s^{-1} at strain 0.4; (c) 1100°C, and the strain rate transient increases from 0.001 s^{-1} to 0.01 s^{-1} at strain 0.4; (d) 1100°C, and the strain rate transient decreases from 0.01 s^{-1} to 0.001 s^{-1} at strain 0.4; (e) 0.001s^{-1}, and the deformation temperature decreases from 1100℃ to 1000℃ from strain 0.4 to 0.41; (f) 0.001s^{-1}, and the deformation temperature increases from 1000℃ to 1100℃ from strain 0.4 to 0.41; (g) 0.01s^{-1}, and the deformation temperature decreases from 1100℃ to 1000℃ from strain 0.4 to 0.5; (h) 0.01s^{-1}, and the deformation temperature increases from 1000℃ to 1100℃ from strain 0.4 to 0.5.

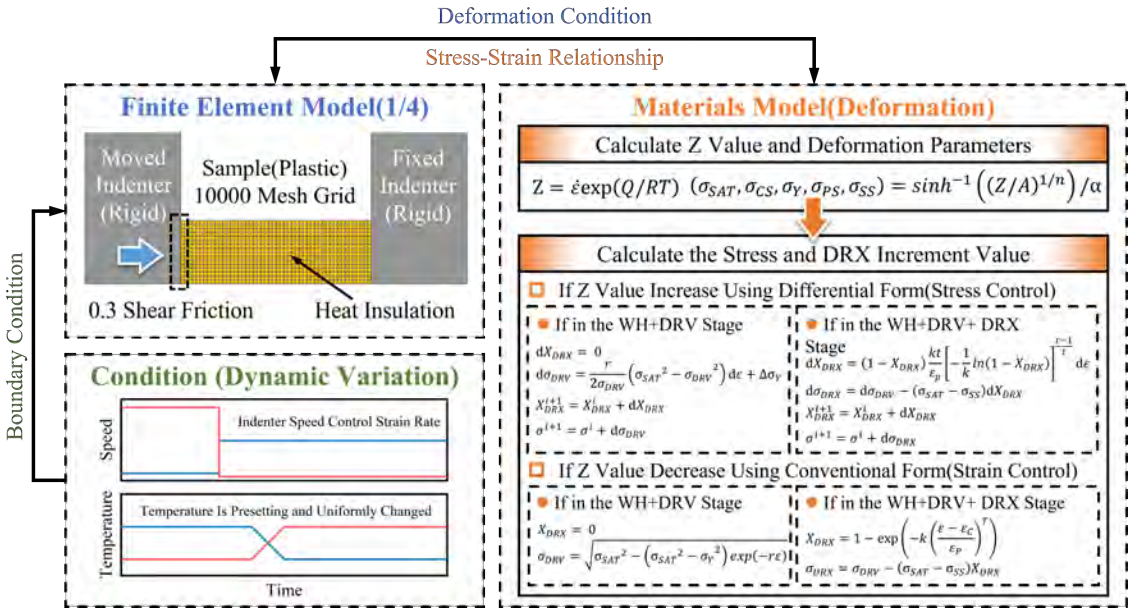

Fig. 14. The finite element model and boundary conditions.

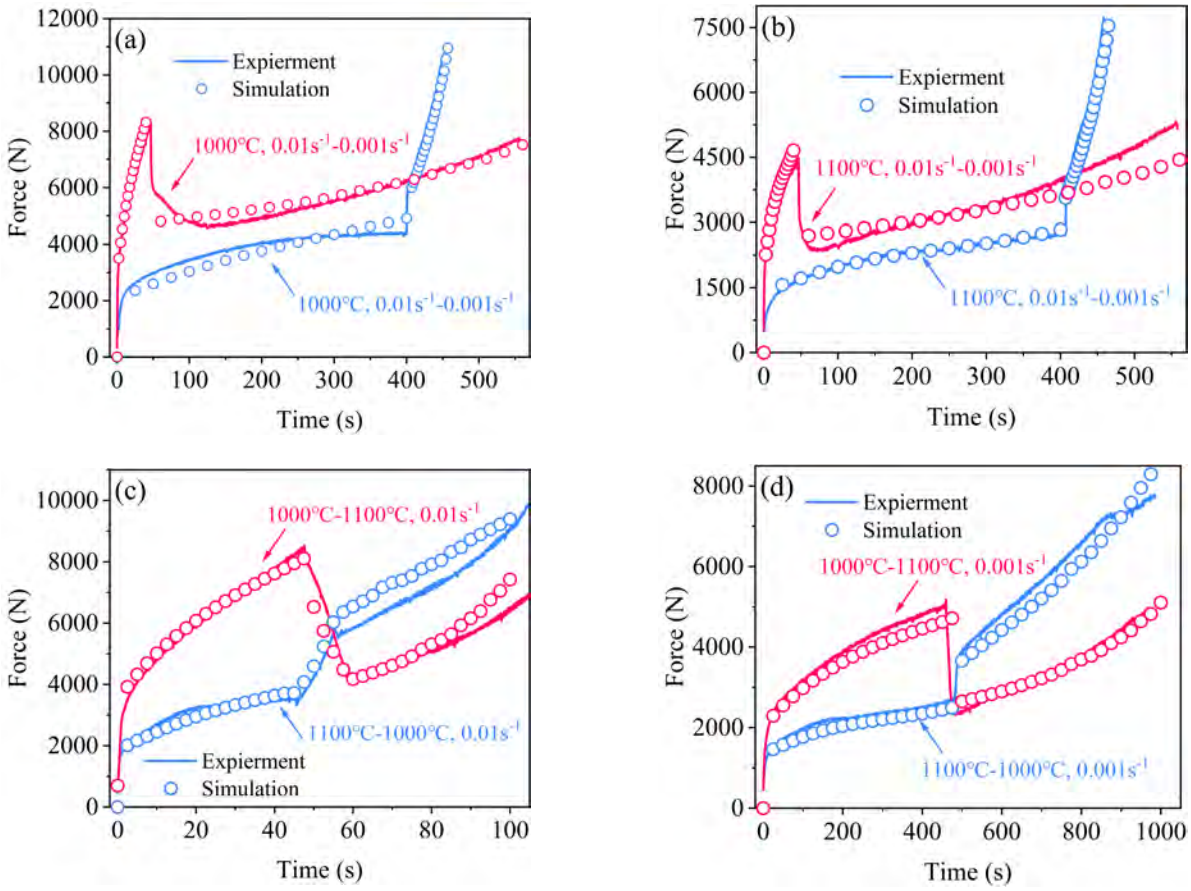

Fig. 15. The load-time comparison between the experiment and simulation under different dynamic variation states. a) strain rate dynamic increases or decreases at 1000°C; b) strain rate dynamic increases or decreases at 1100°C; c) temperature dynamic increase or decrease at $0.01s^{-1}$; d) temperature dynamic increase or decrease at $0.001s^{-1}$.

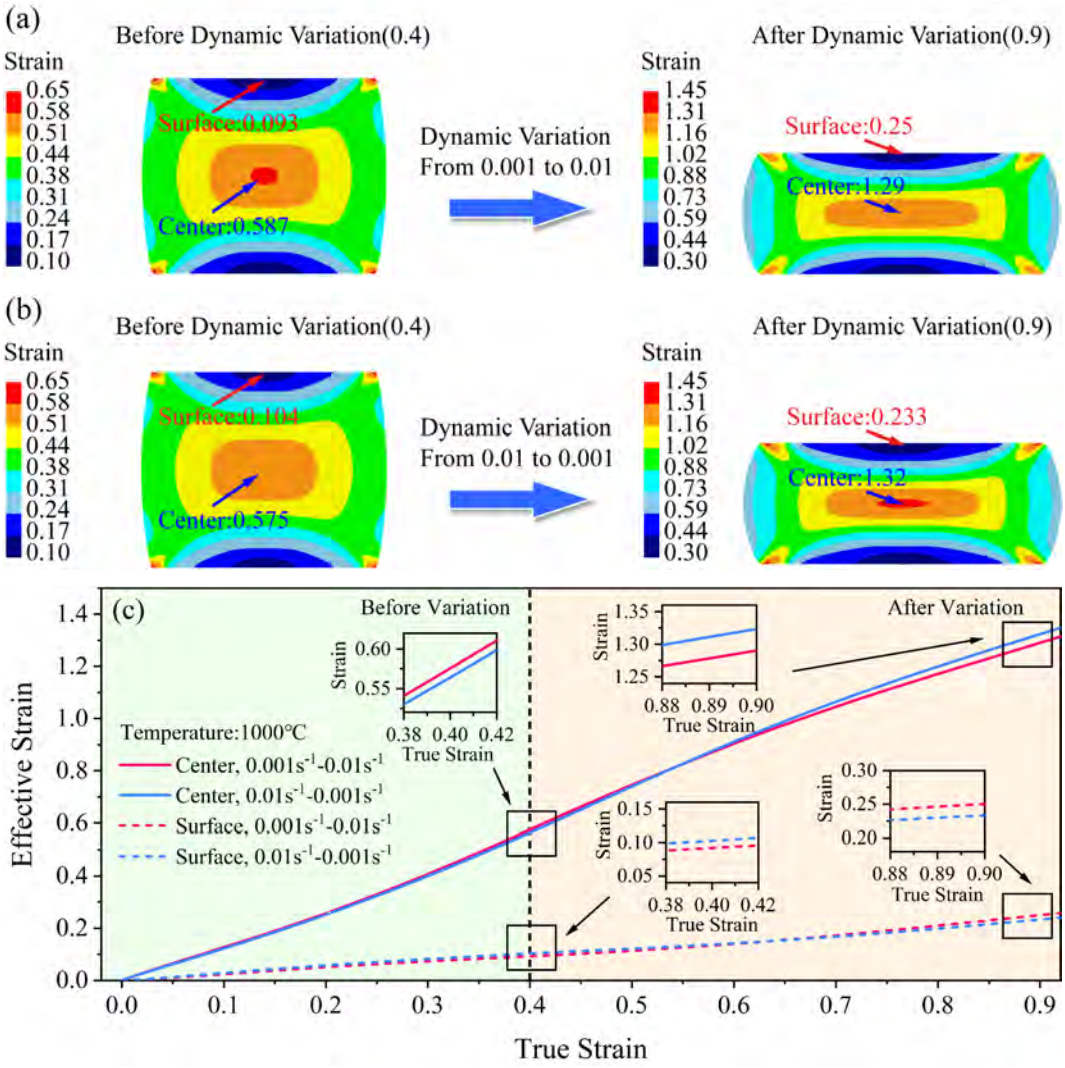

Fig. 16. The effective strain distribution at the beginning of the deformation conditions variation (true strain 0.4) and the end of the deformation (true strain 0.9) under dynamic variation states a) 1000°C, with transient changes of $0.001s^{-1}$-$0.01s^{-1}$ at 0.4 true strain; b) 1000°C, with transient changes of $0.01s^{-1}$-$0.001s^{-1}$ at 0.4 true strain.; c) the effective strain evolutions of the center and surface position in the above two cases.

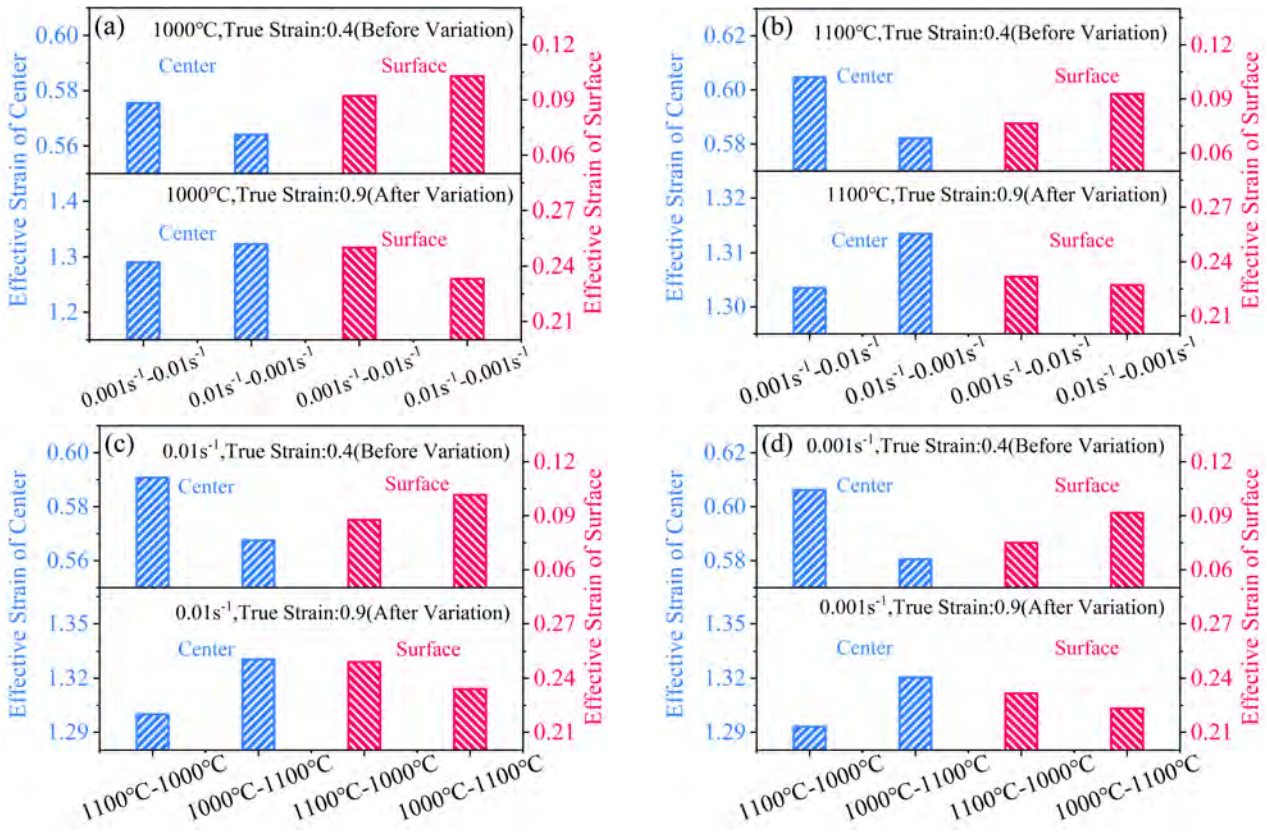

Fig. 17. The center and surface effective strain at the beginning of the deformation conditions variation (true strain 0.4) and the end of the deformation (true strain 0.9). (a)1000℃, $0.001s^{-1}$-$0.01s^{-1}$ and $0.01s^{-1}$-$0.001s^{-1}$; (b) 1100℃, $0.001s^{-1}$-$0.01s^{-1}$ and $0.01s^{-1}$-$0.001s^{-1}$; (c) $0.01s^{-1}$,1000℃-1100℃ and 1100℃-1000℃; (d) $0.001s^{-1}$,1000℃-1100℃ and 1100℃-1000℃.

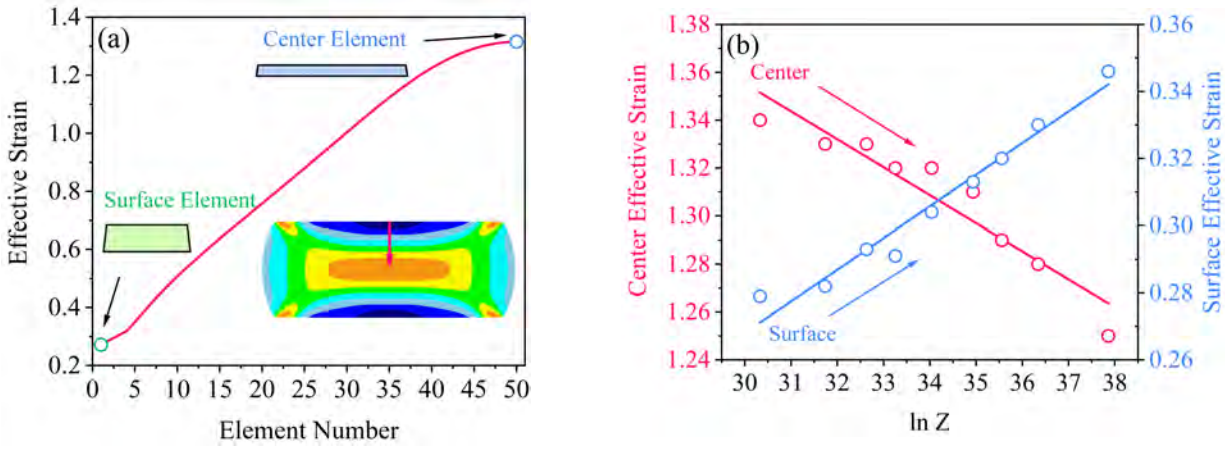

Fig. 18. Non-uniform strain distribution during deformation. (a) the effective strain distribution from surface to center under the deformation condition in Fig. 17. (a); (b) the surface and center effective strain versus Z value for deformation to a true strain of 0.9 at different constant deformation temperatures (1000°C, 1050°C, 1100°C) and strain rates ($0.1s^{-1}$, $0.01s^{-1}$, $0.001s^{-1}$).

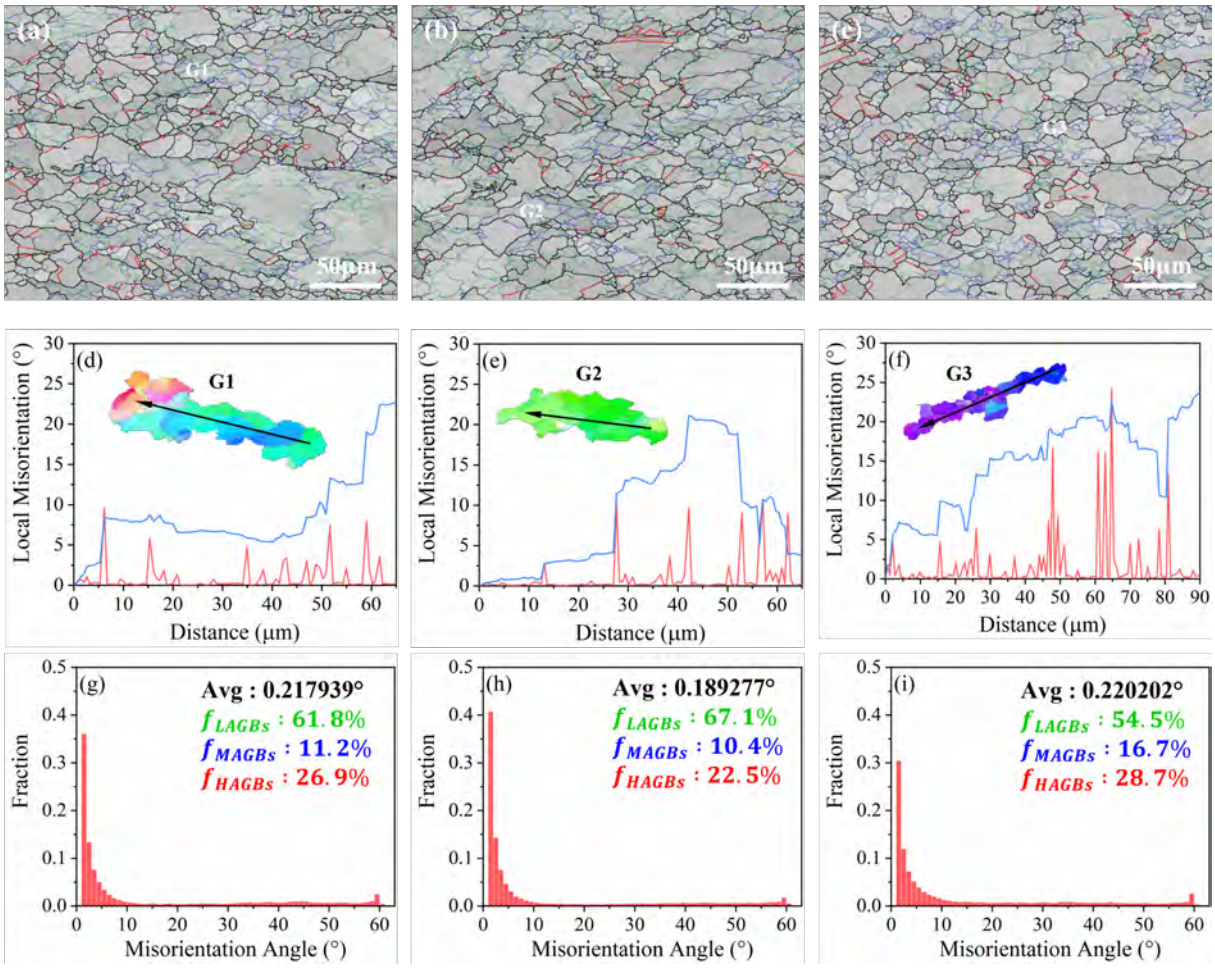

Fig. 19. Microstructure evolution under a deformation condition that strain rate transient increases from $0.001s^{-1}$ to $0.01s^{-1}$ with 1000℃ at different true strain (0.4, 0.6, 0.9). (a)-(c) Grain boundary map; (d)-(f) The local and cumulative misorientation statistics; (g)-(i) Grain boundary statistics.

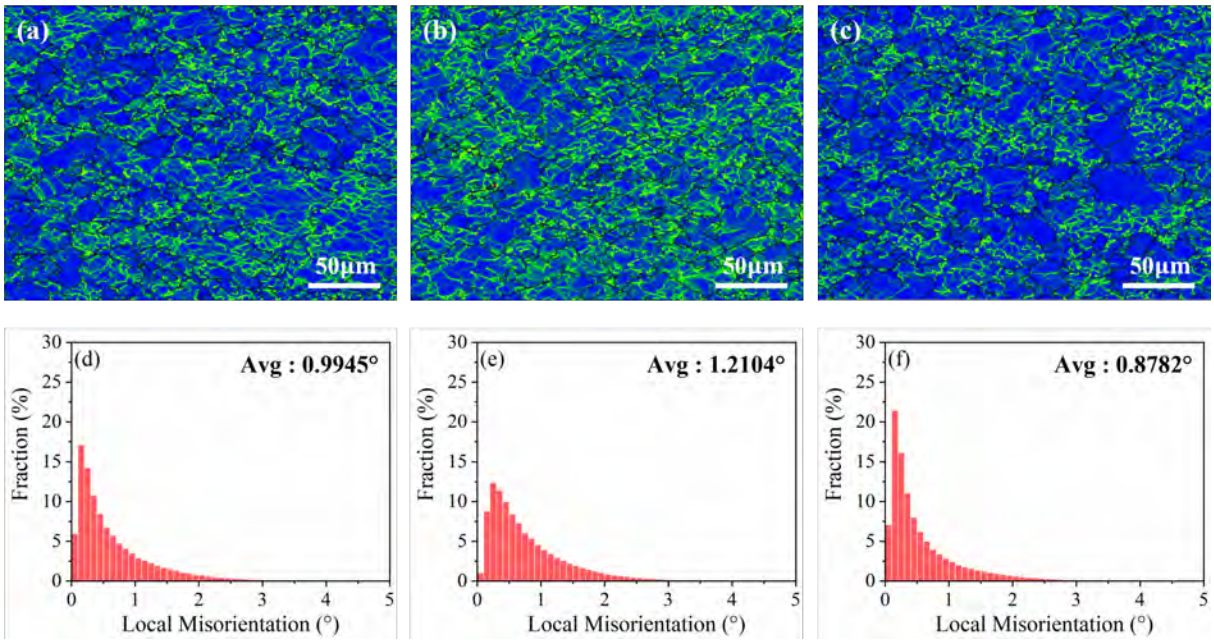

Fig. 20. Deformation energy statistics under a deformation condition that strain rate transient increases from $0.001s^{-1}$ to $0.01s^{-1}$ with 1000℃ at different true strain (0.4, 0.6, 0.9). (a)-(c) Local misorientation angle map; (d)-(f) The local misorientation statistics.

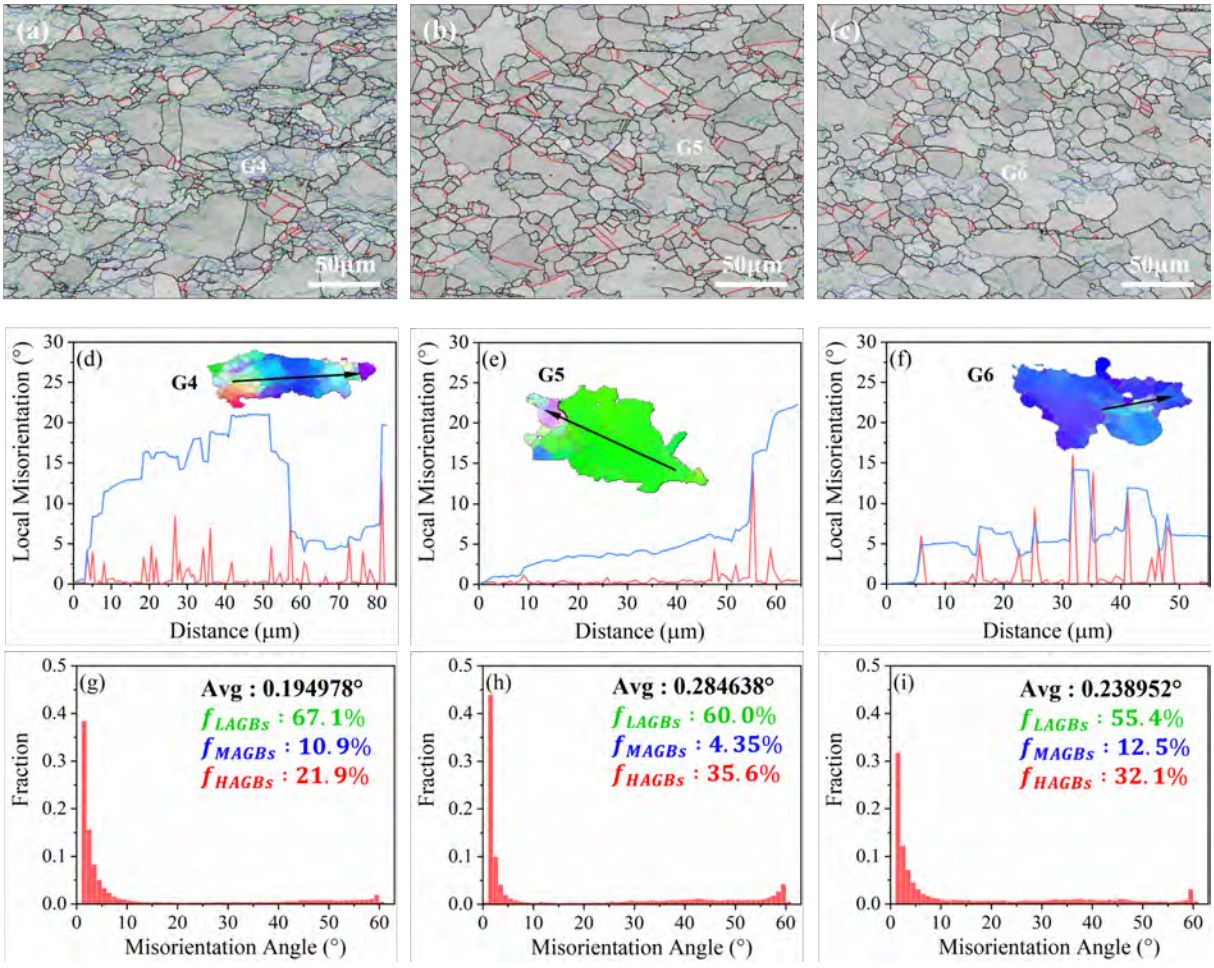

Fig. 21. Microstructure evolution under a deformation condition that strain rate transient decreases from $0.01s^{-1}$ to $0.001s^{-1}$ with 1000℃ at different true strain (0.4, 0.6, 0.9). (a)-(c) Grain boundary map; (d)-(f) The local and

cumulative misorientation statistics; (g)-(i) Grain boundary statistics.

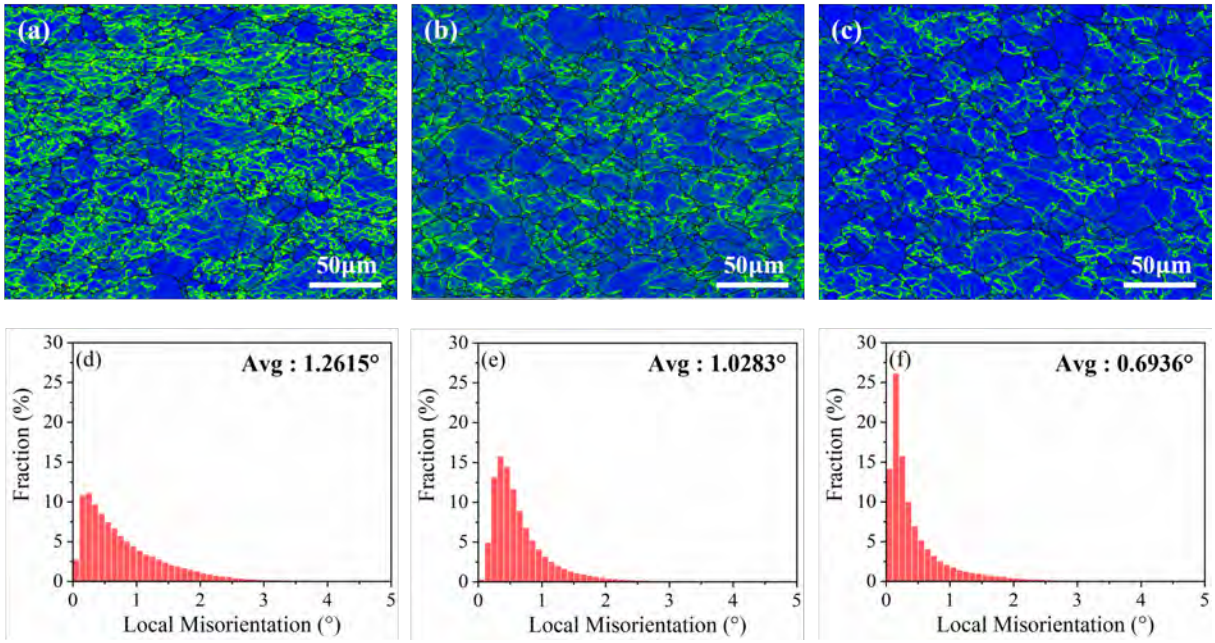

Fig. 22. Deformation energy statistics under a deformation condition that strain rate transient decreases from 0.01s^{-1} to 0.001s^{-1} with 1000℃ at different true strain (0.4, 0.6, 0.9). (a)-(c) Local misorientation angle map; (d)-(f) The local misorientation statistics.

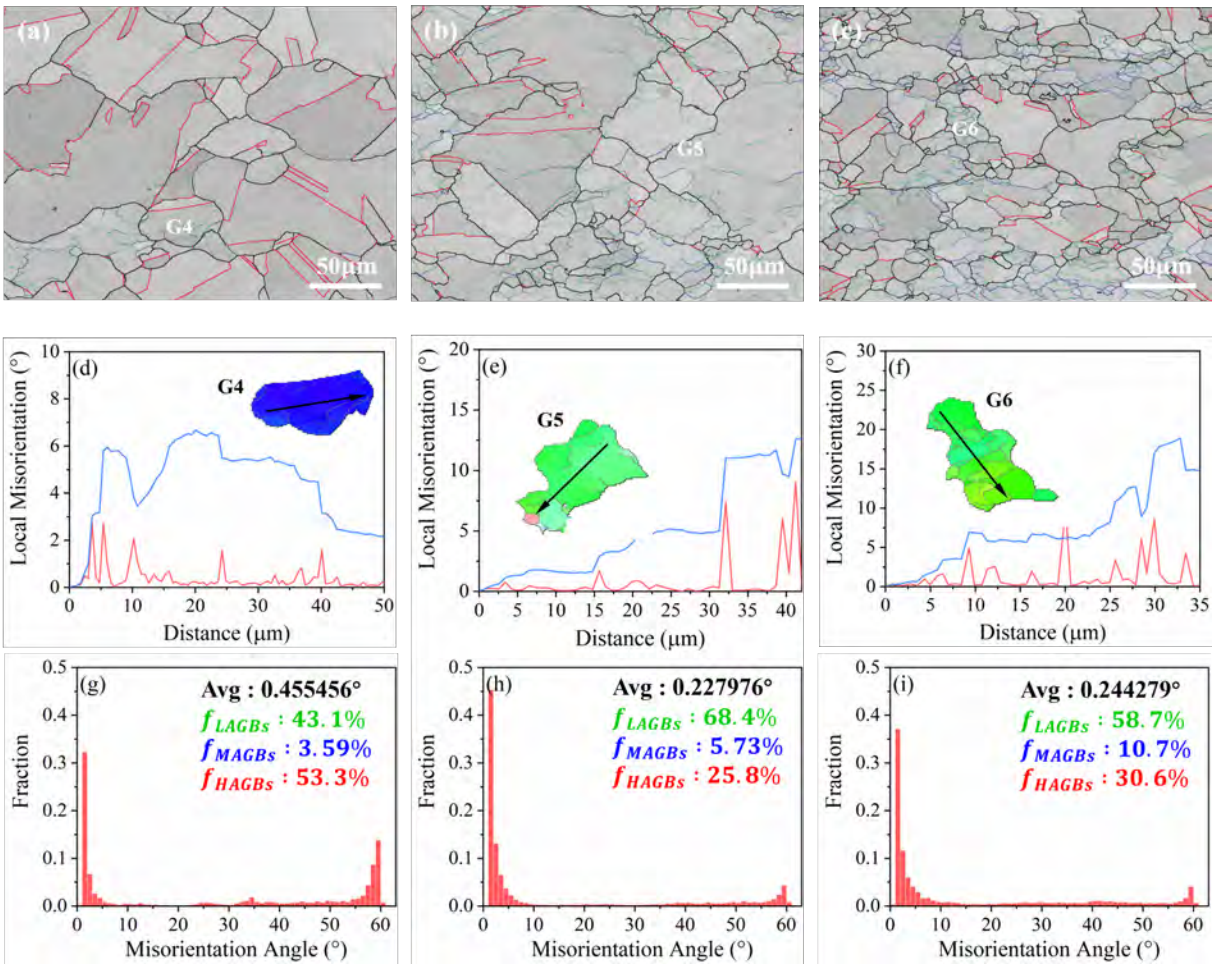

Fig. 23. Microstructure evolution under a deformation condition that temperature decreases from 1100℃ to 1000℃

with 0.001s^{-1} at different true strain (0.4, 0.6, 0.9). (a)-(c) Grain boundary map; (d)-(f) The local and cumulative misorientation statistics; (g)-(i) Grain boundary statistics.

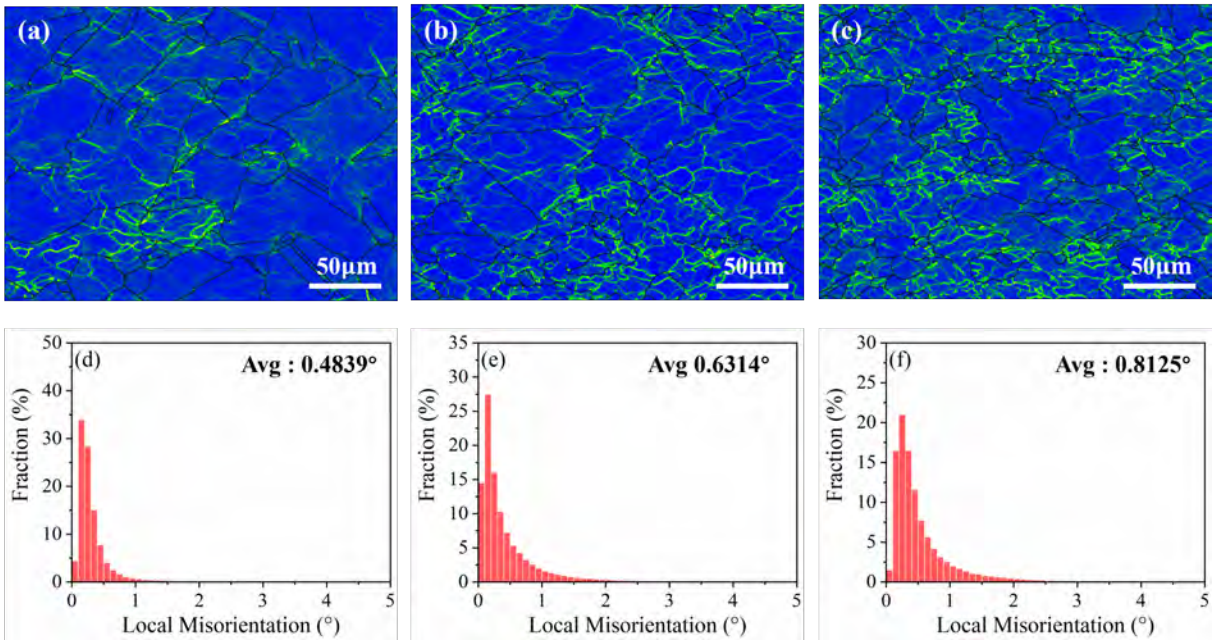

Fig. 24. Deformation energy statistics under a deformation condition that temperature decreases from 1100℃ to 1000℃ with 0.001s^{-1} at different true strain (0.4, 0.6, 0.9). (a)-(c) Local misorientation angle map; (d)-(f) The local misorientation statistics.

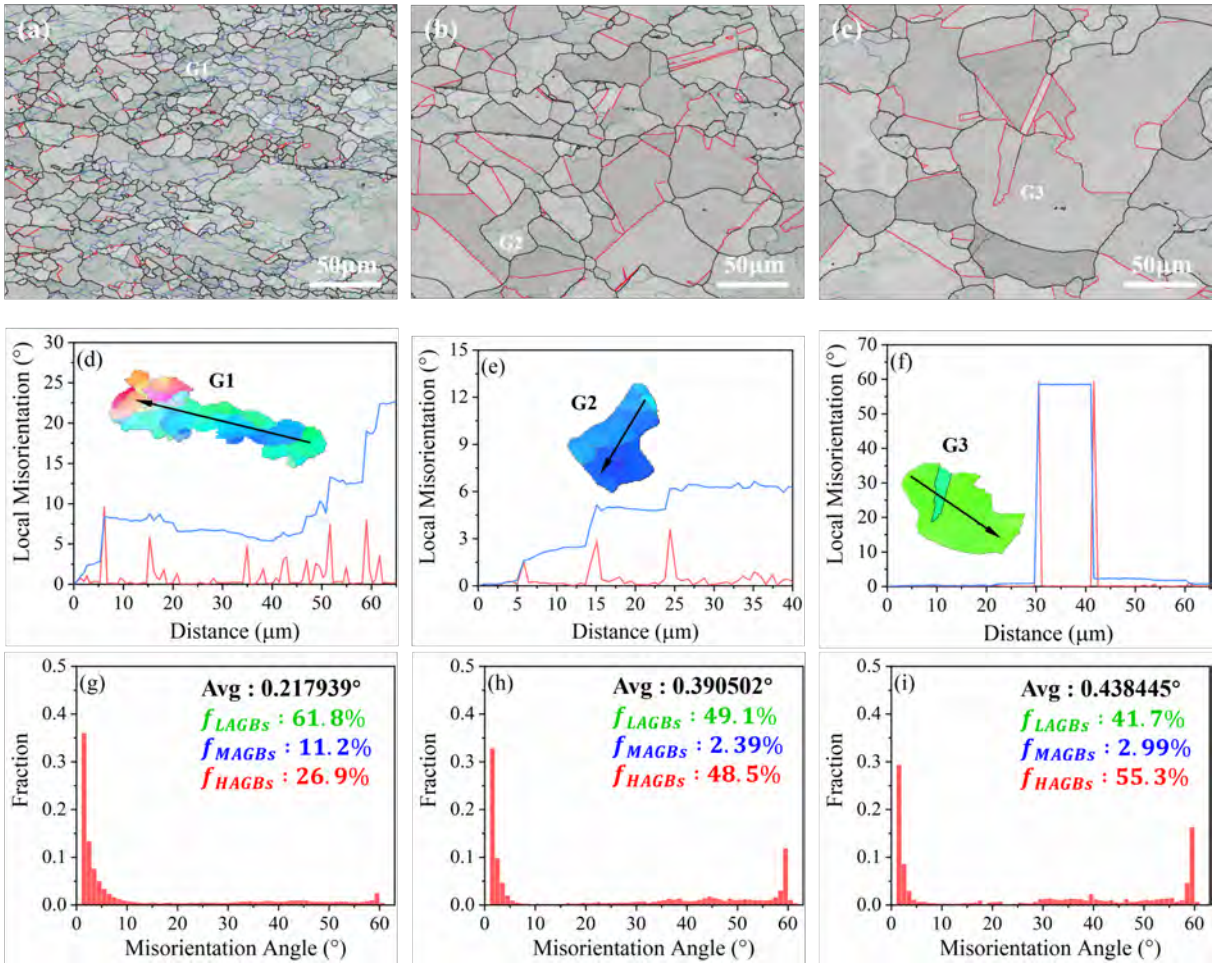

Fig. 25. Microstructure evolution under a deformation condition that temperature increases from 1000℃ to 1100℃ with 0.001s^{-1} at different true strain (0.4, 0.6, 0.9). (a)-(c) Grain boundary map; (d)-(f) The local and cumulative misorientation statistics; (g)-(i) Grain boundary statistics.

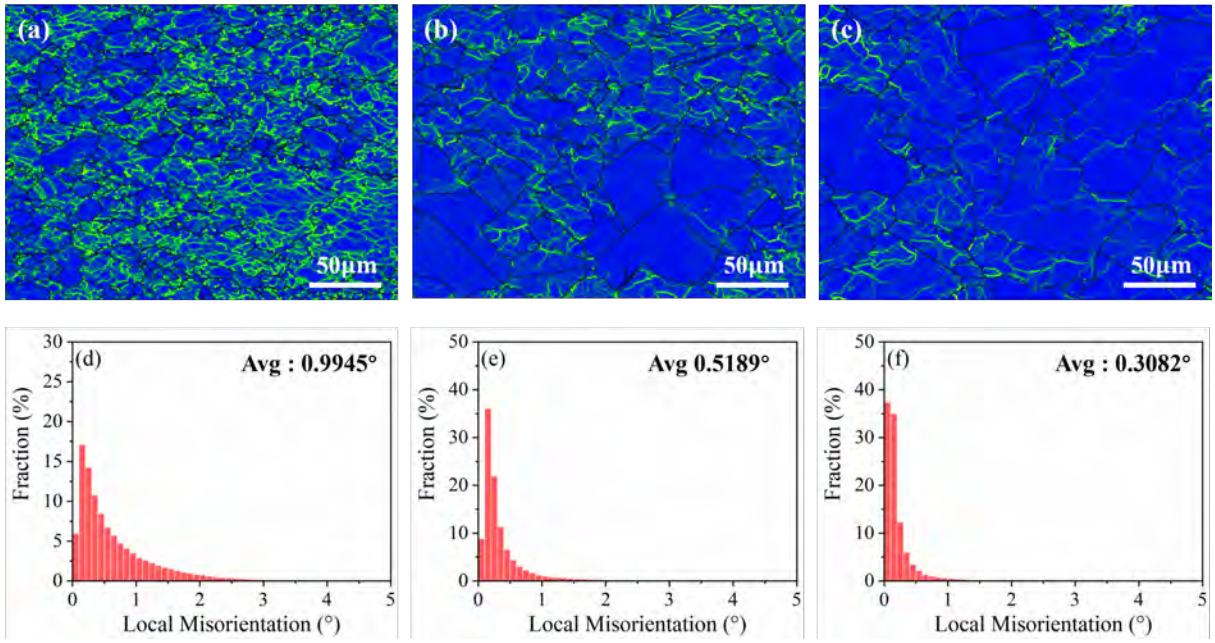

Fig. 26. Deformation energy statistics under a deformation condition that temperature increases from 1000℃ to 1100℃ with 0.001s^{-1} at different true strain (0.4, 0.6, 0.9). (a)-(c) Local misorientation angle map; (d)-(f) The local misorientation statistics.

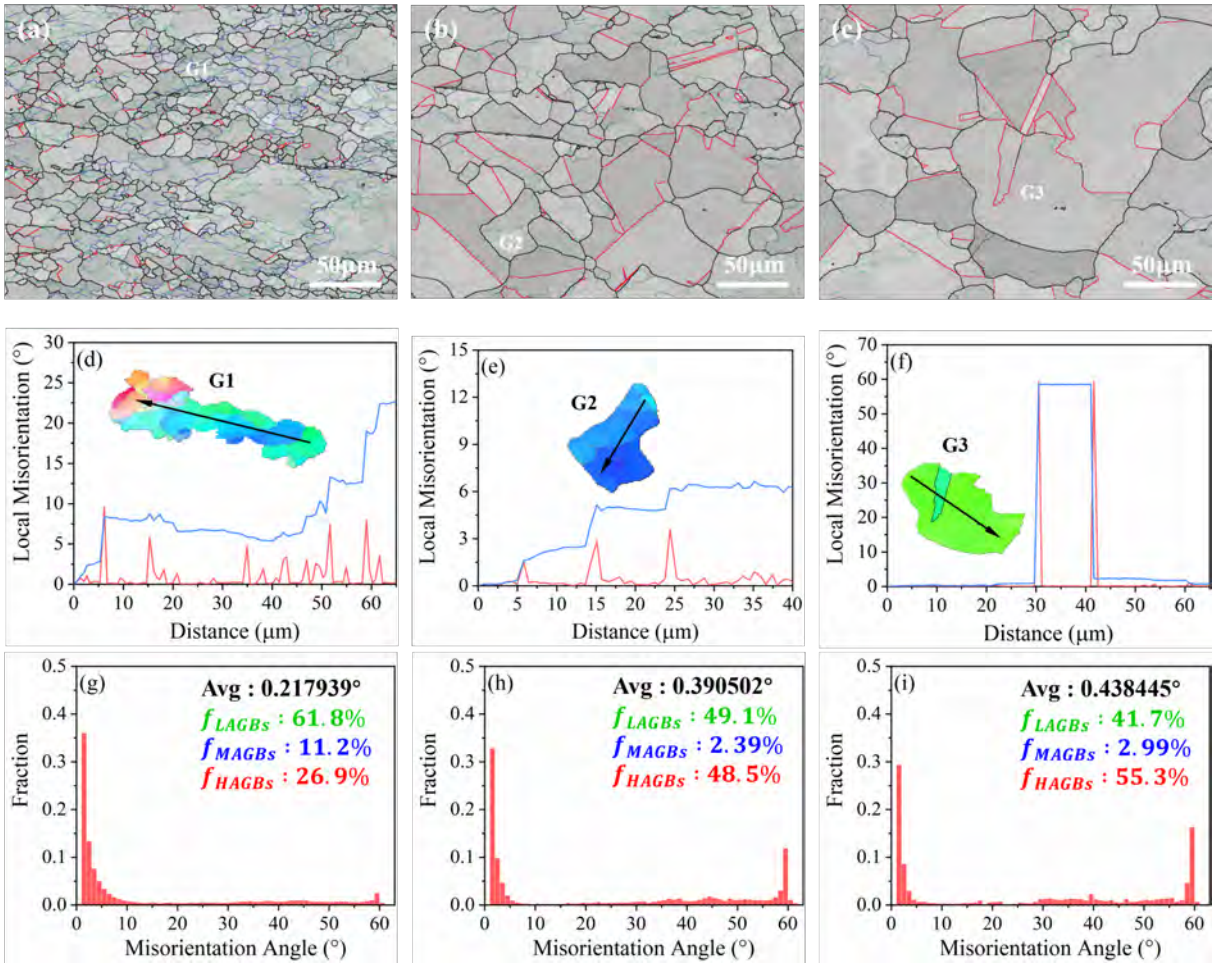

Fig. 25. Microstructure evolution under a deformation condition that temperature increases from 1000℃ to 1100℃ with 0.001s^{-1} at different true strain (0.4, 0.6, 0.9). (a)-(c) Grain boundary map; (d)-(f) The local and cumulative misorientation statistics; (g)-(i) Grain boundary statistics.

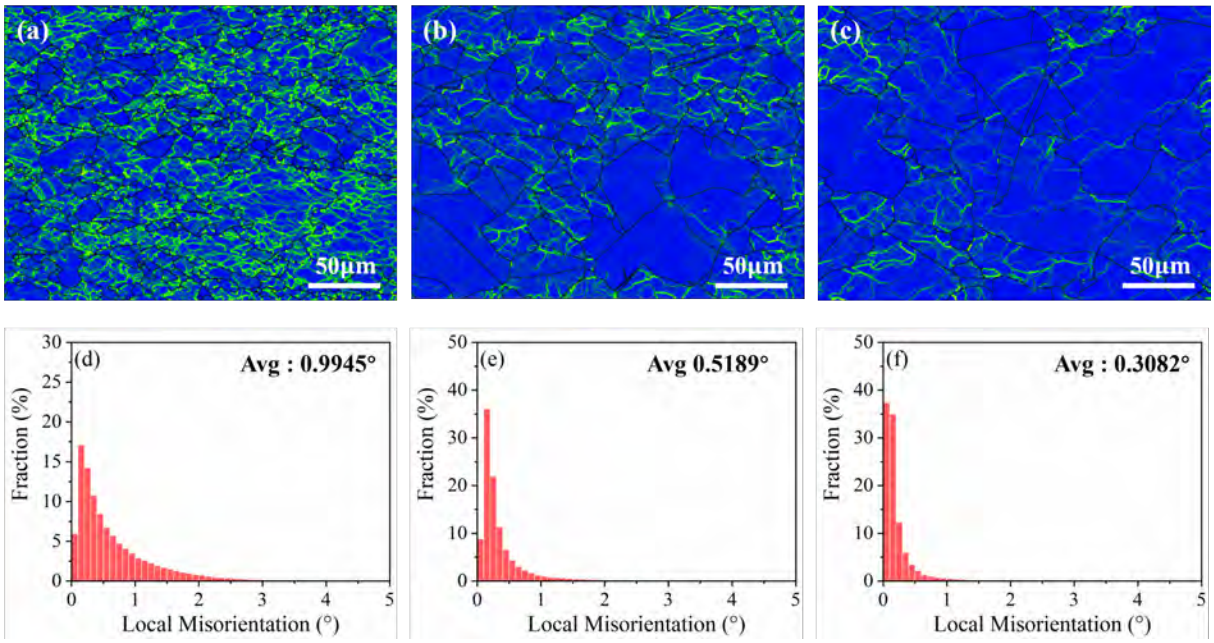

Fig. 26. Deformation energy statistics under a deformation condition that temperature increases from 1000℃ to 1100℃ with 0.001s^{-1} at different true strain (0.4, 0.6, 0.9). (a)-(c) Local misorientation angle map; (d)-(f) The local misorientation statistics.